Torque Magnetometry in Novel Superconductors
I Torque Apparatus Developments
II Correlation Lengths and Anisotropy

Dissertation

zur
Erlangung der naturwissenschaftlichen Doktorwürde
(Dr. sc. nat.)

vorgelegt der
Mathematisch-naturwissenschaftlichen Fakultät der
Universität Zürich

von

Stefan Kohout

von Villigen AG

Promotionskomitee

Prof. Dr. Hugo Keller (Vorsitz)
Prof. Dr. Toni Schneider
Prof. Dr. Andreas Schilling

Zürich, 2005

für Vera

Summary

Since the discovery of high-T_c superconductivity in $La_{2-x}Ba_xCuO_4$ by J.G. Bednorz and K.A. Müller in 1986 a considerable number of studies have been performed on this and the related so-called cuprate family of compounds. Even though a theory exists, which explains well the conventional, so-called low-T_c superconductivity, it was soon shown that it fails in the description of these newly discovered compounds. Today, a concise explanation of superconductivity at temperatures up to 100 K is still missing. Being considered a macroscopic manifestation of quantum effects, it is one of the most important and difficult problems in modern solid state physics and materials research. The need for more precise and reliable measurements has pushed forward various experimental methods which have reached impressive sensitivities. Torque magnetometry is one of these measurement techniques. The early application of atomic-force microscope tips for torque measurements laid the basis for further improvements. Such custom built piezoresistive torque sensors are now the most sensitive instruments worldwide available, capable of measuring tiny micro crystals of superconducting material, far below the detection limit of commercial magnetometers. The implementation of torque sensors with a novel design is presented in this thesis. This allows new measurement configurations to be considered. Sensors for simultaneous measurements along two orthogonal directions are realizable. Another version includes a diode on the sample platform. This can be used for accurate thermometry of the sample itself, rather than of a point close to it.

However, sheer sensitivity and sophisticated techniques are not enough for significant statements about physical properties. The materials exhibiting high-T_c superconductivity are extremely complex, consisting of dozens of atoms in the crystallographic unit cell. The dependence of physical properties on the exact composition and structure are equally complex, often causing uncertainty about whether certain features benefit or impede superconductivity. Therefore, comparisons across different kinds of samples and compounds as well as searches for systematics within a vast parameter space become increasingly more important than observations of minute effects in

special measurement conditions. This demands efficient methods for measurement taking and data acquisition, storage and evaluation. A large part of this thesis was therefore devoted to the development of an automated measurement system. Such automation is possible with most commercially available apparatuses, but the workload associated with the creation of the sophisticated software systems needed, is often beyond the capabilities of a research group. However, in this work, an approach is presented for the creation of LabVIEW programs which can be easily used to achieve automation of arbitrarily customized equipment.

It was this inclusion of automation into the torque apparatus which allowed the studies presented in the second part of this thesis. In one instance, the angle, field and temperature dependence of transitions of the vortex structure were investigated in variously doped samples of the $La_{2-x}Sr_xCuO_4$ compound. These effects are observed in layered superconductors in the mixed state, where the magnetic flux penetrates the sample in form of quantized vortices. Generally, these vortices are oriented between the external applied field and the direction perpendicular to the CuO_2-planes of the sample. However, when the external magnetic field is applied sufficiently close to the CuO_2-planes, the vortices prefer aligning with these planes, causing characteristic changes of torque. The extended data obtained with the automated torque apparatus allowed the determination of the angle and field dependence of these changes and their influence on the determination of important material properties.

Zusammenfassung

Seit der Entdeckung der Hochtemperatursupraleitung in $La_{2-x}Ba_xCuO_4$ durch J.G. Bednorz und K.A. Müller im Jahre 1986 wurde eine beträchtliche Anzahl von Untersuchungen auf diesem Material und den verwandten so genannten Kupraten durchgeführt. Obwohl eine Theorie bekannt ist, die die Tieftemperatursupraleitung sehr gut erklärt, war früh klar, dass diese Beschreibung auf diese neuartigen Materialien nicht anwendbar ist. Nach wie vor ist keine Erklärung für Supraleitung bei Temperaturen über 100 K bekannt. Dieses Problem wird als eine der wichtigsten und schwierigsten Fragen betrachtet, der die moderne Festkörperphysik und Materialwissenschaft gegenübersteht, unter anderem weil es sich dabei im makroskopische Ausprägungen von Quanteneffekten handelt. Der Bedarf nach präzisen und verlässlichen Messungen führte dazu, dass verschiedene Messmethoden stark weiterentwickelt wurden, wobei eindrückliche Empfindlichkeiten erzielt wurden. Drehmomentmagnetometrie ist eine dieser Messmethoden. Der Einsatz von Rasterkraftmikroskopiespitzen für Drehmomentmessungen legte den Grundstein für weitere Verbesserungen. Solche speziell für Drehmomentmessungen entwickelten piezoresistiven Sensoren sind heute weltweit die empfindlichsten Instrumente zur Bestimmung von magnetischen Eigenschaften. Mit ihrer Hilfe können winzige supraleitender Kristalle untersucht werden, welche mit kommerziell erhältlichen Apparaturen nicht mehr messbar sind. In dieser Arbeit wird die Herstellung von Drehmomentsensoren mit einem neuartigen Design beschrieben, welche neue Arten von Messungen ermöglichen. Beispielsweise können Sensoren hergestellt werden, welche die gleichzeitige Drehmomentmessung entlang zweier orthogonaler Achsen erlauben. Bei einer anderen Version wurde eine Diode auf der Probenplattform gefertigt, um eine direkte Messung der Temperatur der Probe zu erlauben.

Allerdings reichen je länger je mehr blosse Empfindlichkeit oder komplizierte Messaufbauten nicht mehr aus, um die nötigen Erkenntnisse über physikalische Grössen zu erhalten. Die Materialien, welche bei solch hohen Temperaturen supraleitend sind, sind ausserordentlich komplex. Sie enthalten Dutzende von Atomen in der Einheitszelle. Die Abhängigkeit der

physikalischer Messgrössen von der exakten Zusammensetzung und Struktur ist daher ähnlich komplex. Oft ist nicht klar, ob ein beobachteter Effekt für die Supraleitung förderlich ist, ob er sie behindert oder ob er weitgehend irrelevant ist. Deshalb werden Studien immer wichtiger, in denen eine grosse Anzahl von Proben systematisch über grosse Bereiche des Phasenraums (Temperatur, Magnetfeld, Druck, ...) untersucht werden. Dies verlangt aber effiziente Methoden bei der Messung und im Umgang mit den gemessenen Daten. Ein grosser Teil dieser Arbeit wurde deshalb darauf verwendet, die Messapparatur zu automatisieren. Eine solche Automatisierung ist zwar in den meisten kommerziell erhältlichen Messsystemen vorhanden, allerdings werden diese mit einem Aufwand entwickelt, der die Möglichkeiten einer Forschungsgruppe schnell übersteigt. In dieser Arbeit wird ein genereller Ansatz vorgestellt, der es erlaubt, beliebig komplexe Eigenbau-Messsysteme zu automatisieren. Es wird gezeigt, dass dies mit der einfach erlernbaren Programmierumgebung LabVIEW sogar mit vergleichbar geringem Aufwand erzielt werden kann.

Diese Automatisierung erlaubte die Durchführung der Studie, die im zweiten Teil der Arbeit besprochen wird. Dabei wurden systematisch die Winkel-, Feld- und Temperaturabhängigkeiten der Veränderungen der Struktur des Flussschlauchgitters in verschieden dotierten Proben von $La_{2-x}Sr_xCuO_4$ untersucht. Diese Effekte werden allgemein in diesen geschichteten Supraleitern im gemischten Zustand beobachtet, wo der magnetische Fluss die Probe in Form von quantisierten Flussschläuchen durchdringt. Im allgemeinen liegen diese annähernd parallel zum angelegten Feld. Wird das Feld allerdings nahezu parallel zu den CuO_2-Ebenen orientiert, kommen die Flussschläuche zwischen diesen Ebenen zu liegen und erzeugen charakteristische Signaturen in Magnetisierungs- und Drehmomentmessungen. Die systematische Untersuchung erlaubte die Bestimmung der Winkel- und Feldabhängigkeiten, wo diese Effekte auftreten und deren Einfluss auf die Bestimmung wichtiger Materialeigenschaften.

Contents

I Developments in torque magnetometry 5

1 Overview of current equipment 7
- 1.1 Torque measurement system 7
- 1.2 Capacitive torque meters 9
- 1.3 Piezoresistive torque meters 11

2 Piezoresistive sensors 13
- 2.1 Introductory remarks 13
- 2.2 Sensitivity calculations and design 14
- 2.3 Electrical connections 24
- 2.4 Sensor fabrication 26
  - 2.4.1 Creating CAD drawings 29
  - 2.4.2 First fabrication run 29
  - 2.4.3 Second fabrication run 30
  - 2.4.4 Mounting samples 33
- 2.5 Test measurements 36
  - 2.5.1 Torque sensor sensitivity measurements 36
  - 2.5.2 Diodes as thermometers 40
- 2.6 Related publication 42

3 Automated measurement system 51
- 3.1 Torque measurement software 51
  - 3.1.1 Description of LabVIEW 52
  - 3.1.2 GPIB bus overview 53
  - 3.1.3 Sending commands via `queues` 54
  - 3.1.4 Sending data using `DataSockets` 54
  - 3.1.5 Torque software overview 56
  - 3.1.6 General VI detailed structure 58
  - 3.1.7 `torque.vi` detailed structure 59
  - 3.1.8 `dataserver.vi` detailed structure 61
  - 3.1.9 `handler.vi` detailed structure 61

3.2 Automation 63
3.2.1 Sequencing language 63
3.3 Helper applications 68
3.3.1 dataviewer.vi 68
3.3.2 selector.vi 69
3.4 Related publication 69

II Magnetic properties of novel superconductors 79

4 Introduction 81
4.1 Materials: the cuprate families 82
4.2 Theories on superconductivity 83
4.2.1 The London model 83
4.2.2 Ginzburg-Landau theory 84
4.2.3 BCS-theory 85
4.2.4 Anisotropic Ginzburg-Landau theory 86
4.2.5 Lawrence-Doniach model 86
4.2.6 Scaling theory 87

5 Vortices and anisotropies 89
5.1 Vortex configurations in $La_{2-x}Sr_xCuO_4$ 91
5.2 Related publication 98

6 Discussion and outlook 107

A Command system 109
A.1 torque.vi commands 109
A.2 dataserver.vi commands 112
A.3 handler.vi VIs commands 112
A.3.1 handlerEGG7265.vi 113
A.3.2 handlerLakeshore.vi 114
A.3.3 handlerBruker.vi 115
A.3.4 handlerAngle.vi 115

Publication list 117

Curriculum Vitae 125

Acknowledgements 127

Introduction

Superconductivity

Superconductivity is known since 1911, when H. Kamerlingh-Onnes measured the resistivity of mercury at cryogenic temperatures. He was the first to succeed in liquefying helium and reaching temperatures only a few degrees above absolute zero. To his surprise, the resistivity of his mercury sample dropped to immeasurably small values below 4.2 K — superconductivity was discovered [Onn11]. It was twenty years later, when W. Meissner and R. Ochsenfeld discovered another peculiar property accompanying the ideal conductivity: the complete expulsion of magnetic fields [MO33]. Only the combination of both zero resistivity and ideal diamagnetism

$$\rho = 0 \qquad \text{and} \qquad \chi = -1$$

qualifies a material to be a superconductor. This state, however, can only be maintained below a critical temperature T_c and below a temperature dependent critical field $H_c(T)$. In the following years, great effort has been invested in the understanding of this state, which many materials enter upon sufficient cooling. J. Bardeen, L.N. Cooper and J.R. Schrieffer managed to explain it in 1957 with their BCS theory [BCS57]. Superconductivity is since then considered a macroscopic manifestation of quantum effects.

This large progress, however, was not matched on the material side for a long time. The highest critical temperature measured until 1986 was 23 K in Nb_3Ge. J.G. Bednorz and K.A. Müller therefore created a sensation, when they reported a T_c of 35 K in a complex compound made of lanthanum, barium and copper oxide [BM86]. Variations of the composition lead to a vast collection of materials, commonly known as the cuprates and critical temperatures skyrocketing within only few years. The current record lies at 139 K, established in 1995 [DCS$^+$95] after a breakthrough in 1993 [SCGO93]. In recent years, other exotic materials were found to superconduct even at surprisingly high temperatures. However, the performance of the cuprates is unrivalled as of now.

Another sensation was caused when the well-known, simple material MgB_2 was found to be superconducting up to 39 K in 2001 by japanese researchers [NNM+01]. The great amount of research performed on this material lead to the conclusion, that it can be understood within the BCS theory. The cuprates, on the other hand, still cannot be described theoretically. Many theories were proposed to explain the appearance of superconductivity at such high temperatures, but none of them satisfactorily agrees with crucial experimental results or is widely accepted in the community. More highly sensitive measurements are needed, especially probing the systematics across different materials. Still the understanding of high-temperature superconductivity is one of the most difficult problems of contemporary condensed matter physics — on both the experimental and the theoretical side.

Magnetometry

The problem of understanding superconductivity in the cuprates is tackled with a variety of theoretical approaches and experimental techniques. The two main categories are the spectroscopic techniques probing microscopic features and the macroscopic investigations of bulk properties. The most important macroscopic techniques are heat capacity, transport (electrical and heat) and magnetisation measurements. The latter is also known as magnetometry. Various methods are known to measure a sample's magnetic moment $\mathbf{m}$. They can be divided into inductive and force detecting techniques. The most frequently used commercial instruments like vibrating sample magnetometers and SQUID (superconducting quantum interference device) magnetometers are of the former type. A magnetic sample is moved through a set of pick-up coils, into which a voltage is induced due to the changing magnetic flux caused by the sample movement. Torque magnetometry is of the latter type. The magnetic moment of a sample is determined by the torque

$$\boldsymbol{\tau} = \mu_0 \mathbf{m} \times \mathbf{H}$$

it experiences in an applied magnetic field $\mathbf{H}$. This technique is particularly sensitive at high magnetic fields, where the otherwise highly sensitive SQUID magnetometers face increasing problems. Torque meters are widely used, in condensed matter physics as well as other research areas such as geology. Initially, samples were suspended on a flexible thread in the magnetic field. The excursion from the equilibrium position was determined optically (see Fig. 1 left). Later, capacitive techniques were introduced. The sample is mounted on a specifically designed, elastic electrode which deforms under the applied torque. The excursion from equilibrium is determined by a

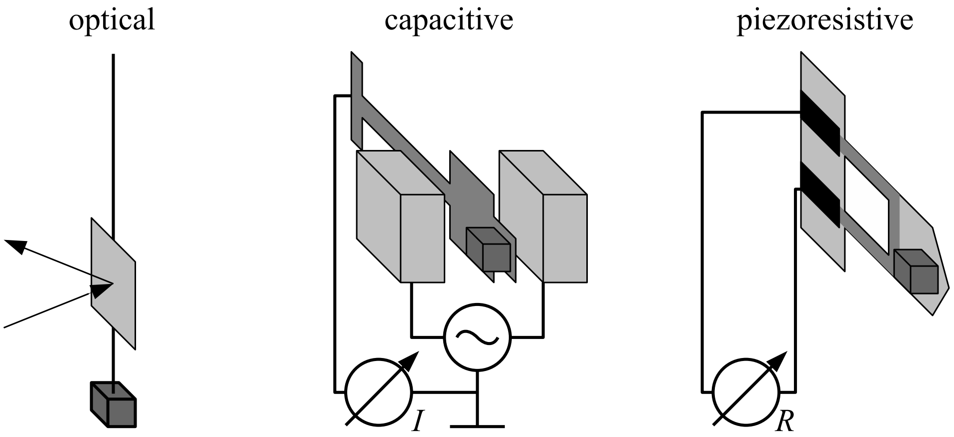

Figure 1: The most common techniques for the readout of torque sensors. The optical readout is widely used, but difficult to implement especially in a cryostat (left). The capacitive and the piezoresistive techniques can easily be incorporated in a cryostat (middle and right). Both are employed at the University of Zurich.

capacitance change of this active electrode relative to a set of external electrodes (see Fig. 1 middle). The capacitive technique is one of the methods employed in the group of H. Keller at the University of Zurich. It reaches outstanding sensitivities, even surpassing the most sensitive commercial SQUID magnetometers.

With the emergence of atomic force microscopy, D. Zech put forward the use of tips designed for this purpose for torque magnetometry in 1995 and demonstrated their suitability [RBZ$^+$96] (see Fig. 1). The measurement principle is based on the piezoresistive effect: certain materials change resistivity when stressed. Doped silicon, widely used in microchip fabrication, has this property. The inclusion of etching procedures into the fabrication processes lead to the emergence of a new branch of semiconductor devices: micro electromechanical systems (MEMS). Nearly arbitrarily complex structures can now be etched from silicon single crystals and equipped with electronic circuitry. M. Willemin made use of such processes and developed piezoresistive sensors specifically designed for torque magnetometry [WRB$^+$98]. The initiation and development was made in collaboration with the *IBM Zurich Research Laboratory* in Rüschlikon. The most recent sensors developed within this thesis were fabricated by the *CSEM Centre Suisse d'Electronique et de Microtechnique SA* in Neuchâtel.

Part I

Developments in torque magnetometry

Chapter 1

Overview of current equipment

1.1 Torque measurement system

Torque magnetometry was introduced at the Physics Institute of the University of Zurich by D. Zech. Since then, the main setup has remained basically unchanged, though large improvements were made to the torque measurement sensors. Basically, the system consists of a rotatable electromagnet and a cryostat which can be equipped with different torque sensors, depending on the needs of a specific experiment.

The magnet is a conventional, water cooled iron yoke magnet built for NMR applications. It is capable of producing fields of $-5\,\mathrm{mT}$ up to $1.5\,\mathrm{T}$ with smooth zero crossing and good homogeneity. At low fields the resolution is better than $0.1\,\mathrm{mT}$. The power supply for the main magnet is remotely controllable by the computer via a General-Purpose-Interface-Bus (GPIB) connection. The electrical and water cooling connections are placed such that a rotation of the magnet by more than 360° is possible. In fact, the magnet can be rotated by nearly two turns. This makes full angle scans possible almost regardless of the sample's initial position. Rotation of the magnet is achieved by three different methods. Rotating by hand is the fastest way. The other possibilities involve using one of two electromotors. There is a large motor for fast, coarse movements and a small motor for slow and precise adjustments. The small motor can be controlled by computer whereas the large one cannot. Thus, the large motor is usable for interactive measurements only, but allows for quick measurements to obtain a general impression of the sample's behavior. The magnet's angular position is measured optically to a precision of 0.01°. The angle readout is connected to the computer via a serial interface.

The helium-flow cryostat passes into the magnet's gap from the top. Tem-

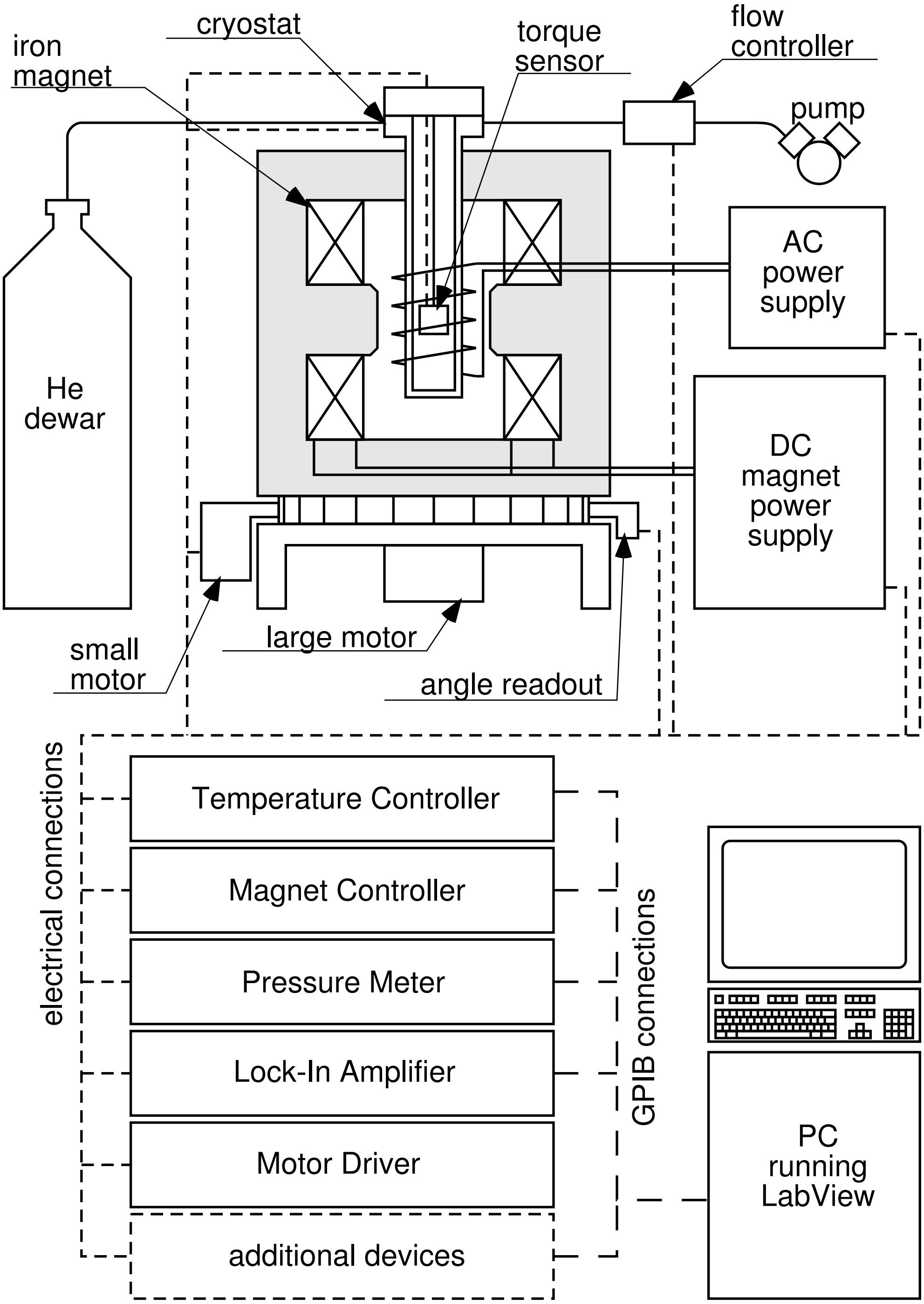

Figure 1.1: Schematic illustration of the torque system installed at the Physics Institute of the University of Zürich. Details are explained in the text.

perature stabilization is obtained either by regulating a heater which is incorporated into the cryostat at fixed coolant flow or by regulating the coolant flow itself. The former is obtained with a dedicated temperature controller; the latter by software running on the attached computer. The temperature controller can be directed remotely via a GPIB connection. Temperatures between $\approx 7\,\mathrm{K}$ and room temperature can be stabilized easily and reliably. Lower temperatures are reachable utilizing more powerful pumps, but this was not necessary in the cases studied in this thesis. A small copper coil is placed outside the croystat but still within the main magnet. This coil generates a small alternating magnetic field which is perpendicular to the main field. It is used to shorten the relaxation time of some magnetic phenomena. Called the shaking technique, it is described in more detail in Ref. [Wil99].

A variety of measurement techniques are employed worldwide to measure the torque of a sample subjected to magnetic fields. In general the sample under interest is fixed on a special sensor which bends or twists under the torque which the sample exerts on it. The amount of movement of the sensor is usually proportional to the applied torque, thus allowing the calculation of the torque if the sensor's movement is known. The different techniques used employ different bending modes of different sensor types and materials and different means of reading out (i.e. measuring) the sensor's movement. Among the most frequently used techniques are optical, capacitive and piezoresistive methods. At the Physics Institute of the University of Zurich two of these readout techniques are used, namely the capacitive and the piezoresistive methods. Both are described in more detail in the following two sections. In either case, a lock-in amplifier (LIA) is used to read out the measured signal. The performance of optical read-out can be superior to the capacitive and piezoresistive ones. However, the alignment of the optics and the usage at cryogenic temperatures poses several problems, especially when samples are to be frequently remounted.

1.2 Capacitive torque meters

When the capacitive readout technique is used, some parts of the torque sensor are fabricated as large thin plates which are placed close to metallic electrodes. These electrodes and the torque sensor form a set of capacitors. The electrodes are excited at a fixed voltage and frequency. The current which is picked up by the torque sensor depends sensitively on its distance from the excited electrodes. In a first approximation this dependence is linear, especially for small deviations from the symmetric position. Figure 1.2 shows the principle of the capacitive torque meter readout. A shielded

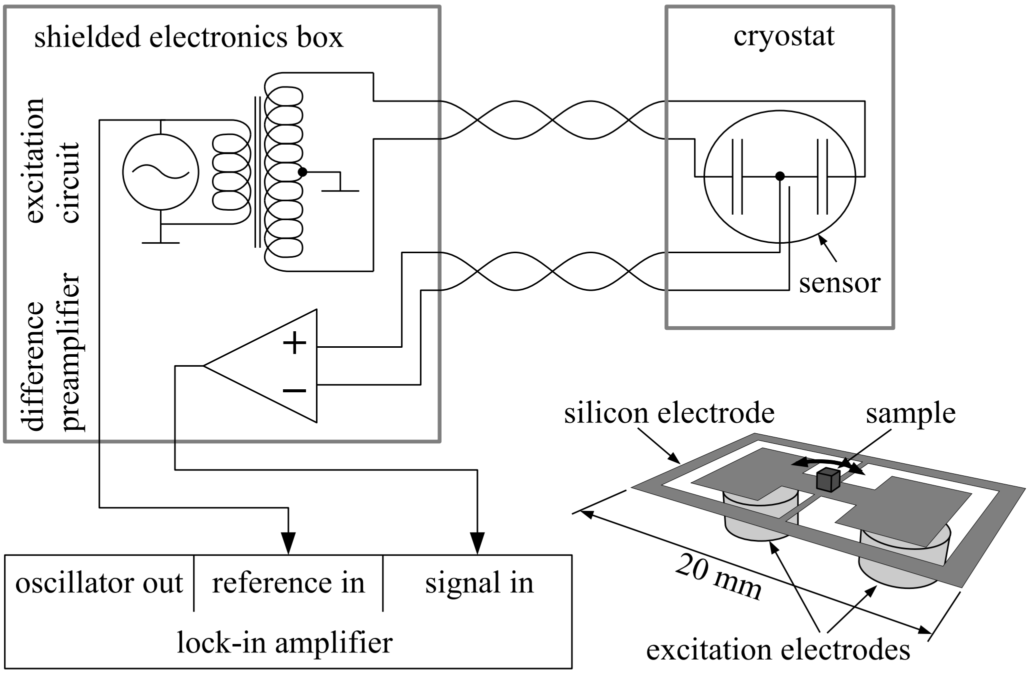

Figure 1.2: Schematic diagram illustrating the readout of the capacitive torque meter (left) and an illustration of the "torsion lever" electrode configuration (right)

box contains the excitation and amplifier circuit, which was designed by M. Willemin [Wil99]. The current which is picked up by the torque sensor is measured using a lock-in amplifier, fixed at the excitation frequency. In order to minimize the background two leads are used to read out the current. The signal lead is connected to the torque sensor whereas the second, the so-called dummy lead, is simply positioned close to the signal lead. Both leads pick up the same background which is cancelled by using a highly symmetric difference amplifier. The electronics are described by M. Willemin in his thesis [Wil99].

Most of the time, doped silicon is used to fabricate the torque sensors by wet or dry etching of wafers to the desired shape and thickness. Of course any elastic and electrically conducting material will do; however, plastic deformation effects usually make measurements with metallic sensors more difficult. In the present work, capacitive torque meters made of silicon about 40 μm thick were used. Outer dimensions are of the order of 10 mm. Capacitive torque sensors are more robust than the piezoresistive ones (see below), especially if made of nonbrittle materials. Due to their large mass and low resonance frequency they are quite sensitive to vibrations. Moreover, several

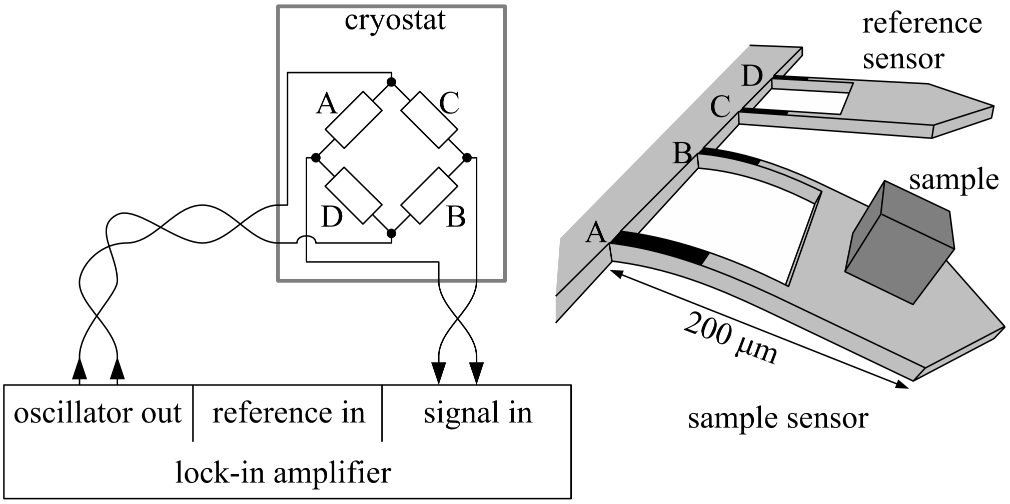

Figure 1.3: Schematic illustration showing the readout principle of the piezoresistive torque meter (left). Two identical torque sensors (right) featuring piezoresistive paths on the surface of their legs (black areas) are connected to form a Wheatstone bridge. The sample is mounted on one sensor.

sources of background couple capacitively into the sensor. Usually large temperature dependencies are observed as well as relatively poor reproducibility. However, if reproducibility is not crucial, they are well suited for high sensitivity experiments, especially for large samples.

1.3 Piezoresistive torque meters

This readout scheme is based on the piezoresistive effect, i.e. the resistivity of certain materials changes upon internal mechanical stress. Doped silicon is generally piezoresistive. Established semiconductor industry techniques allow the micromachining and local doping of silicon single crystals. Thus, nearly arbitrarily complex structures and sophisticated sensors can be created from this material. Structures can be formed according to specific needs, such as sensitivity along special axes. Generally, a sample platform is supported by thin beams carrying piezoresistive paths. These paths are interconnected to form a wheatstone bridge. This allows measurements of extremely small changes of the resistors and simultaneously compensates some background sources like strong temperature and field dependence. The sensor can be operated in two different modes, the static and the dynamic mode. In the former, an alternating voltage is applied to the Wheatstone bridge and a phase sensitive lock-in amplifier is tuned to this excitation frequency. The sensor itself is not moving — hence the name *static mode.* In the dynamic mode, however, a small metallic loop fabricated on the sample platform is fed with an AC current, causing the whole sensor to vibrate in an applied magnetic field. The Wheatstone bridge is now supplied with a DC voltage and the lock-in amplifier tuned to the loop excitation. In the static mode, frequencies and amplitudes around 1 kHz and 1 V, respectively, are used. Figure 1.3 depicts the readout scheme and an illustration of the so-called “two leg lever”.

Piezoresistive torque meters are extremely fragile, because they are only 4 μm thick. This makes the handling with samples difficult, since the force exerted on the sensor while moving the sample on the platform is already likely to break the thin beams. However, their reproducibility is much better than the capacitive sensors, mainly because they can be calibrated with the metallic loop on the sample platform.

Chapter 2

New designs of piezoresistive torque sensors

2.1 Introductory remarks

Based on the previous work on piezoresistive torque sensors carried out by D. Zech and M. Willemin in their PhD theses [Zec95, Wil99], new types of sensors with additional functionality were designed, calculated and fabricated in the present work. In this chapter, the features of the newly designed sensors, the calculation of their sensitivity and their fabrication will be described.

Two versions of piezoresistive torque sensors were copied directly from the existing design, namely the 2-leg and 3-leg cantilevers, developed by M. Willemin and described in his thesis [Wil99]. Differently shaped sensors with higher versatility were calculated, fabricated and tested as well. The following sections deal with these studies. Two iterations of production were carried out. This was principally due to the very high contact resistances resulting from the combination of the metallization and the etching procedures. This rendered the piezoresistive paths useless. Nevertheless, some test measurements were possible on the diodes integrated on the chips and resulted in an undergraduate physics-student advanced practical training.

Fabrication of the sensors was performed by the CSEM Centre Suisse d'Electronique et de Microtechnique SA in Neuchâtel, Switzerland. It is a private company carrying out research and low volume production. It is specialized in micro- and nanotechnology and therefore well qualified for building structures needed for our torque magnetometry sensors. In order to make success as likely as possible, process parameters similar to those employed in previous sensors were chosen. These were the sensor thickness of 4 μm fabricated from single crystal silicon wafers and the use of p-doped

feature	µm
minimal distance	
metal – top outline	2
metal – metal	4
smallest feature	
metal	4
top outline	4
bottom cutout	100
diode size	70 × 80

Table 2.1: Design rules prescribed by the CSEM integration process

regions as piezoresistive paths achieved by implanting boron atoms.

The basic layout of torque sensors is defined by the technology of readout (piezoresistive in this case) and some practical considerations. First, there must be a fairly large platform where samples can be mounted. Second, there must be the possibility to incorporate piezoresistive paths into the structure and, third, these structures must be connected to the outside world via metallic paths. The stress on top of the piezoresistive structures should be as large as possible. The obvious solution to these requirements is to construct platforms held by long, thin legs with piezoresistive paths.

Some constraints on the leg widths are implied by the fabrication technology used. They are formulated in so called design rules which specify minimum distances between different structure parts. The most important design rules are summarized in table 2.1.

2.2 Sensitivity calculations and design

When comparing the sensitivity of different sensor geometries, it is enough to calculate the dependence of the stress on the surface of the sensitive portions of the sensor as a function of the applied torque. This section explains the general technique of such calculations and its application to various sensor designs.

Deformation modes

Depending on the individual leg positions and fixations (and the applied torque direction), the sensor legs deform in different ways. This is best explained using a simple example. Consider a 2-leg lever as shown in Figs. 2.1a and 2.1b. The coordinate system is also shown. Now consider the most

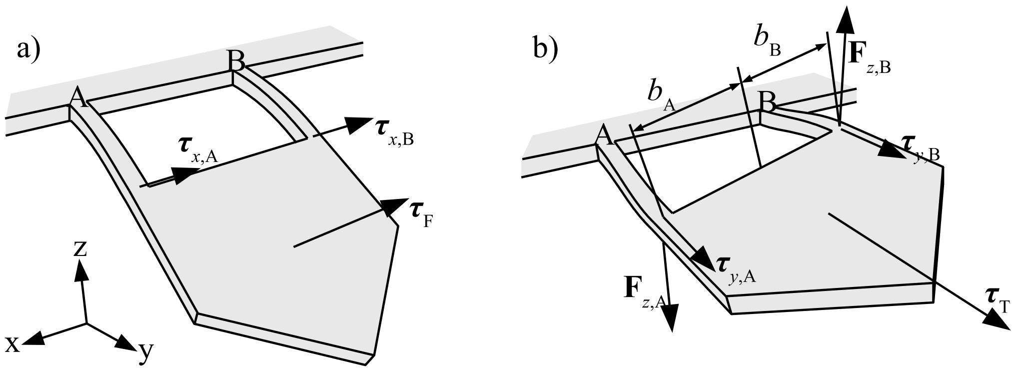

Figure 2.1: Illustration of the two different sensor bending modes *flexion* (a) and *torsion* (b) of a simple cantilever with two legs A and B. The torque applied by the sample is $\boldsymbol{\tau}_{\mathrm{F}}$ ($\boldsymbol{\tau}_{\mathrm{T}}$). It is distributed among the forces and torques acting on the leg ends.

basic measurement situation, where the torque sensor works in the so-called flexion mode. A torque $\boldsymbol{\tau}_{\mathrm{F}}$, applied along the x-axis, causes both legs to bend the same way. Both legs A and B are then subject to individual torques $\boldsymbol{\tau}_{x,\mathrm{A}}$ and $\boldsymbol{\tau}_{x,\mathrm{B}}$. On the other hand, if a torque $\boldsymbol{\tau}_{\mathrm{T}}$ is applied, causing the sensor to tilt along the y-axis, the sensor is stressed in the so called torsion mode. Now the legs are bent in opposite directions. The applied torque $\boldsymbol{\tau}_{\mathrm{T}}$ has been transformed via the lever formed by the platform into a set of opposite forces ($\mathbf{F}_{z,\mathrm{A}} = -\mathbf{F}_{z,\mathrm{B}}$) and torques along the long axes of the legs ($\boldsymbol{\tau}_{y,\mathrm{A}}$ and $\boldsymbol{\tau}_{y,\mathrm{B}}$). It turns out that all sensor deformations can be described by these elemental actions (transverse and parallel torque ($\boldsymbol{\tau}_x$ and $\boldsymbol{\tau}_y$) and transverse force $\mathbf{F}_z$). Other deformations like shear and tension can be neglected. The applied torque $\mathbf{M}$ is therefore always distributed among the different deformation modes of all legs resulting in

$$\boldsymbol{\tau}_{\mathrm{F}} = \boldsymbol{\tau}_{x,\mathrm{A}} + \boldsymbol{\tau}_{x,\mathrm{B}} \tag{2.1}$$

in the flexion mode and

$$\boldsymbol{\tau}_{\mathrm{T}} \quad = \quad \mathbf{b}_{\mathrm{A}} \times \mathbf{F}_{z,\mathrm{A}} + \boldsymbol{\tau}_{y,\mathrm{A}} + \mathbf{b}_{\mathrm{B}} \times \mathbf{F}_{z,\mathrm{B}} + \boldsymbol{\tau}_{y,\mathrm{B}} \tag{2.2}$$

in the torsion mode, where $\mathbf{b}_i$ is the lever which transforms the force $\mathbf{F}_z$ to a torque. Note that in the torsion mode the transverse torque $\boldsymbol{\tau}_{x,\mathrm{A}}$ and $\boldsymbol{\tau}_{x,\mathrm{B}}$ on the two legs is exerted by the platform structure due to a mechanical constraint and does not appear in this summation.

The absolute values of these three elemental actions are readily calculated from the leg deformations θ_x, z and θ_z, which are the flexure angle, the

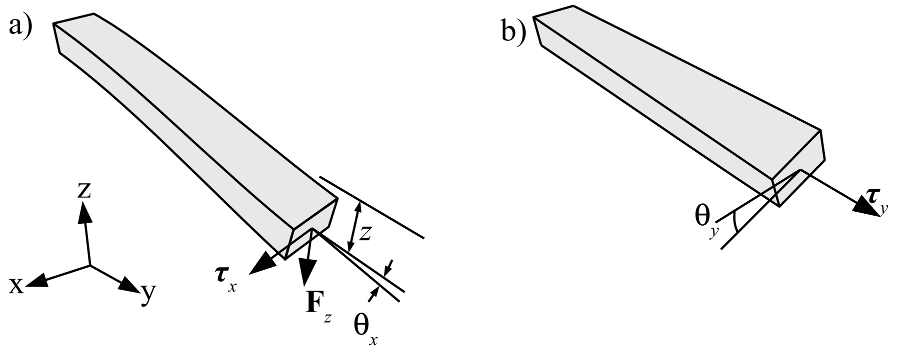

Figure 2.2: Flexion of a single leg due to transverse torque $\boldsymbol{\tau}_x$ and force $\mathbf{F}_z$ (a) and torsion due to longitudinal torque $\boldsymbol{\tau}_y$ (b).

vertical excursion and the torsion angle, respectively (see Figs. 2.2a and 2.2b for illustrations).

Applying a torque τ_x or a force F_z perpendicular to the end of a beam results in a bending θ_x and vertical displacement z of the end face (Note that from this point on only signed absolute values of torque and force will be calculated. Directions are considered separately):

$$\begin{aligned} \theta_x &= \frac{12l}{Ewt^3}\left(\tau_x + F_z\frac{l}{2}\right) && (2.3) \\ z &= \frac{12l^2}{Ewt^3}\left(\tau_x\frac{1}{2} + F_z\frac{l}{3}\right), && (2.4) \end{aligned}$$

where l, w and t are the beam length, width and thickness, respectively as shown in Fig. 2.3a and E is the beam material elasticity modulus. Note that these formulas are obtained with the approximation

$$\sin(\theta) \simeq \tan(\theta) \simeq \theta \tag{2.5}$$

applied. Because the deflection angles involved are small, this is a reasonable assumption. The torsion of a beam is not at all trivial to calculate due to bulging of the internal planes. The approximation

$$\theta_y = \tau_y \frac{6l(1+\nu)}{Ewt^3}\zeta^{-1}\left(\frac{w}{t}\right) \tag{2.6}$$

with $\nu = 0.28$ being the Poisson ratio of silicon and

$$\zeta(\alpha) = 1 - 0.63\alpha^{-1} + 0.052\alpha^{-5} \tag{2.7}$$

for $\alpha > 1$ found in textbooks ([SBL70]) suffices for our purposes. This formula is valid only for $w > t$. In the current fabrication process, where the

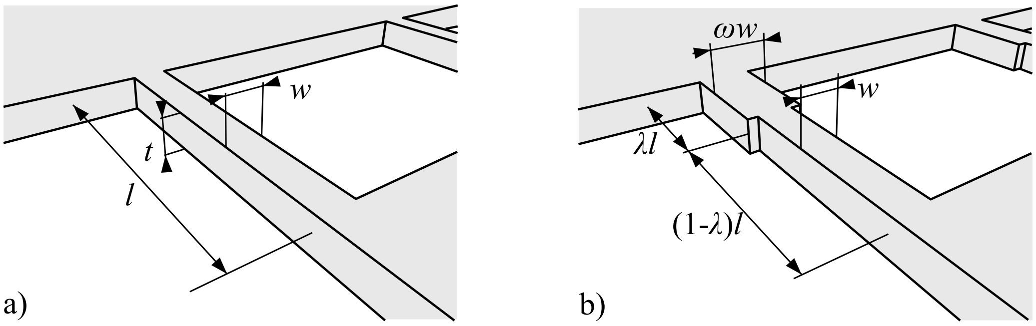

Figure 2.3: a) Dimensions of an individual beam. Width w, thickness (height) t and length l. b) Dimensions of a nonuniform beam. The part λl of the total length is wider by a factor ω. The wide part of the beam is required for fabrication of a metallic layer on top. Only the narrow part is made piezoresistive.

design rules restrict making any leg narrower than the sensor thickness, this is obeyed automatically. Otherwise the roles of w and t must be interchanged for calculation of θ_y. These formulas are readily transformed to

$$\begin{aligned}\tau_x &= \frac{Ewt^3}{6l}\left(2\theta_x - 3\frac{z}{l}\right) &\quad (2.8)\\ F_z &= \frac{Ewt^3}{2l^2}\left(-\theta_x + 2\frac{z}{l}\right) &\quad (2.9)\\ \tau_y &= \frac{Ewt^3}{6l(1+\nu)}\zeta\left(\frac{w}{t}\right)\theta_y. &\quad (2.10)\end{aligned}$$

In order to calculate the sensitivity of a particular sensor geometry, the surface stress needs to be calculated for each leg as a function of torque applied to the whole sensor. For this, each leg's basic deformation parameters θ_x, z and θ_z are expressed by the sensor's net deflection θ. This allows the summation of the individual torque contributions to get the net torque

$$\tau(\theta) = \sum_{j=\text{legs}} \left[\tau_{x,j}(\theta) + b_j F_{z,j}(\theta) + \tau_{y,j}(\theta)\right] \tag{2.11}$$

needed to obtain the sensor deflection θ. For each leg j, the surface stress is

$$\sigma_j(y;\theta) = \frac{6}{wt^2}\left[\tau_{x,j}(\theta) + (l-y)F_{z,j}(\theta)\right], \tag{2.12}$$

which is independent on the material's elasticity modulus E. Depending on the deformation of a specific sensor geometry, the stress on the beam may be constant along its length (if $F_z = 0$ for this leg) or reach a maximum at either end. For the 3leg lever, a compromise was effected by extending the piezoresistive paths halfway along the legs. Parallel torque τ_y causes surface stress as well, but as it is perpendicular to the current flow in the piezoresistive path, it does not contribute to piezoresistive effects.

Both $\tau(\theta)$, the torque acting on the sensor and $\sigma_j(y;\theta)$, the surface stress on each beam are calculated based on the sensor deflection θ. However, for sensitivity calculations, the ratio $\sigma_j(y)$ of surface stress vs torque is needed. As long as θ dependences remain linear, which is the case with approximation (2.5), this is achieved by a simple division

$$\frac{\sigma_j(y)}{\tau} = \frac{\sigma_j(y;\theta)}{\tau(\theta)} \tag{2.13}$$

of Eqs. (2.12) and (2.11). The sensor dimensions and the placement of the piezoresistive paths can then be optimized for highest sensitivity.

Because beams carrying a metallic path need to be wider than bare beams (at least in the presently used fabrication process), the situation of varying width $w(y)$ also has to be considered. This work restricts itself to the simplest case where a portion λl ($\lambda < 1$) of the beam is wider by $\omega > 1$, thus having a width ωw, as illustrated in Fig. 2.3b. Doing the same calculations again, one gets the adaptations of Eqs. (2.8)–(2.10) and (2.12)

$$\tau_x = \frac{Ewt^3}{6l}\left(2\theta_x\xi_3 - 3\frac{z}{l}\xi_2\right)\left(4\xi_1\xi_3 - 3\xi_2^2\right)^{-1} \tag{2.14}$$

$$F_z = \frac{Ewt^3}{2l^2}\left(-\theta_x\xi_2 + 2\frac{z}{l}\xi_1\right)\left(4\xi_1\xi_3 - 3\xi_2^2\right)^{-1} \tag{2.15}$$

$$\tau_y = \frac{Ewt^3}{6l(1+\nu)}\zeta\left(\frac{w}{t}\right)\theta_y\,(\xi_1(\lambda, \zeta(\omega w/t)\omega/\zeta(w/t)) \tag{2.16}$$

and

$$\sigma_j(y;\theta) = \frac{6}{w(y)t^2}\left[\tau_{x,j}(\theta) + (l-y)F_{z,j}(\theta)\right], \tag{2.17}$$

with the correction factors $\xi_i = (1-\lambda)^i(1-1/\omega)+1/\omega$. Note that $\xi_i(\lambda = 0) = 1$ recovers the results for uniform beams. For beam torsion the correction is

$$\theta_3 = \tau\frac{6l(1+\nu)}{Ewt^3}\zeta^{-1}\left(\frac{w}{t}\right)\xi_1' \tag{2.18}$$

with ξ_1' being obtained from ξ_1 by replacing $1/\omega$ by $\zeta(w/t)/\omega\zeta(\omega w/t)$. The stress on the beam's surface [Eq. (2.12)] is also modified to become

$$\sigma(y) = \frac{6}{w(y)t^2}\left(\tau + F(l-y)\right). \tag{2.19}$$

We emphasize that the stress on the leg surface does not depend on the elastic constants of the material used. The elasticity modulus E was introduced for the calculation, but it drops out for the sensitivity ratio $\sigma_j(y)/\tau$. Nevertheless, E of course influences the amount of excursion of the sensor from its equilibrium position for a given applied torque.

The resistance change of a piezoresistive path fabricated on top of a beam is

$$\frac{\Delta R}{R} = \bar{\sigma}\pi_{\mathrm{L}}\beta, \tag{2.20}$$

where $\bar{\sigma}$ is the average surface stress along the entire path. The piezoresistive coefficient for silicon is $\pi_{\mathrm{L}} = 4.5\,10^{-10}\,\mathrm{Pa}^{-1}$ and $\beta < 1$ is a geometrical correction factor needed to account for the fact that current flows not only at the surface (with stress $\bar{\sigma}$), but also deeper, where the stress is smaller.

The value of interest is the resistance change of a piezoresistor due to the applied torque. For small torques, when the approximation (2.5) is valid, this relationship can be expressed by a constant gain factor

$$G = \frac{\Delta R}{R\tau} = \frac{\bar{\sigma}\pi_{\mathrm{L}}\beta}{\tau}, \tag{2.21}$$

in the future simply referred to as the *gain*.

Because π_{L} depends on the silicon doping, β is unknown and due to variations of the sensor fabrication process, the sensitivity prediction from Eq. (2.20) may only serve as a rough estimate. In order to obtain absolute torque measurements, each torque sensor has to be calibrated individually. Nevertheless, Eq. (2.20) serves well for estimating the expected sensitivity of proposed torque sensor designs. Finite element analysis was not used for the deformation calculations of these torque sensors, because the structures studied are quite simple allowing for the exact calculation shown above. Using the described method, it is much easier to systematically study the dependence of the sensitivity on several parameters like the beam length or the placement of the piezoresistive path.

Different sensor geometries are now discussed. In order to improve the electrical insulation between adjacent current paths, the material between them is removed. This makes each leg consist of two individual beams, sometimes connected by small bridges. For a torque sensor with N legs, $2N$ beams have to be accounted for in order to calculate the sensitivity.

Straight 2leg and 3leg levers

These are the designs described by M. Willemin in his thesis [Wil99]. A schematic outline marking the dimensions and a tabular collection of the

dimensions

beam number N	length	width	λ	ω	piezo number	piezo start y/l	piezo end y/l
1	l	w	0		1	0	0.5
2	l	w	0		1	0	0.5
3	l	$2w$	0				
4	l	$2w$	0				
5	l	w	0		2	0	0.5
6	l	w	0		2	0	0.5

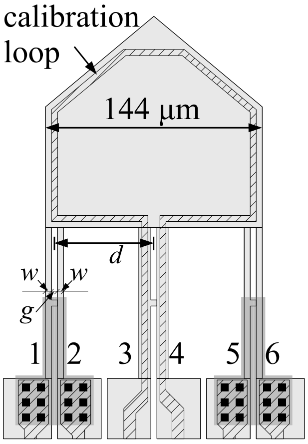

deflection parameters

	flexion				torsion		
N	θ_x/θ	z/θ	b	θ_y/θ	θ_x/θ	$z/\theta = b$	θ_y/θ
1	1	$l/2$	0	0	0	$b + \frac{g+w}{2}$	1
2	1	$l/2$	0	0	0	$b - \frac{g+w}{2}$	1
3	1	$l/2$	0	0	0	$\frac{g+2w}{2}$	1
4	1	$l/2$	0	0	0	$-\frac{g+2w}{2}$	1
5	1	$l/2$	0	0	0	$-b + \frac{g+w}{2}$	1
6	1	$l/2$	0	0	0	$-b - \frac{g+w}{2}$	1

Table 2.2: Illustration of 3leg lever. Dimension specification and deformation parameters for the flexion and torsion modes are given in the tables. In order to calculate the sensitivity of the 2leg lever, the central two beams (3 and 4) are omitted.

parameters of the 3leg lever used for the calculation of its gain are shown in table 2.2. The central leg provides for the current supply for the calibration loop incorporated on top of the sensor platform.

The sensitivity along the x-axis (flexion mode) does not depend on the length of the legs. Its only proportionality is to $w^{-1}t^{-2}$. Thus, it can be increased by choosing a sensor thickness as small as possible and very narrow beams. However, thin beams suffer from a sensitivity reduction due to a smaller β factor in Eq. (2.20).

Along the y-axis (torsion mode) the sensitivity can be maximized by choosing an appropriate distance d between the legs for a fixed leg length l. For the above indicated leg length of 100 µm, the optimum sensitivity is reached around 40 µm. This extremum is rather broad. The optimized calculated sensitivities along the x- and y axis are

$$x\text{-axis:}\qquad G = 3.71 \times 10^6\,\mathrm{Nm}^{-1} \text{ and} \tag{2.22}$$
$$y\text{-axis:}\qquad G = 2.17 \times 10^6\,\mathrm{Nm}^{-1} \tag{2.23}$$

for the 3leg lever and

$$x\text{-axis:}\qquad G = 7.44 \times 10^6\,\mathrm{Nm}^{-1} \text{ and} \tag{2.24}$$
$$y\text{-axis:}\qquad G = 2.92 \times 10^6\,\mathrm{Nm}^{-1} \tag{2.25}$$

for the 2leg lever. It is clear that the 2leg lever in flexion mode reaches the highest sensitivity. This is due to the fact that in this configuration, no deformation energy is lost to inactive parts of the sensor. This also seems to be the highest achievable sensitivity. However, as there is no possibility to incorporate a calibration loop on this sensor, there are situations where this high sensitivity sensor cannot be used.

3leg angled lever

An extension of the 3leg lever, designed for equal sensitivities along the x- and y-axis by the use of tilted legs. By suitable choice of the tilt angle α for the sensor legs, equal sensitivities along both directions can be obtained. Table 2.3 depicts the outline of this sensor design and indicates the dimension and deformation parameters. When optimizing the sensitivities along both axes to be equal, they are both reduced compared to the straight 3leg lever

$$G = 1.57 \times 10^6\,\mathrm{Nm}^{-1}, \tag{2.26}$$

when the angle is $\alpha = 66°$.

Square lever

This design, as shown in table 2.4, was primarily intended to provide a sensor with equal sensitivities along two axes due to its inherent symmetry. When calculating the sensitivity, it turned out that it can become larger than that of the conventional 3leg lever.

For highest sensitivities the piezoresistive paths must be placed near the sample platform, making contacts necessary on top of the legs. These contacts provide for electrical connection between the piezoresistors and the metal wiring on the chip. In order to provide for good contacts, large surfaces are needed which are not present on top of the thin beams. By using only small contacts, the total resistance of the piezoresistive paths increases,

dimensions

leg number N	length	width	λ	ω	piezo number	piezo start y/l	piezo end y/l
1	l	w	0		1	0	0.5
2	l	w	0		1	0	0.5
3	$l\cos(\alpha)$	$2w$	0				
4	$l\cos(\alpha)$	$2w$	0				
5	l	w	0		2	0	0.5
6	l	w	0		2	0	0.5

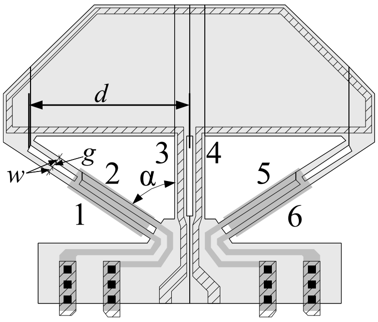

deflection parameters

	flexion				torsion		
N	θ_x/θ	z/θ	b	θ_y/θ	θ_x/θ	$z/\theta = b$	θ_y/θ
1	$\cos(\alpha)$	$\frac{l}{2}\cos(\alpha)$	0	$\sin(\alpha)$	$\sin(\alpha)$	$d + \cos(\alpha)\frac{g+w}{2}$	$\cos(\alpha)$
2	$\cos(\alpha)$	$\frac{l}{2}\cos(\alpha)$	0	$\sin(\alpha)$	$\sin(\alpha)$	$d - \cos(\alpha)\frac{g+w}{2}$	$\cos(\alpha)$
3	1	$\frac{l}{2}\cos(\alpha)$	0	0	0	$\frac{g+2w}{2}$	1
4	1	$\frac{l}{2}\cos(\alpha)$	0	0	0	$-\frac{g+2w}{2}$	1
5	$\cos(\alpha)$	$\frac{l}{2}\cos(\alpha)$	0	$\sin(\alpha)$	$-\sin(\alpha)$	$-d + \cos(\alpha)\frac{g+w}{2}$	$-\cos(\alpha)$
6	$\cos(\alpha)$	$\frac{l}{2}\cos(\alpha)$	0	$\sin(\alpha)$	$-\sin(\alpha)$	$-d - \cos(\alpha)\frac{g+w}{2}$	$-\cos(\alpha)$

Table 2.3: Illustration, dimension specification and deflection parameters of the individual legs of the angled 3leg lever for the flexion and torsion mode.

dimensions

leg number N	length	width	λ	ω	piezo number	piezo start y/l	piezo end y/l
1	l	w	λ	2	1	λ	1
2	l	w	λ	2	1	λ	1
3	l	w	λ	2	2	λ	1
4	l	w	λ	2	2	λ	1
5	l	$2w$	0	1			
6	l	$2w$	0	1			
7	l	$2w$	0	1			
8	l	$2w$	0	1			

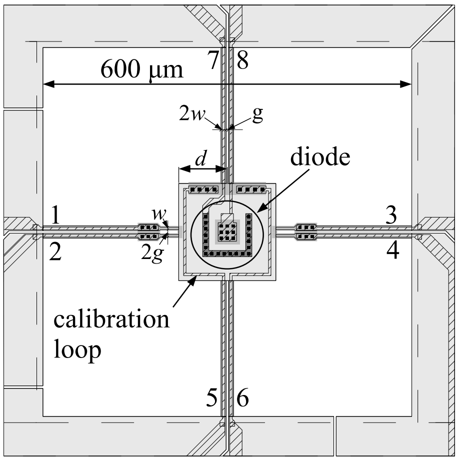

deflection parameters

N	θ_x/θ	z/θ	b	θ_y/θ
1	1	$-d-\frac{l}{2}$	$-d$	0
2	1	$-d-\frac{l}{2}$	$-d$	0
3	1	$d+\frac{l}{2}$	$-d$	0
4	1	$d+\frac{l}{2}$	$-d$	0
5	0	$\frac{g+\omega w}{2}$	$\frac{g+\omega w}{2}$	1
6	0	$-\frac{g+\omega w}{2}$	$-\frac{g+\omega w}{2}$	1
7	0	$\frac{g+\omega w}{2}$	$\frac{g+\omega w}{2}$	1
8	0	$-\frac{g+\omega w}{2}$	$-\frac{g+\omega w}{2}$	1

Table 2.4: Illustration, dimension specification and deflection parameters of the individual legs of the square lever. Only one deformation mode is useful for torque measurements. Beams 7 and 8 are not present in our high sensitivity torque sensor.

thereby reducing the sensitivity. Due to several uncertainties influencing the contact resistance during the fabrication process, this effect is hard to estimate. A compromise between reduction of the contact surface and broadening the beams was found solely by choosing a design that “looked good”.

Its larger complexity compared to the 3leg sensors allows for the variation of several parameters. The following versions were considered for fabrication:

1. **Symmetric.** All four legs are equally shaped. Two opposing legs can be used together in order to measure torque along one axis. Due to its inherent symmetry, the sensitivities along both axes are the same. Due to the lack of a calibration loop, absolute calibration must be performed by other means.
2. **With calibration loop.** One leg is used to supply current for a calibration loop incorporated on the platform similarly to the 3leg lever. This version has only three legs.
    (a) **Basic.** The leg parameters were chosen in order to reach a sensitivity similar to the 3leg lever. As the dimensions are similar to the 3leg lever, this version is expected to be quite robust.
    (b) **Hires.** A version with very long legs for a higher sensitivity. This is expected to be very fragile and therefore very likely to break when mounting samples or even already during the fabrication.
    (c) **Inverted.** Same dimensions as the version **basic**. The piezoresistors are placed at the base of the legs instead of near the platform. This was done to have a backup solution in case the placement of the contacts on top of the beams causes serious problems.
3. **Loop&diode.** Similar to version **basic**, only that the fourth leg is added and used for the connection to a diode fabricated on top of the sensor to provide for temperature measurements directly at the sample position.

Figure 2.4 shows schematic illustrations of the versions with a calibration loop. The detailed dimension and deflection parameters for the **loop&diode** version (3.) are shown in table 2.4.

2.3 Electrical connections

As shown in Fig. 1.3 on page 11, the sensor piezoresistors are connected to form a wheatstone bridge. One half of the bridge is formed by the sensor

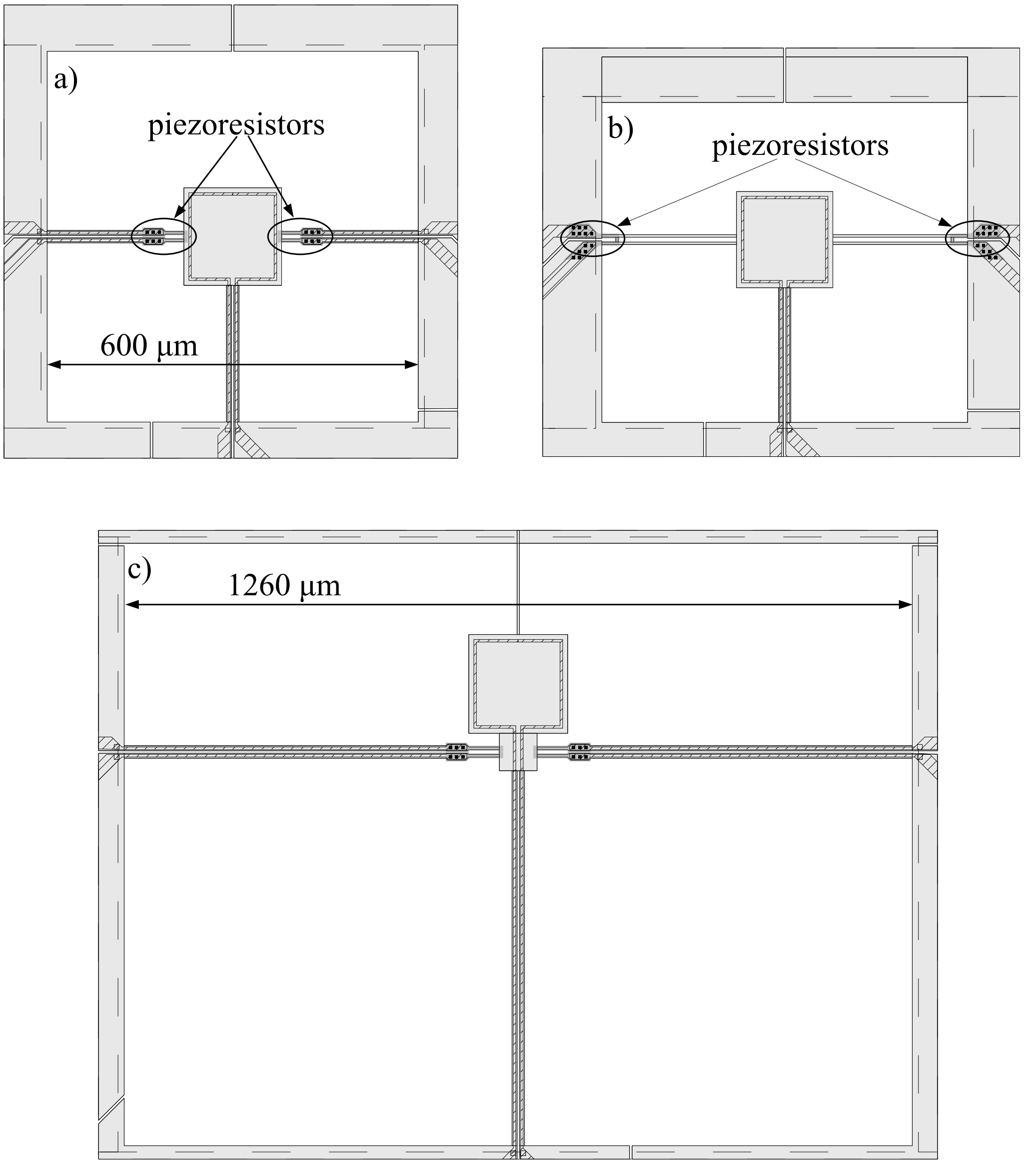

Figure 2.4: Schematic illustrations of the sensor versions belonging to the square class of sensors. a) **Basic** with loop, b) **inverted** with different piezoresistor placement and c) **hires** with a higher gain.

bearing the sample. In order to minimise temperature and field dependences as well as noise, a second sensor is used for the other half of the bridge, instead of external resistors. All sensors are designed such that under an applied torque, the absolute resistance change of the two piezoresistors is equal. Thus the measured voltage across the bridge is

$$U \approx U_0 \frac{\Delta R}{2R} = \frac{U_0}{2} G\tau, \tag{2.27}$$

with U_0 being the bridge excitation voltage.

2.4 Sensor fabrication

Two fabrication runs were performed in which the sensors were designed using computer aided design software and the files sent electronically to the manufacturing company, *CSEM Centre Suisse d'Electronique et de Microtechnique SA*. Fabrication starts from a single crystal silicon wafer of 300 µm thickness and consists of a sequence of steps. In brief, the process can be described as follows:

1. **Oxidation.** A very common step is the growth of a thin silicon dioxide layer in a furnace. This layer protects the underlying silicon, but can be etched away selectively if necessary.

2. **Photoresist.** The whole wafer is coated with a thin layer of photoresistive material.

3. **Exposure.** Through a patterned mask, the photoresist is irradiated with ultraviolet light, thus causing it to harden.

4. **Dissolution.** The wafer is dipped in a solvent to remove the unirradiated photoresist. This completes the transfer of the mask pattern onto the wafer.

5. **Application.** This step might consist of various individual steps. In the end, a certain property of the wafer acquires the structure of the mask. This can be the metallization, the implantation of dopant atoms or an etch process. Depending on the features to be created, the photoresist layer cannot be used directly. In such a case, the structure is first transformed on the underlying silicon dioxide, which makes the step more complicated.

6. **Removal.** The photoresist layer is removed if it was not removed already during the previous step.

Several such sequences make up the whole fabrication of a chip. The details of the fabrication are property of CSEM SA, the fabrication company. Therefore, they are not reproduced here.

Different types of chips can be fabricated on one wafer, provided that they share similar production steps. For each sequence, a separate mask is needed. One mask contains the information necessary for one fabrication step for the whole wafer and can cover hundreds of different chips. However, imperfections of the fabrication process cause some of the chips to contain errors which make them unusable. It is therefore inadvisable to create a mask set for hundred different chips. In this work, only four different chips were designed. Each was placed a dozen times on the masks, distributed uniformly over the wafer. The uniform distribution is advisable since imperfections might preferably occur at certain positions on the wafer. Above all, the area close to the wafer edge is the most error-prone. A chip placed at the outer perimeter of the wafer should also be present near the center. Figures 2.6 and 2.7 each show one half of a wafer.

Six masks are needed for the fabrication of the torque sensors. Their designation and purpose is given in the following list. An illustration is provided in Fig. 2.5.

top outline is the mask defining the actual sensor structure. It defines the areas which are protected from the etchant and thus remain intact. All other material is removed down to a defined depth.

bottom outline is the mask defining the dimensions of the chip supporting the sensor. The process is similar to the one defining the top outline.

metal defines the placement of the metallic lines needed for connecting the piezoresistive structures to the outside world. Bond pads (square areas $200 \times 200\ \mu\mathrm{m}^2$) are defined where thin aluminum wires can be attached.

contact defines openings in the insulating silicon dioxide layer covering the whole wafer. These openings provide for an electrical contact between the metal and the underlying bare (usually doped) silicon.

p-implant defines the areas where boron is implanted in the wafer, thus making it a p-type semiconductor. Usually, only a thin surface layer is affected. The piezoresistive paths, being p-type silicon, are created this way.

n-implant equivalent to the **p-implant** mask, but used for creating n-type semiconducting areas on the wafer by phosphorus implantation. Suit-

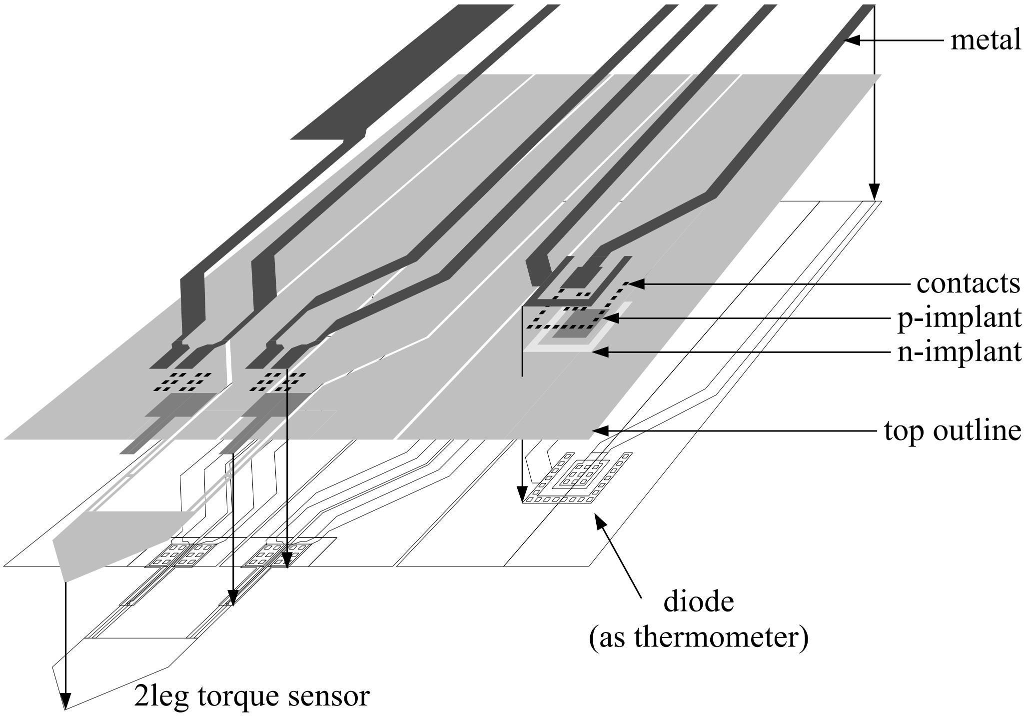

Figure 2.5: Schematic of the mask usage during the fabrication process. The masks *top outline* (grey), *p-implant* (dark grey), *n-implant* (light gray), *metal* (black) and *contacts* (small, dark grey). The *bottom outline* mask is not shown.

able combination of p- and n-type areas allows for the creation of silicon diodes.

In order to achieve a uniform thickness, silicon-on-insulator (SOI) wafers are used as the starting material. A thin layer of silicon dioxide is buried at a fixed depth below the wafer surface. This layer effectively stops the etching performed from the back side. The final, thin sensor structures then consist of the top layer of fixed thickness.

2.4.1 Creating CAD drawings

Electronic drawings were created with the computer aided design (CAD) software *AutoCAD LT®* [aut]. The outlines of the individual structures were drawn using closed *polylines*. For each mask, a separate *layer* was used. *Layers* are a widely used concept in CAD software in order to separate drawing items used for different detail levels or thematic groups. It also facilitates the import of the created drawings into the mask creation apparatus.

2.4.2 First fabrication run

In the first run the following sensor chips were submitted:

2leg chip with 4 levers, interconnected for 2 sensor pairs.

3leg loop chip with 4 3leg levers including calibration loops, interconnected for 2 sensor pairs.

3leg diode chip with 4 levers featuring a diode to serve as a thermometer instead of the calibration loop.

square normal chip with 4 fully symmetric levers for two axis measurements.

square loop chips with 4 levers with a calibration loop. The leg opposing the leg holding the loop wires was equipped with a piezoresistor to enable a rough torque measurement along the axis perpendicular to the main measurement axis.

square loopdiode chip with 4 levers with a calibration loop and a diode for thermometry on the sample platform.

square high chip with 4 fully symmetric levers for a higher sensitivity.

square XHires chip with 2 fully symmetric levers for even higher sensitivity. The sample platform was quite small, probably even unusably small, and the legs were frighteningly long. The choice for this chip was merely a trial of feasibility of such a fragile structure instead of a usable sensor.

A 100 mm wafer was filled with 92 such chips (see Fig. 2.6 for an illustration) and fabrication was started with 4 wafers. Due to problems combining the wet etching procedures used to micromachine the sensor structures and an appropriate metallization, very few chips were obtained from this first fabrication run. Moreover, internal stress led to breakage of two wafers, leaving only two fabricated wafers.

Very bad contact resistances between the metallized layer and the piezoresistive material made these sensors unusable. Nevertheless, the diode characteristics could be measured on some specimen in the low current regime. These measurement were carried out by an undergraduate student within the framework of advanced practical work.

Few sensors were broken, showing that the fabrication process and subsequent handling of the wafers and chips was not as critical as feared. Due to insufficient etching, there were large remaining parts of the membrane connected only via the thin legs. Even these large areas did not cause the legs to break during fabrication and handling.

It was only after the production was finished that a design error was discovered. The backside opening needed to bare the sensors of the square type sensors were all together missing. Consequently no square sensors could be studied concerning their fragility.

The extremely small sample platform of the square XHires lever turned out to be really too small for practical use. Consequently the design of this sensor version was reworked.

2.4.3 Second fabrication run

Based on the experience obtained from the first sensor fabrication the design was reworked and the strategy altered somewhat to account for the faced problems. These problems and their solutions are addressed now.

Problem: Missing bottom opening in the square sensors. The problem was a misinterpretation of the design. To the eye, the created layout looked correct, because there was a square in the design looking like the opening. This square was not subtracted from the rest of the shape to form a hole but was simply overlapped. The design program used can only

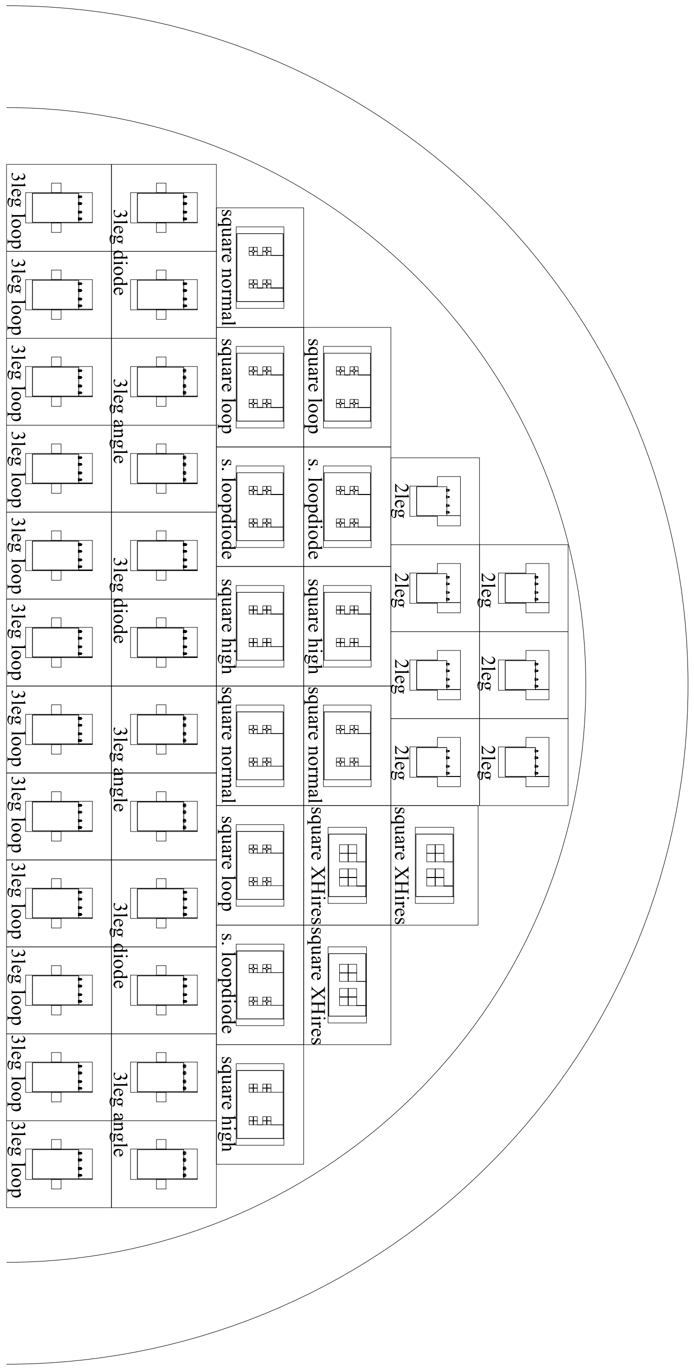

Figure 2.6: Illustration of the layout of the sensor chips on the 100 mm wafer of the first fabrication run. The smaller semicircle denotes a 85 mm diameter circle within which the whole design must be situated. The drawing is to scale. Only the upper half of the *top outline* mask is shown. The lower half is symmetric.

represent the drawing as a wireframe. The drawn polygons cannot easily be filled.

Solution: A program was created to run over the drawing files and collect only the raw drawing data and omit everything else (like color and view definitions). A fresh drawing file was created using this collected data. Additionally a check is performed looking for degenerate vortices and eliminating them. These are drawing points being situated at the same coordinates, causing their connecting line to have zero length. Such occurrences caused problems when importing the data into the CSEM fabrication process. The created clean drawing was then imported into blender$^{\text{TM}}$[ble], a 3D visualization program. There the designed structure can be rotated and looked at from different angles almost like the finished structure. Flaws like the missing bottom opening could easily be seen this way.

Problem: Too small sample platform on the high resistivity square sensors.

Solution: The design was reworked. No more sensors were created for two axis measurements. The sample platform was divided into a narrow part where the sensor legs are attached and a wide part where the sample can be mounted. Moreover, the calibration loop was incorporated on all sensor versions. Unused legs were removed instead of putting a piezoresistor on it. Thus no more two axis torque sensors were fabricated. On the other hand, sensitivity was gained.

Problem: Different sizes of the sensor chips required printed circuit boards to be specially fabricated for each type individually. This made producing these PCBs expensive and in the end, some were completely useless because the chips for which they were designed were not usable.

Solution: Only two principally different chip sizes were chosen and consequently only two PCB sizes were necessary of which the one for 2leg and 3leg sensors already was present. When creating the PCB for the square sensors the design was made such that it was possible to mount also the 2leg and 3leg sensors on them.

Solving these problems led to a smaller number of different chip designs, but fabricated in larger quantities. The following chips were fabricated in the second run.

2leg. Chip with four levers, interconnected for two sensor pairs.

3leg. Chip with two interconnected sensor pairs. One pair is equipped with calibration loops, the other with a diode thermometer.

Square normal. Chip with two sensor pairs. The interconnection has to be provided externally. One pair is the **loop&diode** version, the other the simple **loop** version.

Square high. Chip with two sensor pairs. The interconnection has to be provided externally. One pair is the **hires** version for high sensitivity, the other the **inverted** version with a different piezoresistor placement.

At the time of fabrication, there was no need for the full symmetric sensor type for two-axis measurements. Therefore, no such designs were incorporated.

This time, fabrication started from ten 100 mm wafers, filled with about 50 of these chips (see Fig. 2.7). Only one half of the wafer was filled with torque sensors, as the other half was occupied by sensors designed for heat capacity and thermal conductivity measurements. This was a collaboration with researchers from Prof. Schilling's group at the University of Zurich. A scanning electron micrograph of a fabricated square **hires** torque sensor is shown in Fig. 2.8.

The results from this second fabrication run were satisfactory. The results varied between different wafers, since they were not processed simultaneously. Detailed results are presented in the following section 2.5.

2.4.4 Mounting samples

Experience collected with sample mounting trials on the sensors from the first fabrication run shows that, as long as the legs are not touched directly, the sensors allow considerable bending along the axis for which they are designed. Of course the sample and sensor smallness combined with the normal human tremor make it difficult to touch the sensor such that it is bent only in the allowed way. Flexible mounting tools are therefore much more suitable than rigid metallic ones, even if the latter can be manufactured much thinner. The most efficient way to mount a sample is the following two step approach:

1. Place the sample on the sensor by hand using a flexible tool. A one hair paintbrush or a single human hair does fine. This leaves a great deal of flexibility in rotating the tool which is needed to succeed in getting the sample off the tool and on the sensor.

2. Maneuver the sample into the correct position and orientation using the thinnest available acupuncture needle attached to a micromanipulator.

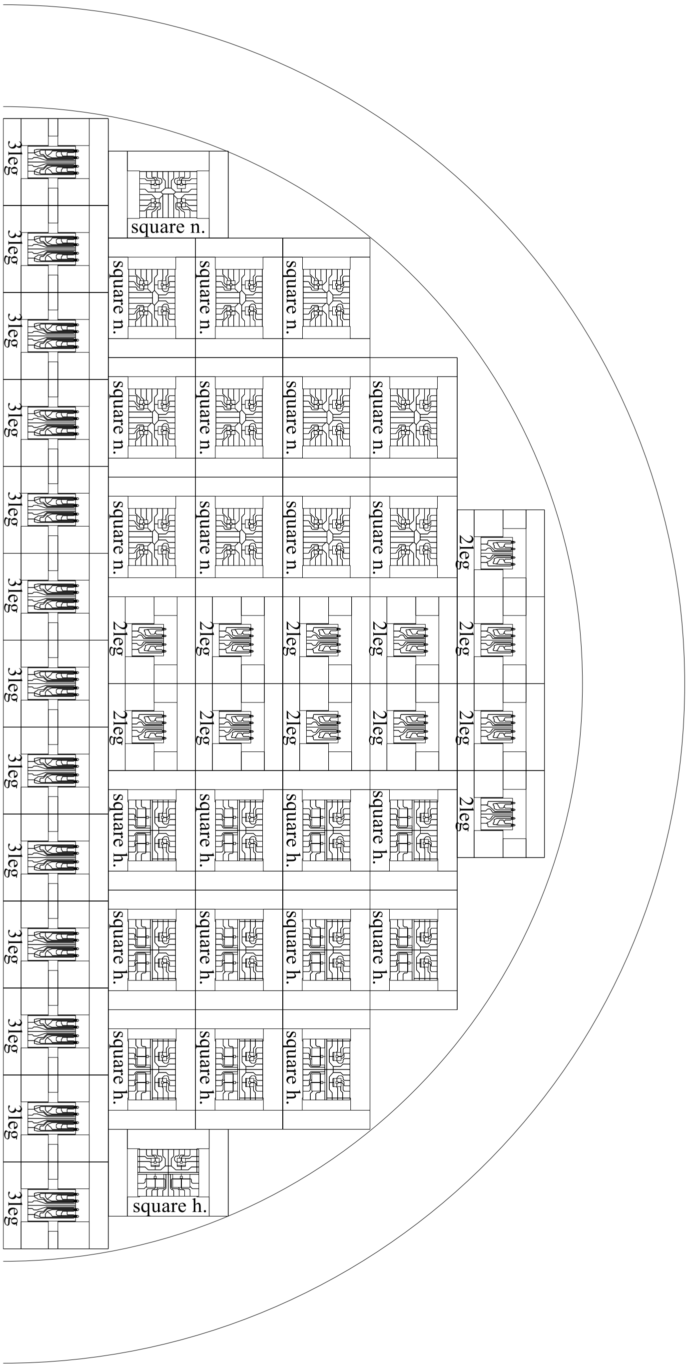

Figure 2.7: Illustration of the layout of the sensor chips on the 100 mm wafer of the second fabrication run. The smaller circle denotes a 85 mm diameter circle within which the whole design must be situated. The drawing is to scale. Only the upper half of the *top outline* mask is shown. The lower half is occupied by sensors for heat capacity and thermal conductivity measurements.

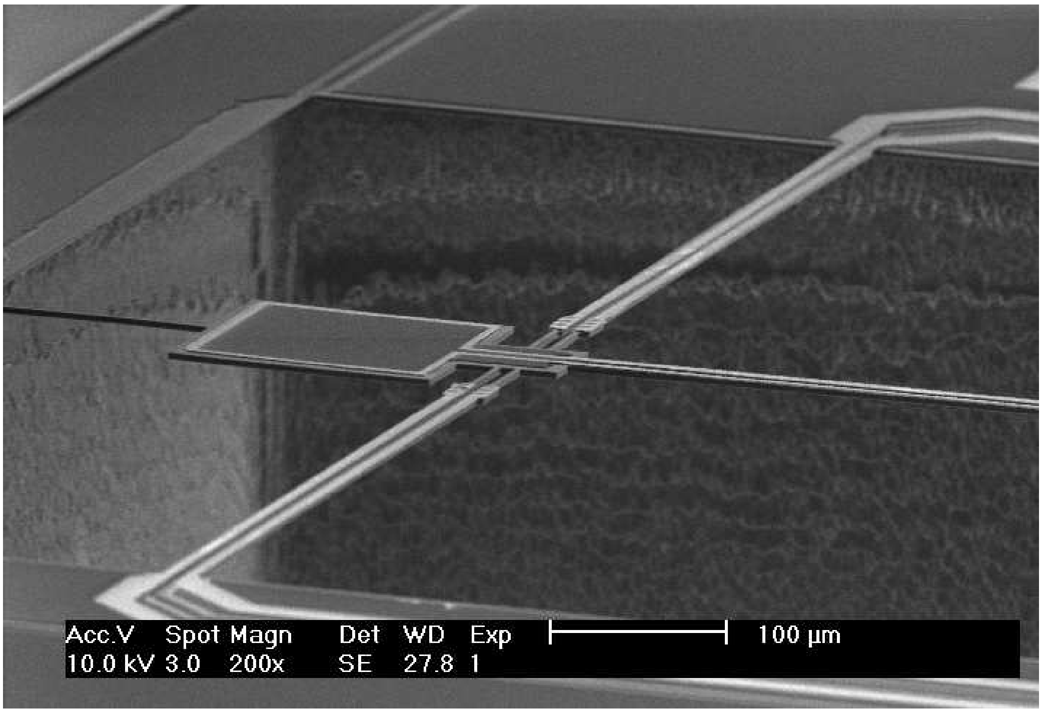

Figure 2.8: Scanning electron micrograph of a square **hires** torque sensor with high sensitivity. The sample platform with the calibration loop is at the center of the picture. Two legs, each consisting of two beams, carry metallic lines needed for contact to the piezoresistive paths close to the sample platform.

> The extremely thin tip allows accurate positioning of the sample on the sensor. This, however, is only possible in combination with the micromanipulator and great care is needed in order not to break the sensor.

A small amount of nonmagnetic vacuum grease (such as Apiezon® N grease [Api]) is suitable to ensure sticking of the sample to the storage container, the mounting tool and finally to the torque sensor. It can be removed completely (with xylene and subsequent rinsing with isopropyl alcohol for Apiezon® N). A too large amount of grase may lead to loss of the sample, because the frozen grease drop can come off due to the sensor bending.

2.5 Test measurements

In order to verify the calculated sensitivities for the various sensor designs different test measurements were performed. The performance of the torque sensors was investigated by two different methods. One was the measurement of a ferromagnetic sample. By measuring it using the torque sensors and comparing the results with measurements of the saturation moment obtained from SQUID measurements allows the determination of the torque meter's sensitivity and therefore its performance. The second method is the usage of the calibration loop present on some sensors. Of course only those sensors featuring such a loop can be studied this way. These results are presented in section 2.5.1.

All chips and some sensors feature a silicon diode made from p- and n-doped regions. The functioning of these devices was checked in two steps. At first, the voltage-current characteristic was checked and second, the temperature dependence of the voltage drop at a fixed excitation current was measured. These results are described in section 2.5.2.

2.5.1 Torque sensor sensitivity measurements

Thanks to their integrated calibration loop, the sensitivity of piezoresistive torque sensors can be easily measured without mounting a specific sample. It is even possible to measure the actual sensitivity during a real measurement.

As shown in Fig. 1.3 on page 11, the piezoresistive torque sensors are connected as a wheatstone bridge for the readout. For some sensors, part of these connections are made already on the chip, but most of them have to be completed. Usually the bridge is then driven at an AC voltage and read out with a lock-in amplifier (LIA) for low noise detection. The excitation frequency can be chosen freely, but usually it is set to 1.5 kHz. Thus, it is far from both the line frequency of 50 Hz which might be disturbing and the resonance frequencies of the sensor which range from above 100 kHz for a bare sensor down to 5 kHz with a mounted sample [WRB+98]. The noise ΔU of the voltage which is measured by the LIA and which is proportional to the torque [Eq. (2.27)] on page 26), is constant

$$\Delta U \approx 1\,\mu\mathrm{V} \tag{2.28}$$

and mainly determined by the electrical connections and the readout electronics. Thus, a larger excitation voltage U_0 automatically causes higher sensitivity. On the other hand, heating effects become more important. We therefore chose

$$U_0 = 1\,\mathrm{V}, \tag{2.29}$$

directly delivered from the LIA internal oscillator. In this respect, the piezoresistive torque sensors are very easy to operate.

Calibration with the current loop

There are three independet parameters which can be varied for a calibration measurement with the current loop. They are

field strength H and

field orientation θ of the applied magnetic field, as well as the

current I through the loop itself.

The torque of such a single turn loop inside a magnetic field **H** is

$$\begin{aligned} \boldsymbol{\tau} &= \mu_0 \mathbf{m} \times \mathbf{H} = \mu_0 I \mathbf{A} \times \mathbf{H} && (2.30)\\ \tau &= \mu_0 I A H \sin(\theta), && (2.31) \end{aligned}$$

where A is the area enclosed by the current loop. Figure 2.9 shows a typical calibration measurement using the current loop.

Calibration with a Ferromagnetic Sample

A calibration of the sensor can also be obtained with a sample of known magnetic moment. Small pieces of magnetic audio tape proved useful for this purpose. Such a piece is first measured in a SQUID mangetometer and afterwards mounted on a torque sensor. However, the usable field range is limited by the coercive field of the sample material. Fortunately, the maximum field $\mu_0 H = 1.5\,\mathrm{T}$ suffices to saturate the tape sample, and fields up to

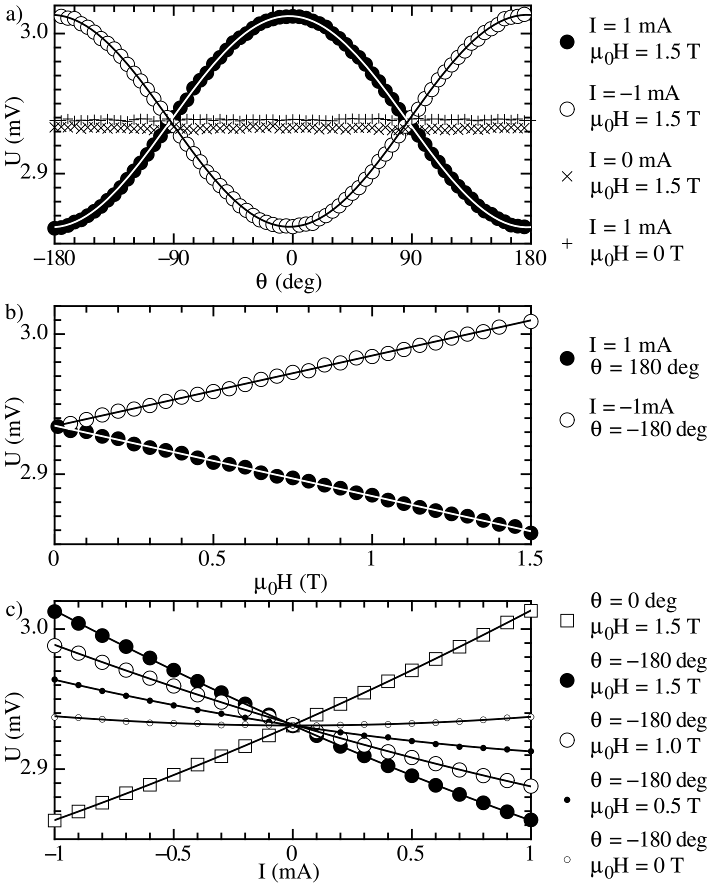

Figure 2.9: Torque sensor calibration with the integrated current loop. a) Angle dependence at constant current and field. b) Field dependence at constant current and angle. c) Current dependence at constant field and angle. The deviations from linearity in the current dependence (c) are likely to be caused by crosstalk between the current loop and the piezoresistors. This effect varies strongly between different exemplars of the same design. This data was taken with a square **hires** sensor (see Section 2.2).

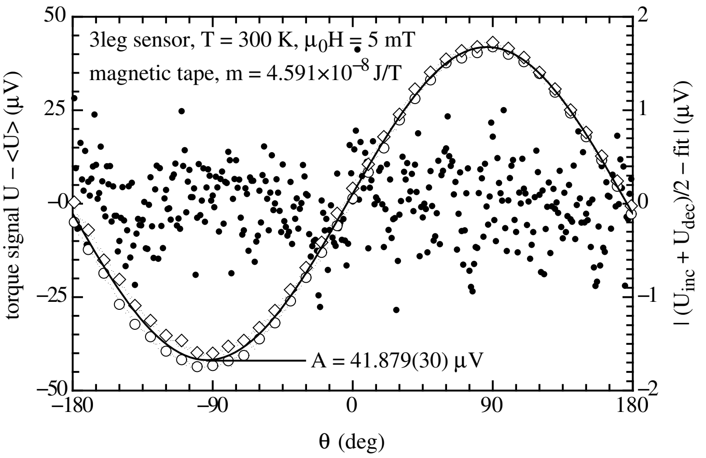

Figure 2.10: Calibration measurement of a 3leg lever taken with a small piece of magnetic tape ($m = 4.591 \times 10^{-8}\,\mathrm{Am}^2$) in an applied magnetic field of $\mu_0 H = 1\,\mathrm{mT}$. Open symbols denote the measured voltage signal with a constant offset subtracted (left scale). Deviations from the sine fit (solid curve) are due to a continous drift of the readout voltage. Filled dots show the difference between the signal, corrected for drift, and the fit (right scale).

$\mu_0 H = 1\,\mathrm{mT}$ do not cause measurable hysteresis. The angle dependence of the torque is perfectly described by $\sin(\theta)$ within experimental errors. However, measurements with $\mu_0 H = 5\,\mathrm{mT}$ already show significant deviations proportional to $\sin(2\theta)$, indicative of remagnetization effects. Such calibration measurements therefore are not suitable for linearity checks across large field ranges. On the other hand, the large magnetic moment

$$m \approx 10^{-8}\,\mathrm{Am}^2, \tag{2.32}$$

(compared to $m \approx 10^{-11}\,\mathrm{Am}^2$ of the current loop) allows good measurements at low fields where the current loop produces a torque which is too small and therefore is not usable. A typical calibration measurement taken with a 3leg sensor is shown in Fig. 2.10.

Temperature dependence

The temperature dependence of the gain varies strongly with temperature. For some sensors, the gain even changes sign at a temperature around 40 K. However, no systematic variations have been observed so far, which is why the effect is not yet understood. Therefore, each newly mounted sensor has to be calibrated separately, before it can be used. Figure 2.11 shows the

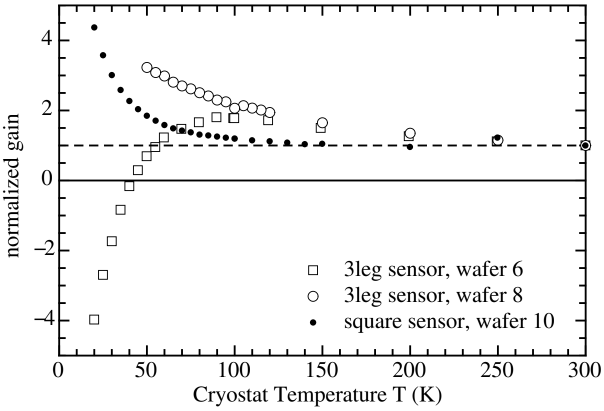

Figure 2.11: Temperature dependence of the normalized gain $G(T)/G(300\,\mathrm{K})$ for different sensors. Deviations from the optimum (dashed line) vary strongly between differently processed wafers.

temperature dependence of the gain of various torque sensors, normalized to the room temperature value. The sign change observed at low temperature is puzzling. A measurement of the temperature dependence of the resistance of a single piezoresistive path, shown in Fig. 2.12, shows a peculiarity at similar temperatures. This behavior is still under investigation. For the operation of the torque sensors, its understanding is not crucial. Only the knowledge of its presence is necessary. Since piezoresistive torque sensors are well known to exhibit a strong temperature dependence, a precise calibration at various temperatures is necessary in any case.

2.5.2 Diodes as thermometers

Usually, the sample temperature is measured at a spot very near the sample. However, this place can usually be thermally quite far away from the sample. As a trial, a diode was incorporated in the sample platform to enable the possibility of measuring the temperature of the sample directly, possibly detecting small changes during measurements. Even though diodes experience strong influence from magnetic fields, this possibility may turn out to be useful.

Diode characteristic

The current-voltage curve of a diode fabricated on a torque sensor chip was measured and found to agree with the expectations. It is reproduced in Fig. 2.13.

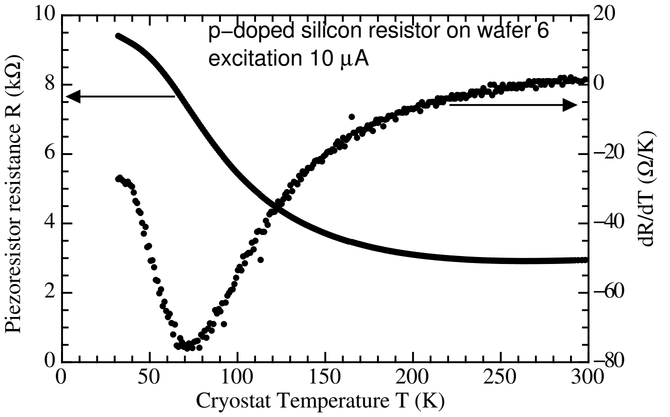

Figure 2.12: Temperature dependence of the resistance (left scale) of a piezoresistor. The derivative with respect to temperature is shown on the right scale.

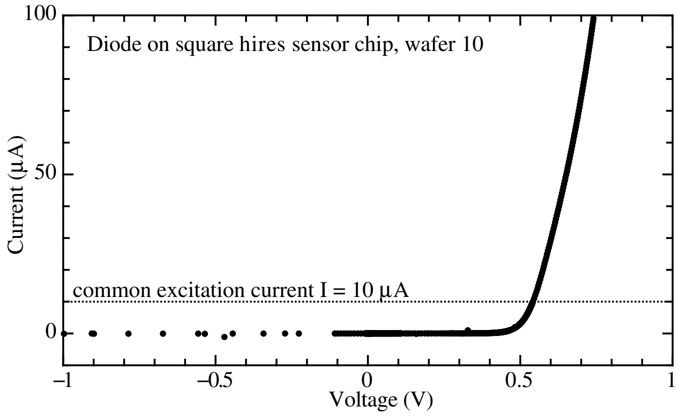

Figure 2.13: Current-Voltage curve for a diode on a torque sensor.

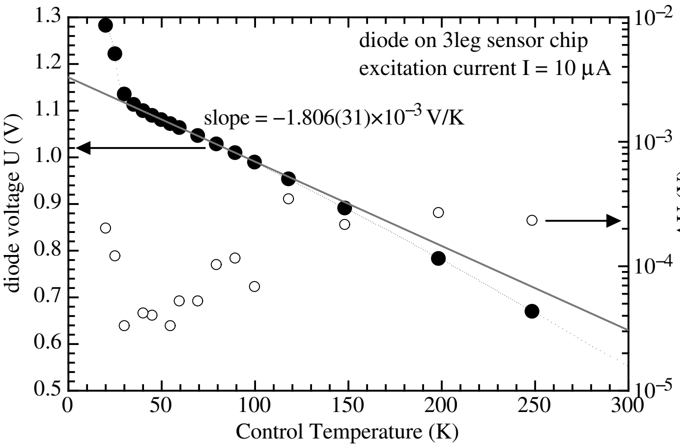

Figure 2.14: Temperature dependence of the voltage drop of a diode on a torque sensor at constant forward bias ($I = 10\,\mu\mathrm{A}$) in zero field. The standard deviation and the total difference between the extremal measurements are shown on the right scale.

Temperature dependence

Diodes are used as thermometers by biasing them with a constant current in the forward direction and measuring the voltage drop of 0.7 . . . 2 V. This shows a nearly linear region down to about 20 K, below which the voltage suddenly increases, making the diode more sensitive to temperature changes. The diodes on the torque sensors show this characteristic behavior, as shown in Fig. 2.14. At an average slope of the diode voltage of -1.806×10^{-3} V/K and a maximum standard deviation of the voltage measurement of $2\times10^{-4}V$, the standard deviation of the temperature measurement amounts to

$$\Delta T \approx 0.1\,\mathrm{K}.$$

Field dependence

As mentioned above, diodes experience a strong influence from magnetic fields. Figure 2.15 shows the deviation of the voltage drop from the zero field signal due to a magnetic field.

2.6 Related publication

Novel Sensor Design for Torque Magnetometry
Stefan Kohout, Joseph Roos and Hugo Keller
submitted to Rev. Sci. Instrum.

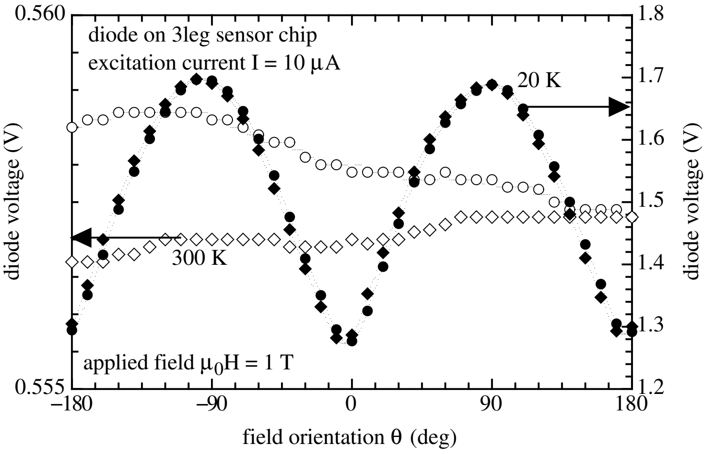

Figure 2.15: Field dependence of the voltage drop of a diode on a torque sensor at constant forward bias ($I = 10\,\mu\mathrm{A}$) and constant temperature in an applied magnetic field $\mu_0 H = 1\,\mathrm{T}$. Open and filled symbols are from measurements obtained at 300 K and 20 K, respectively. Diamonds and circles represent measurements obtained during increasing and decreasing angle, respectively.

Novel sensor design for torque magnetometry

Stefan Kohout,* Josef Roos, and Hugo Keller
Physik-Institut, Universität Zürich, Winterthurerstrasse 190, 8057 Zürich, Switzerland
(Dated: May 24, 2006)

Torque magnetometry is a powerful method to determine a sample's magnetic properties. In a torque magnetometer, the sample under interest is mounted on a suitable sensor, the core part of the instrument. Piezoresistive atomic force microscope tips proved to be very useful torque sensors and have already been optimized for the specific needs of torque magnetometry. However, this type of sensor did not offer the possibility of measuring torque along two perpendicular directions simultaneously. In this article we demonstrate a fundamentally new sensor design based on the piezoresistive readout technique, which offers a large variability of measurement modes. With a symmetric arrangement of the sensor legs, concurrent two-axis measurements are easily possible with two separate readout circuits. Furthermore, the variability can be exploited by fabricating a thermometer on the sample platform to directly measure the sample temperature. Test measurements are in good agreement with elasticity calculations.

I. INTRODUCTION

The investigation of high temperature superconductivity has posed ever higher demands on instrumentation. For magnetization measurements, superconducting quantum interference devices (SQUID) and torque magnetometry proved the most sensitive techniques, capable of coping with tiny samples. While SQUIDs are best at low magnetic fields, the sensitivity of micro-fabricated torque magnetometers is unrivaled in the high field regime[1–5]. Torque sensors were first torsion balances with optical or capacitive readout[6–8]. With the advancements of technology in atomic force microscopy (AFM)[9], the use of tips fabricated for AFM were first suggested as torque sensors by Zech and coworkers[1] in a collaboration of our group and the IBM Zurich Research Lab. The design was later specialized for the requirements of torque magnetometry by Willemin *et al.*[10]. Such specially designed and highly sensitive torque sensors allowed several demanding experiments in high temperature superconductivity to be carried out, such as the observation of flux lattice melting[11], the determination of the in-plane anisotropy[12], the measurement of the oxygen isotope effect on the in-plane magnetic penetration depth[13] or the systematic investigation of the lock-in effect[14].

Current specialized torque magnetometers reach sensitivities of $< 10^{-12}\,\mathrm{Nm}$,[10,15,16] the torque experienced by a sample with a magnetic moment of $< 10^{-12}\,\mathrm{Am}^2$ in a field of 1 T. However, due to variations during the fabrication process, an accurate calibration of each individual sensor is vital for reliable results. Sensors are therefore equipped with designated structures, enabling a calibration even in situ, while a sample is mounted on the sensor. Moreover, current sensors can be used to measure the torque along two orthogonal directions. Unfortunately, a rewiring is needed to enable measurement along the second axis, making simultaneous measurements along both axes very difficult. Due to the geometrical asymmetry, the sensitivities for measurements along both axes are unequal.

The sensors presented in this article are fully symmetric, enabling inherently equal sensitivities along two orthogonal directions. Both torque components can be measured simultaneously, because an individual pair of piezoresistive paths is used for either measurement axis. Furthermore, this sensor design can easily be varied to accommodate different needs. We present versions with a high resolution or with a semiconductor diode fabricated on the sample mounting platform suitable for accurate temperature measurements. Such sensors will enable new, sophisticated measurement modes to be exploited.

II. BASIC PRINCIPLES OF TORQUE MAGNETOMETRY

Using a torque sensor, the magnetic moment $\mathbf{m}$ of a sample in an external magnetic field $\mathbf{H}$ is determined via the torque

$$\boldsymbol{\tau} = \mu_0 \mathbf{m} \times \mathbf{H} \tag{1}$$

it experiences. Of course, only samples with anisotropic or hysteretic magnetic properties can be investigated. As opposed to experiments with inductive techniques like vibrating sample magnetometers or SQUIDs, torque measurements are usually very fast, because the torque acting on a sensor is measured nearly instantaneously by the detection of a resistance change, a capacitance change or the position change of a mirror by optical means. Thus, torque measurements can usually be performed in varying magnetic field strengths or orientations. Torque magnetometers are increasingly sensitive at high magnetic fields, where a SQUID's sensitivity is reduced.

Piezoresistive torque sensors are generally fabricated from single crystal silicon wafers. The piezoresistive paths needed for the detection of the stress in the structure due to an applied torque are incorporated by selective implantation of boron atoms forming p-doped semiconductor regions. A Wheatstone bridge circuit is very well suited to detect the small resistance changes of the piezoresistive paths. To increase the performance of the bridge and to reduce temperature drifts, two identical

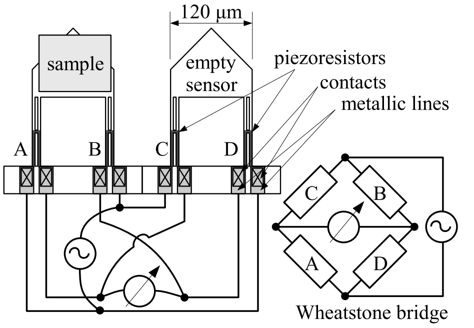

FIG. 1: Wheatstone bridge connection of two identical 2leg[10] sensors. One sensor carries the sample, the other serves as a reference. This electrical scheme is used equivalently with other sensor designs.

sensors, each carrying two piezoresistors are ideally used to form the circuit, as the two 2leg sensors[10] shown in Fig. 1. Such 2leg sensors are not part of this work. They are merely shown as an example of previously used torque sensors. Usually an AC excitation of 1 V and ≈ 1 kHz is applied with a voltage measurement using a lock-in technique in phase with the excitation. All sensors described in this article were fabricated by the *Centre Suisse d' Electronique et de Microtechnique SA*, a Swiss company specialized in small volume production. The starting material were silicon-on-insulator wafers yielding a sensor thickness of 4 µm.

III. SHAPE CONSIDERATIONS

The piezoresistive torque sensors used so far[10] allowed the measurement of torque along two orthogonal directions, but only at reduced and unequal sensitivity and not simultaneously. The torque sensor design described in this article and shown in Fig. 2 overcomes these limitations. A separate pair of piezoresistors is used for each measurement axis. Both pairs can be incorporated into independent Wheatstone bridge circuits allowing a highly sensitive detection of the resistance changes. From this design, a great variability can be derived by using two legs for other purposes than carrying piezoresistive paths. They can be equipped with current carrying metallic lines. Each leg consists of two individual beams. Thus, a leg can carry two metallic lines. As shown in Fig. 3, these metallic lines can be used to supply a diode on the sample platform or a metallic loop for calibration purposes. In the figure the version *loop & thermometer* with a calibration loop (supplied by leg D) and a diode (supplied by leg C) for temperature measurements is shown. Piezoresistive paths are fabricated on legs A and B close to the sample platform. For the *fully symmetric* version shown

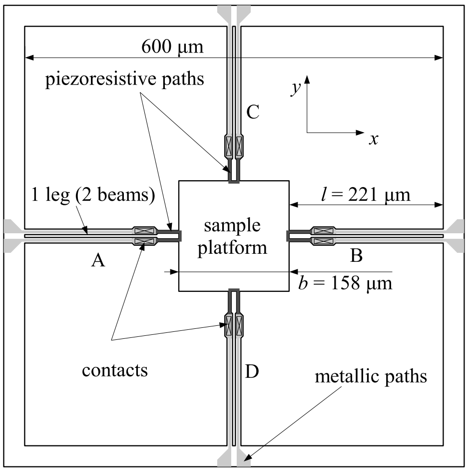

FIG. 2: New, fully symmetric piezoresistive sensor design for simultaneous two-axis measurement. The base material is silicon. Light and dark gray areas denote the metalization layer and p-type doped areas, respectively. Contacts between them are situated at the crossed rectangles. The sample platform is situated in the middle. The piezoresistors on the horizontal (A,B) and vertical (C,D) legs serve to measure torque along the y- and x-axis, respectively.

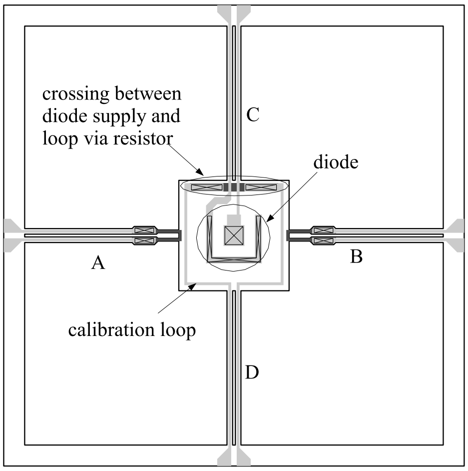

FIG. 3: The *loop & thermometer* configuration of the square sensor. Legs A and B carry piezoresistive paths, whereas leg C connects the diode situated on the sample platform, and leg D supplies the calibration loop. The piezoresistive path on the upper side of the platform is a part of the calibration loop and is used to enable the crossing with the metallic lines supplying the diode.

in Fig. 2 legs C and D are equipped with piezoresistive paths, allowing the simultaneous two-axis torque measurements with equal sensitivities. By simply omitting the diode and removing leg C, a slightly higher sensitivity is reached (*simple* version). The leg length can be varied to accommodate for robustness (shorter legs) or higher sensitivity (longer legs). The *high gain* (Fig. 4) version is doubled in size compared to the one shown in Fig. 2. For test purposes a *low gain* variation was designed with piezoresistive paths at the base of the legs instead of near the sample platform.

IV. GAIN CALCULATIONS

The gain, defined as resistance change per applied torque, of different sensor geometries was calculated from basic elasticity theory, assuming that both the sample platform and the base structure are infinitely rigid. The beams are designed very thin and long, making shear stress unimportant. Tensile forces along the beam can be neglected as well, if only small deflections (small torques) are considered. A torque τ acting on the platform is thus distributed among forces and torques acting on the beams attached to the platform. The resulting stress $\bar{\sigma}$ on the beam surface leads to a resistance change $\Delta R/R$ due to piezoresistivity which is detected in the end. The sensitivity of any sensor geometry can be determined by first calculating the gain

$$G = \frac{\Delta R}{R\tau} \tag{2}$$

of each piezoresistive path present (see Appendix). The sensitivity of the whole sensor can then be determined based on how the individual paths are interconnected.

A summary of calculated and measured gains of different torque sensor geometries is given in Table I. The 2leg and 3leg shapes are included for comparison with the work of Willemin *et al.*[10]. The gain of the 2leg cantilever is unachievable by any other geometry. For low noise measurements without the need of absolute calibration, it is the best choice. The reliable calibration of the 3leg sensor comes at the price of reduced gain. Moreover, simultaneous measurement along two directions is not possible with these sensors. The normal sized square lever is a matching alternative to the 3leg sensor, offering additional temperature measurement directly at the sample site. For more sensitive, calibrated measurements, the square lever with longer legs as shown in Fig. 4 can be employed, since the gain of this design increases with the ratio

$$\eta = \frac{\text{leg length}}{\text{sample platform width}} = \frac{l}{b}. \tag{3}$$

In the limit $\eta \to \infty$, the gain approaches that of the 2leg cantilever. However, practical restrictions limit the gain achieved with the square sensor to about 80 % of the 2leg lever, but still preserving the advantageous calibration possibility.

sensor shape	gain G ($10^6\,(\mathrm{Nm})^{-1}$)	
	calculated	measured
2leg[a]	7.44	–[b]
3leg[a]	3.72	4.35(4)
square (*low gain*)	2.20	2.25(1)
square (*loop & thermometer*)	3.08	3.56(24)
square (*fully symmetric*)	3.18	–[c]
square (*simple*)	3.30	3.42(2)
square (*high gain*)	5.11	5.28(2)

[a] Same design as used by Willemin *et al.*[10].
[b] No calibration loop present.
[c] Not yet fabricated.

TABLE I: Calculated and measured gains $G = \Delta R/\tau R$ of piezoresistive paths of different sensor shapes.

V. GAIN MEASUREMENTS

A piezoresistive resistance change is detected most easily and sensitively by connecting four resistors to form a Wheatstone bridge as shown in Fig. 1. This reduces temperature drifts and noise because the whole bridge is in the cryostat.[10] If two resistors are active and two are constant (half bridge), the measured voltage across the bridge is $U = U_0 G\tau/2$ with U_0 being the bridge excitation voltage. We use AC excitation (1.5 kHz) with $U_0 \approx 1\,\mathrm{V}$, a compromise between resolution and heating effects. The signal U is measured with a lock-in amplifier in phase with the excitation. The read out noise level of the lock-in amplifier is usually $\Delta U \approx 0.1\,\mu\mathrm{V}$. Since mechanical vibrations of the sensor are unimportant, this yields an equivalent torque noise $\Delta\tau = 2\Delta U U_0^{-1} G^{-1} \approx 10^{-13}\,\mathrm{Nm}$ for a typical piezoresistor gain $G \approx 2 \times 10^6\,(\mathrm{Nm})^{-1}$. Larger gains and excitation voltages cause lower torque noise levels.

The gain of the fabricated devices was measured both with the integrated calibration loop, and using a piece of magnetic audio tape whose magnetic moment was measured in a commercial SQUID magnetometer beforehand. The area $A = 1.9 \times 10^{-8}\,\mathrm{m}^2$ enclosed by the metallic loop on the sample platform is derived from the design of the sensors and is therefore accurately known. Figure 4 shows a scanning electron micro graph of the square *high gain* sensor which was used for the calibration loop measurement shown in Fig. 5. The metallic lines support a maximum current of $I = 1\,\mathrm{mA}$, yielding an easily measurable torque of $\tau \approx 10^{-11}\,\mathrm{Nm}$ in a field of 1 T. By reducing the field or the current by a factor 1000, a reliable reduction of the torque below the expected noise level is easily possible. The voltage $U = 0.5 U_0 GAIH \sin\delta$ is measured across the Wheatstone bridge. H is the applied field's magnitude and δ the angle it encloses with the sample platform plane. Figure 5 shows the angle-, field- and current dependence of the *high gain* version torque sensor (see also Table I). The fits with a sine function to the angle dependence demonstrate the excellent perfor-

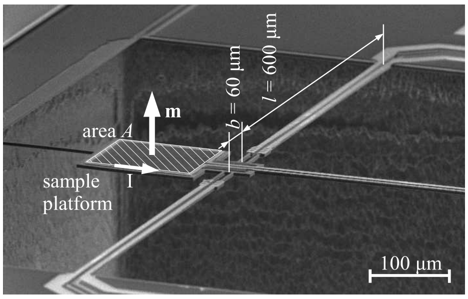

FIG. 4: Scanning electron micro graph of a square *high gain* sensor such as used in the measurements shown in Fig. 5. A current I flows through the calibration loop enclosing an area A and generates a well-known magnetic moment $\mathbf{m}$.

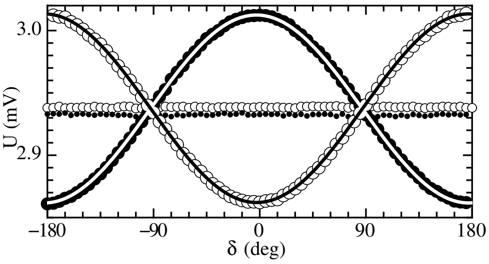

FIG. 5: Current loop calibration measurements of a square *high gain* sensor (Table I). The angle δ dependence at constant current I and field H of the Wheatstone bridge voltage U was recorded during continuous rotation of the magnet. Curves are fits with a simple sine function. Large filled (open) symbols: $\mu_0 H = 1.5\,\mathrm{T}$ and $I = +(-)1\,\mathrm{mA}$. Small filled symbols: $\mu_0 H = 1.5\,\mathrm{T}$, $I = 0\,\mathrm{mA}$. Small open symbols: $\mu_0 H = 0\,\mathrm{T}$, $I = +1\,\mathrm{mA}$.

mance of the sensor. The small offset ($\approx 2.94\,\mathrm{mV}$) due to an imbalance of the bridge is inevitable, but negligible in measurements.

VI. DISCUSSION AND OUTLOOK

We presented a new shape of piezoresistive torque sensors allowing a large variability of measurement modes. The fabricated sensors were shown to agree well with elasticity calculations. Their magnetic background signal was determined to be small enough to be of no concern. Unfortunately, the sensitivity is strongly temperature dependent, increasing nonlinearly by a factor of 8 from 300 K to 20 K. However, thanks to the metallic loop allowing calibration even during a measurement and to the fact that the Wheatstone bridge stays in balance nevertheless, this does not impede measurements down to about 15 K. Because the temperature dependence stems purely from fabrication specific issues and is entirely independent of the sensor geometry, these effects were not discussed in this article. They will be addressed in future fabrication runs.

The ability of simultaneous torque measurement along two perpendicular axes will allow further investigations of the layered high temperature superconductors. Measurements of torque with the field applied parallel to specific crystallographic symmetry planes will be feasible more easily. The field should be rotated such that the torque about one axis remains zero ensuring perfect alignment with the crystallographic axes. Simultaneous measurement of the other torque component will then allow the determination of important physical properties of the sample under investigation, such as the in-plane anisotropy. Eventually, such measurements could also lead to hints about the symmetry of the superconducting order parameter[12]. In another setup, the relaxation enhancement effects of the so-called shaking procedure[17] could be studied in detail. This procedure consists of the application of a small secondary AC-field H_{AC} perpendicular to the main applied field H and results in a much earlier reaching of the equilibrium orientation of the magnetisation after changes in the main magnetic field. The additional torque measurement axis provided by our sensors would allow the measurement of the effects this AC-field has while it is applied, leading to new insight into the relaxation processes of vortices in high-temperature superconductors.

APPENDIX A: GAIN CALCULATION

The torque τ acting on the sample platform and causing it to deflect by an angle θ, is distributed among transverse and longitudinal torques (τ_{T}, τ_{L}) and transverse forces (F) on each beam attached to the platform[18]:

$$\tau(\theta) = \sum_{j=\mathrm{beams}} \left[\tau_{\mathrm{T},j}(\theta) + b_j F_j(\theta) + \tau_{\mathrm{L},j}(\theta)\right], \qquad \text{(A1)}$$

where b_j is the distance of the fixation point of the beam to the platform from the platform rotation axis. The contributions from each beam (length l, width w and thickness t) can be calculated by[18]

$$\begin{aligned} \tau_{\mathrm{T}} &= \frac{Ewt^3}{6l}\left(2\theta_{\mathrm{T}} - 3\frac{z}{l}\right) && \text{(A2)} \\ F &= \frac{Ewt^3}{2l^2}\left(-\theta_{\mathrm{T}} + 2\frac{z}{l}\right) && \text{(A3)} \\ \tau_{\mathrm{L}} &= \frac{Ewt^3}{6l(1+\nu)}\zeta\left(\frac{t}{w}\right)\theta_{\mathrm{L}}, && \text{(A4)} \end{aligned}$$

where θ_{T}, z and θ_{L} are the deflection parameters of the individual beams, expressed in terms of the sensor deflection θ. E and ν are Young's modulus and Poisson's ratio, respectively. $\zeta(n) = 1 - 0.63n + 0.052n^5$ is an approximation for $n \leq 1$ found in textbooks[19]. Correction were applied for the beams used in our square sensors which have a non-uniform width along their length.

Longitudinal torque τ_L causes shear stress on the surface perpendicular to the piezoresistive path and therefore does not contribute directly to the gain. The surface stress along the leg length $(0 < y < l)$ is

$$\sigma(y) = \frac{6}{wt^2}\left[\tau_\mathrm{T} + (l - y)F\right]. \tag{A5}$$

The average stress $\bar{\sigma}(\theta)$ along the piezoresistive path then gives the resistance change $\Delta R/R$ due to the deflection θ of the sensor. The gain (resistance change per applied torque) is then the simple division

$$G = \frac{\Delta R}{\tau R} = \frac{\bar{\sigma}(\theta)}{\tau(\theta)}\pi_\mathrm{L}\beta, \tag{A6}$$

where $\pi_\mathrm{L} = 4.5 \times 10^{-10}\,\mathrm{Pa}^{-1}$ is the longitudinal piezoresistive coefficient of the material and $\beta \approx 0.8$ is a geometrical factor, taking the finite depth of the piezoresistive path into account.

---

[*] current e-mail address: `kohout@physik.unizh.ch`

[1] D. Zech, J. Hofer, H. Keller, C. Rossel, P. Bauer, and J. Karpinski, Phys. Rev. B **53**, R6026 (1996).

[2] H. G. Schnack, R. Griessen, P. Noordeloos, and K. Heeck, Physica C **266**, 285 (1996).

[3] C. Rossel, P. Bauer, D. Zech, J. Hofer, M. Willemin, and H. Keller, J. Appl. Phys. **79**, 8166 (1996).

[4] C. Bergemann, A. W. Tyler, A. P. Mackenzie, J. R. Cooper, S. R. Julian, and D. E. Farrell, Phys. Rev. B **57**, 14387 (1998).

[5] M. J. Naughton, Phys. Rev. B **61**, 1605 (1999).

[6] J. H. Condon and J. A. Marcus, Phys. Rev **134**, A446 (1964).

[7] R. Griessen, M. J. G. Lee, and D. J. Stanley, Phys. Rev. B **16**, 4385 (1977).

[8] M. Qvarford, K. Heeck, J. G. Lensink, R. J. Wijngaarden, and R. Griessen, Rev. Sci. Instr. **63**, 5762 (1992).

[9] M. Tortonese, R. C. Barrett, and C. F. Quate, Appl. Phys. Lett. **62**, 834 (1993).

[10] M. Willemin, C. Rossel, J. Brugger, M. H. Despont, H. Rothuizen, P. Vettiger, J. Hofer, and H. Keller, J. Appl. Phys. **83**, 1163 (1998).

[11] M. Willemin, A. Schilling, H. Keller, C. Rossel, J. Hofer, U. Welp, W. K. Kwok, R. J. Olsson, and G. W. Crabtree, Phys. Rev. Lett. **81**, 4236 (1998).

[12] M. Willemin, C. Rossel, J. Hofer, H. Keller, Z. F. Ren, and J. H. Wang, Phys. Rev. B **57**, 6137 (1998).

[13] J. Hofer, K. Conder, T. Sasagawa, G. meng Zhao, M. Willemin, H. Keller, and K. Kishio, Phys. Rev. Lett. **84**, 4192 (2000).

[14] S. Kohout, T. Schneider, J. Roos, H. Keller, T. Sasagawa, and H. Takagi, to be published.

[15] D. E. Farrell, W. K. Kwok, U. Welp, J. Fendrich, and G. W. Crabtree, Phys. Rev. B **51**, 9148 (1995).

[16] M. J. Naughton, J. P. Ulmet, A. Narjis, S. Askenazy, M. V. Chaparala, and A. P. Hope, Rev. Sci. Instr **68**, 4061 (1997).

[17] M. Willemin, C. Rossel, J. Hofer, H. Keller, A. Erb, and E. Walker, Phys. Rev. B **58**, R5940 (1998).

[18] S. Kohout, Ph.D. thesis, Universität Zürich (2005).

[19] F. Sass, C. Bouché, and A. Leitner, *Dubbel / Taschenbuch für den Maschinenbau* (Berlin: Springer, 1970), 13th ed.

Chapter 3

Automated measurement system

3.1 Torque measurement software

A large part of the improvement of the torque measurement system consisted of the development of a new control software. The formerly used Pascal program did not allow for automatic measurements and was becoming outdated concerning the current standard of graphical user interfaces. The use of the graphical LabVIEW$^{\mathrm{TM}}$[Lab] allowed an easy implementation of a new software system. After a short introduction to this graphical programming language and the involved technologies, the software system will be described in this section.

As a quick overview, Fig. 3.1 presents the whole software system consisting of several programs running in parallel. The main program which the user interacts with, is torque.vi. It is divided into two parts, the GUI and the command parser (CP). The former checks the graphical user interface for changes by the user and accordingly informs the CP which contains the actual logic for conducting measurements. The CP receives data and sends commands to the dataserver.vi, which in turn collects data from and dispatches commands to the handler.vis. These ultimately communicate with the physical instruments comprising the apparatus. The extension .vi is characteristic of LabVIEW programs. In the following sections the main features of LabVIEW and the communication paths used are explained. Finally, the whole software system is described in detail. More in-depth information not directly needed for understanding of the function may be found in appendix A. Several other helper programs were created to inspect and more efficiently organize measured data. They are described in section 3.3.

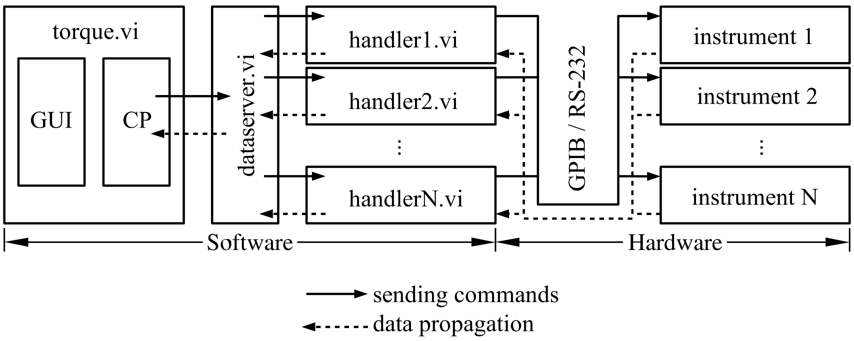

Figure 3.1: Main organization of the torque software system. torque.vi is the main program with which the user interacts. It is divided into two parts. One part (GUI) monitors the user interface for changes and informs the command parser (CP) accordingly. The CP contains the actual logic needed to conduct experiments. It sends commands to and receives data from the dataserver.vi which interacts with the handler.vis. These are able to communicate with the instruments attached to the computer.

3.1.1 Description of LabVIEW

The new system was developed using LabVIEW$^{\text{TM}}$, a programming language from National Instruments [Lab]. Instead of putting together a program by typing sequences of instructions the data-flow is diagrammed graphically, i.e. by drawing data connections (wires) between data sources, sinks and processors. Data sources and sinks are usually connected to parts on the graphical user interface like control knobs or graphs. Data processors can perform simple functions like arithmetic operations or more complex tasks like fitting functions or talking to externally connected instruments. This method of creating programs is very efficient because syntax errors are displayed immediately while drawing, which makes debugging very fast. Modular programming is strongly encouraged, because otherwise the programs tend to become increasingly cluttered. Moreover the creation of the graphical user interface is part of the programming itself, so it does not require basically any additional effort.

LabVIEW was developed mainly to facilitate interfacing of instruments to the computer. Therefore a program in LabView is called *Virtual Instrument* (VI). Any VI can be reused as a Sub-VI within another VI, similar to the usage of subroutines in conventional programming. Data can be passed to Sub-VIs and Sub-VIs can pass data back to the calling VI.

Supported data types are the same as found in most other programming languages and include numbers (floating point and integer types), character strings of variable length and boolean values. Multidimensional arrays can be built from all types. Moreover, there is the possibility to combine several different variables (numbers, strings, arrays, ...) into a so-called cluster, which can also be used to build an array. In this way, the limit to data complexity is set only by ones fantasy or by physical limits such as memory restriction or execution-speed considerations. Flow control mechanisms, as found in any other programming language, are present in LabVIEW as well. They include loop and for structures which are used to define a part of a program to be executed repeatedly and case structures which allow the selection of different parts of a program depending on the value of a specific data wire. This selector wire is not restricted to the boolean type for simple true/false decisions but can be a number or a string to select from dozens of alternatives.

3.1.2 GPIB bus overview

The data bus used to connect the instruments to the computer is the so-called General Purpose Interface Bus (GPIB), sometimes called IEEE-488 along with its specifications. Up to 15 instruments can be connected together. An interface card built into the computer assumes the task of a bus controller. It performs managing activities like addressing the attached instruments. Only addressed instruments are allowed to write to or read from the bus.

Apart from the connection lines used for transmitting data there are other bus control lines. They are not important for the understanding of the bus function, except for the service request (SRQ) line. Every instrument can send a signal over this line at any time, without being specially addressed. Usually an instrument does this whenever it wants to be serviced. Hence the name service request. After realizing that the SRQ line was asserted, the controller finds out which instrument requested service. There exists a function in LabVIEW to check a specific instrument has requested service. Most instruments can be set up to assert the SRQ line depending on different conditions. These include availability of a measurement, problems with the bus interface or overload situations where a measured quantity exceeds the measurement range. This functionality is used in the torque system software whenever possible. As an example, the temperature controller is checked often for the SRQ, but is talked to only if the asserted SRQ signals the availability of an updated temperature reading.

3.1.3 Sending commands via queues

VIs running in parallel cannot pass data among themselves as if they would call each other as sub-VIs. This and the following section describe the communication schemes used in the torque software system.

For sending commands between VIs, the so-called queue mechanism was used. This feature is native to LabView and consists of a collection of sub-VIs to create and manage FIFO-style (first in, first out) memory constructs. One process places values on top of this queue, whereas another takes the oldest value(s) from the bottom, thus forming a means of one-way communication. Another queue can be set up for the opposite direction. Each VI in the torque system has its own queue, identified by a unique name. In case any other VI needs to talk to this VI, sending a command to its queue is all that needs to be done.

Using queues it is ensured that

- no commands are lost, because items already residing in the queue are not overwritten. If needed, the queue's size is increased in order to hold all entries so that
- commands are executed in the correct order, because the oldest entry inside a queue is always returned first and so that
- each command is executed only once because it is removed from the queue after having been read.

Figure 3.2 schematically shows the communication paths for sending commands. If the user wants for example to change the cryostat temperature, he puts the number in the appropriate control on the torque.vi's graphical user interface. The GUI part detects this change and puts the corresponding command on CP's queue. The CP now sends the command back to GUI's queue as a confirmation and simultaneously sends it on to dataserver.vi to have it executed. The dataserver.vi receives the command in its queue and sends it on to the appropriate handler.vi VI, in this case handerLakeshore.vi, the one responsible for the temperature controller. handlerLakeshore.vi finally contains the logic necessary for changing the system temperature and executes the command.

3.1.4 Sending data using DataSockets

For returning measurement data from the instruments a so-called DataSocket connection is used. This is a memory construct, similar to queues, identified by a unique name, but with space for just one entry. Thus, each newly put

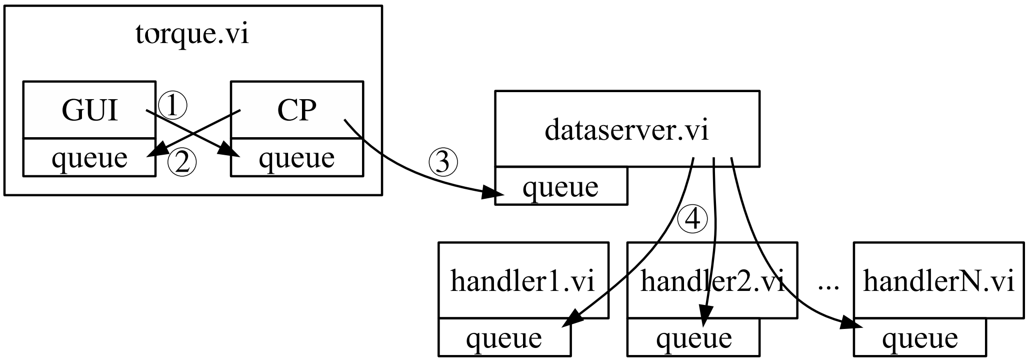

Figure 3.2: Schematic drawing depicting the communication paths used for sending commands by queues. Arrows indicate the command's propagation. At first, the GUI part of torque.vi detects a value change on a control on the user interface and sends an appropriate command to the CP (1). The CP sends the same command back as an acknowledgment (2). At the same time, CP sends the command to the dataserver.vi (3), which sends it on to the handler.vi appropriate for the specific command (4).

value overwrites the old one. This is reasonable with respect to measurement data. The system consuming data needs only the newest data.

The implementation within LabView differs in that there is an external program called the DataSocket Server which provides the service. It is intended to be used over the network to enable other computers to access the local data. Of course this also works if both the data producer and the data consumer are the same computer. LabView offers two sub-VIs which are used to write to and read from the DataSocket Server.

- More than one VI can read the same data.
- Obsolete data is overwritten.
- Old data is taken if no new is available.

Figure 3.3 schematically shows the flow of the measurement data. All handlers.vi independently write the measured values to their appropriate DataSocket locations as soon as they are available. The dataserver.vi waits for a new measurement to arrive at the lock-in amplifier's DataSocket and subsequently reads all other instrument's DataSockets. It then combines all this data into one measurement and writes it to the DataSocket called alldata. The CP part of torque.vi periodically reads the new data that arrives there. The measurement is thus registered and further processed.

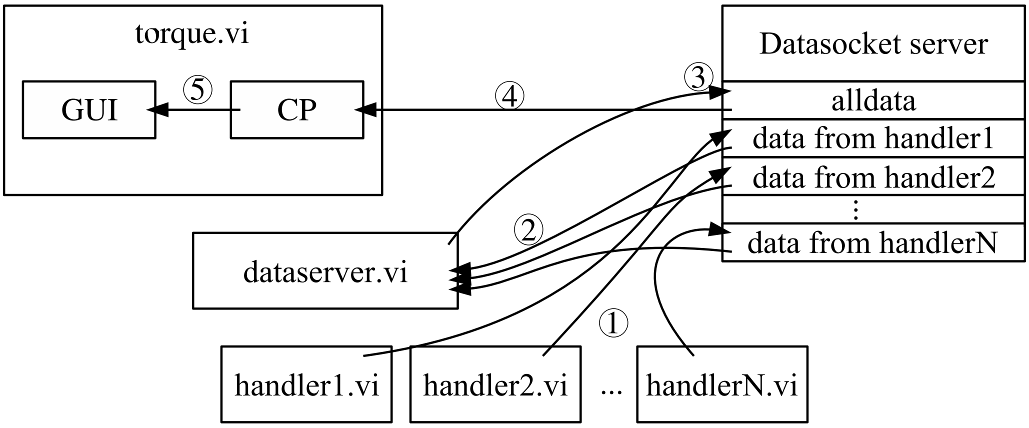

Figure 3.3: Schematic drawing showing the flow of the measurement data using the DataSocket server. Arrows indicate the data's movement. All handler.vis independently post their respective data to the DataSocket server (1). Whenever new data from the lock-in amplifier handler becomes available, the dataserver.vi is notified by the DataSocket server and downloads the data (2). It bundles all data and uploads it to a separate place on the DataSocket server (3). The torque.vi can then download the whole set of data at once (4). In the end, the data is sent to the user interface for display to the user (5).

3.1.5 Torque software overview

The whole torque software system consists of different VIs (shown in Fig. 3.1) running in parallel. Generally speaking, the physical setup of the torque apparatus was inherited. Thus, each instrument (temperature controller, magnet controller, lock-in amplifier, …) is managed by a separate VI, the so-called handler.vi. All handler.vis are initiated by one main VI, the dataserver.vi. Its purpose is to collect all data from the handler.vis and consolidate them before sending them to the main user interface, the torque.vi program. The torque.vi VI is the main point where the user interacts with the measurement system. Measurement parameters can be set and measurements started interactively.

torque.vi This is the main program with which the user interacts. It monitors the graphical user interface and issues the commands necessary to change measurement parameters. Moreover, all the functionality for measurement collection, graphing, saving and printing is contained within this VI. It talks to the dataserver.vi whenever an action is required on the instruments, like change of temperature or start of a parameter sweep. torque.vi is subdivided into two main parts which execute independently and in parallel as if they were separate VIs. One part, called GUI, repeatedly checks for changes of the controls on the graphical user interface. If such a change is detected, it sends an appropriate command to the second part, the so-called “command parser” (CP), which contains all the actual logic and functionality. This separation enables the CP part to be controlled not only by the user interface but also by other VIs. This makes possible the fully automatic control of the whole torque software system. One such program, the sequencer.vi was created which works through a previously created list of commands and sequentially sends them to the CP for programmatic control. It is described in detail in section 3.2. More complicated control programs can be thought of which change the sequence depending on the results of the recent measurements.

dataserver.vi This is the main background VI responsible for managing the information flow to the instruments. It redirects the commands from torque.vi to the appropriate instrument handler VIs. Moreover, it collects the data from the instruments and sends them to torque.vi according to what was requested. It knows which handler.vi publishes which data. This VI displays some basic status information about each running handler.vi VI and can be used to send commands to the instruments directly. However, it lacks the functionality to collect whole measurement sets.

handler*.vi** These VIs actually “do the work” in the whole system. They know how to talk to the devices attached to the GPIB bus or the serial interface and perform more complex tasks like rotating the magnet or sweeping the temperature.

Although this architecture seems somewhat complicated it is in effect easier to maintain than one large VI which performs everything by itself. Moreover, having the VIs which communicate with the instruments run in parallel makes more efficient use of the GPIB bus and therefore results in a higher data acquisition rate. In fact, adding new functionality is easier than one might think. In most cases, only one of the handler.vis and the main torque.vi need to be changed while all other lower level VIs remain unaffected. In case a new device like a voltmeter is added to the measurement setup, a new handler.vi is created quickly by copying an existing similar one and changing the part which is specific to the instrument. After including the new handler.vi in the dataserver.vi and adapting torque.vi to understand the new data, all is done already. The similar internal organization of the VIs makes it even simpler to make such extensions. Everything is based on the exchange and interpretation of commands. The logic of the VIs can therefore be understood

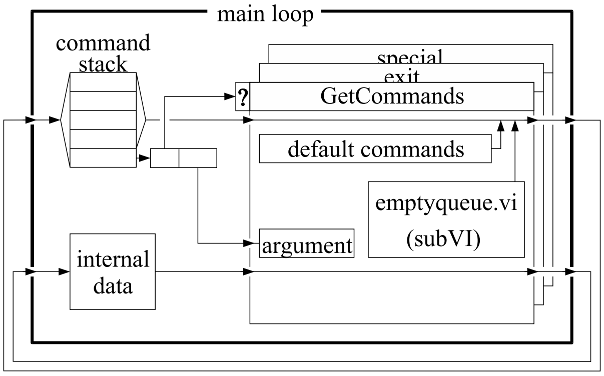

Figure 3.4: Basic *command parser* structure of all VIs. A main loop encloses the relevant parts, which are the command stack holding a set of commands which are to be executed, some internal data and a case structure consisting of several cases (GetCommands, exit and special are shown here). Upon each iteration of the main loop, the latest command is retrieved from the command stack and split into instruction and argument. The former is fed into the selector of the case structure and chooses the appropriate case. The latter is passed into the case and is used by it accordingly. Each case may alter the contents of the internal data and the command stack. In the example shown, the subVI emptyqueue.vi is used to obtain new commands from the queue, which are then appended to the command stack.

in terms of a *command parser* (CP). They are able to receive commands with arguments and act accordingly. Not only do they react to commands received by other VIs, but also their continuous operation is accomplished by repetitive execution of a basic set of commands, which are stored in a list internally.

3.1.6 General VI detailed structure

As was explained in the previous chapters all actions within the torque software system are organized via commands. So each VI needs to interpret and act accordingly on such specially formatted strings. Basically, the structure of the VIs is that of a *command parser* (see Fig. 3.4).

The main building block used to accomplish this, is a case structure inside a loop structure. The loop structure ensures continuous execution of the enclosed elements. It is only stopped, if an exit command occurs. Each case within the case structure is identified by a character string, which in turn is its corresponding command. Thus, each command is interpreted by a special case. Upon each iteration, a command is removed from the internal command stack and executed. There exists a case, which fills the stack with a sequence of commands as soon as it is empty. This sequence consists of the commands received via the queue from other VIs and of commands necessary for the VI's continuous function. Some commands even put commands on the stack themselves in order to work correctly.

Summarizing, each VI consists of a

- loop structure, executed indefinitely (until an exit command is received), containing a
- case structure which handles the different commands, a
- stack holding commands both scheduled internally or received from external sources and
- data needed for the execution.

All of this together functions as a command parser (CP). Different commands perform different tasks and either change the internally stored data, perform operations on the instruments or both.

3.1.7 torque.vi detailed structure

As mentioned above, the torque.vi is the main program. It is divided into two parts, the graphical user interface handler (GUI) and the actual command parser (CP). The whole program logic is contained in the CP part, whereas the GUI simply checks the user interface for changes and reports them to the CP.

The program knows two distinct running conditions, *interactive* and *scanning*. When in the former state, the user can change the state of the experiment, define parameters for measurement scans and investigate, view, save and print measured data. In the latter state, an automatic scan of torque versus a specified measurement parameter is carried out. The upper and lower bounds of the scan, the scan direction, the speed and the step size are set beforehand in the interactive mode. During a running scan, other interactive operations remain possible. It is the responsibility of the operator not to disturb a running measurement.

In order to simplify the frequent use of different measurement settings, it is possible to define several so-called presets. Each preset is identified by a unique name and holds a set of scan settings, consisting of the parameter to be scanned (temperature, field or angle), its range and the speed, step size and measurement mode to be employed. New presets can be defined based on existing ones. They can be renamed and deleted. The most basic and useful presets are built into the program and do not have to be specially defined.

The process of performing scans is quite sophisticated and will now be summarized. Each scan is defined by the above mentioned corner values (minimum, maximum, speed, step size, direction) and a so-called trigger program. This program is used to determine when a measurement should be considered as valid, which part of the measurement should be saved and to define whether the shaking coil should be turned on or off. The commands understood in such a trigger program are the following:

wait waits for a specific amount of time or for the parameter to become stable.

mark marks the current position within the pretrigger

include [N|mark] includes the last N seconds or all points after the mark.

save [keyword] Saves the current measurement. The keyword must be a valid postprocess command like nearest or average. The former just saves the measurement which is closest to the current setpoint while the latter saves the average of all of the current measurement.

shake [N] turns shaking on ($N > 0$) or off ($N = 0$).

Measured data is held at four different storage spaces within the program, described in the following list.

pretrigger contains the set of most recent measurements received from the dataserver.vi, usually the last few seconds.

log: In regular intervals a measurement is copied on the end of this structure. It helps to track the status of the measurement system concerning temperature and measurement stability.

scan measurement contains the raw data of a scan measurement

postprocessed data is filled with a copy of the scan measurement data after processing.

A unified mechanism is used for transferring data between these storage spaces. For appending newly measured data points to the scan measurement or the log structure or for reorganizing measured data from the scan measurement to the postprocessed data structure, the same *postprocess* mechanism is used. It is a command within the CP, which accepts an argument specifying the precise task to be performed. One very convenient command is the combine command used to reorganize data such that values measured during increasing and decreasing scan parameter appear in adjacent columns when saved, rather than in one single column below each other.

3.1.8 dataserver.vi detailed structure

The dataserver.vi collects the data published by the handler.vis to the DataSocket, puts them together and publishes it back to the DataSocket to form the actual measurement. The dataserver.vi can be instructed which data to combine to the measurement while it is already running. It knows which handler.vi provides which data and appropriately forms the requested combination. Moreover, this VI serves as a basic control tool for the GPIB interface's functioning. It displays all the instruments' current status which is updated on a regular basis, about once every second. It offers a large display of the current Lock-In Amplifier reading and a liquid helium level indicator. The helium level is not measured, but calculated from an initial value and the subsequent consumption. Therefore, as time goes on, the indicated value becomes more inaccurate and can be used as a rough estimate only.

Because the operation of dataserver.vi is much simpler and more regular compared to the other VIs, there is no command stack built into it. Nevertheless the function is based on commands. Each command simply defines which command to execute afterward. The exit condition is checked only at one point, in which case execution stops. Otherwise the program is kept in an infinite loop. It is also not possible to interactively change the sequence or execute special commands.

3.1.9 handler.vi detailed structure

As stated above, the general structure of all VIs in the system is similar. The handler.vis are even identical concerning their architecture. They differ in the cases contained in the main case structure, because they comprise slightly different functionality and because the instruments they are programs for need different treatment. A handler.vi for a newly attached instrument is easily created by copying an existing handler.vi and modifying it to the specific needs.

handlerEGG7265.vi

The EG&G model 7265 is the lock-in amplifier used in the torque system. It features an internal oscillator which can be used to excite the sensor. It also has additional analog in- and outputs and eight digital output lines. These are used to monitor and control the coolant flow in the cryostat as well as the motion of the small motor. The whole device can be fully controlled via a built in GPIB interface. Not all of the ampifier's functionality is needed for torque measurements, so only a part of the available commands was incorporated into the handler.vi.

handlerLakeshore.vi

The Lakeshore model DRC-93CA is the temperature controller for the cryostat. It is able to read two temperature sensors with user definable calibration curves and drive a heater, controlled with a freely configurable three term (PID) real-time analog control. This temperature controller is able to indicate via the SRQ mechanism which temperature sensor has been updated. This makes efficient use of the GPIB bus possible.

handlerBruker.vi

The Bruker B-H 15 field controller's GPIB interface is old and little error tolerant. There were some timing problems and very often the field controller is the only device needing a reset after some unexpected happening. The field controller offers different modes of operation. We are using mode 5 where the field can be swept using an internal sweep address generator. The instrument can be provided with a center field, sweep width and sweep time value and then be left alone to do the sweeps. By the use of special commands the sweeps can be started and stopped. Due to the internal structure of the field controller, it is not possible to directly read the field. The number received from the controller when reading the field represents the current field's position in the current sweep, i.e. between the programmed lower and upper limit. The handler.vi remembers these settings and calculates the field from the value returned by the controller.

handlerAngle.vi

The device used to read out the magnet's angular position is connected to the computer via a serial connection (instead of using the GPIB bus). This makes the implementation of the communication somewhat different, but the handler.vi's general structure stays the same. The magnet's angular position is read regularly. If the magnet has to be moved, the necessary speed is calculated and the appropriate command (motor=N) sent to handlerEGG7265.vi in order to set the motor speed. When the position is approaching toward the final position, the speed is automatically reduced in order to make an accurate stop possible. For this purpose, a list is maintained which defines the maximum speed for a given distance from the setpoint. Thus, whenever the distance falls below a value from the list, the speed is reduced accordingly.

3.2 Automation

The seemingly needless splitting of the main program (torque.vi) into two parts GUI and CP becomes obvious when trying to introduce automation into the system. As mentioned in section 3.1.7 the GUI simply sends commands to the CP to instruct it about the users intents. Because the input by queues is open to the outside (the same mechanism is used to send data between VIs running in parallel), it is possible for any other VI to send the same commands to the CP. Such a VI is the sequencer.vi. It can be used to automatically control the whole torque software system. A specialized sequencing language is used to create so-called sequence files. These are ordinary text files consisting of a set of instructions. These can be a simple list of commands or a complex program involving iterations and branchings. The sequencing language will be described first. Details on the sequencer.vi follow afterward.

3.2.1 Sequencing language

Basically, a sequence is just a text file. Known commands are recognized simply by their appearance as keywords. Everything else is treated as an argument to the last recognized command. Thus, it is possible to provide a command with several arguments. However, care has to be taken not to include any keywords into arguments. This would cause the start of a new command. Such arguments can be protected by enclosing them in quotes ("). Keywords are delimited by whitespace characters (line brakes and space characters). The available commands include the obvious ones like setting the system temperature or starting a scan measurement. Additionally, some wait commands are needed. It is clear that the system temperature should not be changed while a field dependent measurement is running. When working interactively, this is intuitively done by the user, but if a sequence is to be run, such waiting must be performed by the system. A list of available commands is given below.

Torque commands

Words written in typewriter font (`example`) must be put in the sequence exactly as given there. Italicized characters (X) represent variables which have to be replaced by the desired value. The allowed values depend on the command and are given in the list as well. To show allowed alternatives, the notation [`one`|`two`] is used (in this case, either `one` or `two` would be allowed).

`setfield` N Set the field to N Oersted. This deprecated unit for magnetic field is still used here, because the Bruker BH-15 field controller uses the cgs system.

`setangle` N Set the magnet angle to N degrees.

`settemp` N Set the temperature to N Kelvin.

`sweeptemp` S>N Continuously sweep the temperature at S Kelvin/minute until N Kelvin is reached. S need not have the correct sign.

`shaking` N Change the frequency of the Wavetek waveform generator (connected to the shaking coil). N is a multiplier applied to the frequency set on the front panel of the Wavetek (N=0:off).

`setrange` N Sets the sensitivity range of the LIA to N Volts (N can contain units such as `10mV` or `100uV`).

`settimeconst` N Sets the averaging time constant of the lock-in amplifier to N seconds (N can contain units such as `ms`).

`setphase` N Sets the phase angle of the lock-in amplifier to N degrees (for details, refer to the lock-in amplifier manual).

`setflow` N Sets the coolant flow in the cryostat to N=0...200 display units.

`comment` S Sets the comment to S (any string). If S contains spaces, it must be enclosed in quotes ("). The comment will be saved along with the data at all subsequent `save` commands.

`postprocess` S Causes the postprocess command S to be executed.

`save`|`print`|`clearplot` *plot* saves, prints or clears the plot indicated by *plot*. Allowed values are the following: `pretrigger` = `trigger` = `measurement` = `0` all represent the same, `log` = `time` = `"all vs time"` = `1` again are the same, `"scan"` = `2` are for the scan measurement and `"postprocessed data"` = `data` = `processed` = `3` are the same again. Note the usage of quotes.

`filename` *S* Sets the filename to *S* which must be a complete filename with drive, path and filename.

`tempcontrol` [`off`|`cooler`|`heater`|`hold`] Sets the temperature control mode. If `cooler` is chosen, temperature is controlled by software via adjustment of the coolant flow. In the case of `heater`, the Lakeshore temperature controller stabilizes temperature by means of the cryostat heater (the coolant flow must be set manually with `setflow` in this case). When `hold` is chosen, the coolant flow is regulated during five minutes and is afterward set at the recorded averaged value.

`heaterrange` [`off`|`-4...-1`|`max`] Sets the power range for the Lakeshore Temperature Controller heater.

`setscan option=value` Sets measurement scan options and controls the usage of presets. Valid options and values are the following:
`NewPreset=`*S* defines a new preset based on the current one with a new name supplied by *S*.
`DelPreset=`*S* deletes the preset indicated by *S*. If *S*is a string, it must match an existing preset's name. If *S* is a number, it is understood as the position where it appears in the preset selection box in torque.vi.
`Preset=`*S* selects the preset indicated by *S*, understood in the same way as in `DelPreset`.
`scan=`[`H`|`f`|`T`|`0`|`1`|`2`] changes the scan parameter to the indicated one for the current preset.
[`min`|`max`|`delta`|`speed`]`=`*N* alters the current preset's indicated key parameter to *N*.
`direction=`[`up`|`up&down`|`down`|`down&up`|`0`|`1`|`2`|`3`] selects the current preset's scan direction.
`mode=`[`stepped`|`smooth`|`0`|`1`] sets the current preset's scan mode.
`nmbr=`*N* defines the current measurement to be number *N*. This parameter is used only for some `postprocess` commands. Most frequently and to avoid confusion, it is left at 1.
`stacklength=`*N* defines the length of the `pretrigger` in seconds. Usually this is set at 5 seconds.
`program=`*string* defines the trigger program for the current `preset`. Remember that, because most likely the program will contain whitespace characters, the string must be enclosed in quotes (").

`beep` simply causes the computer to produce sound. This can be used to attract the user's attention if his intervention is needed.

`scan` [*string*] Starts a scan. If specified, *string* must be a valid preset name

`wait`N[s|sec|min|h|hour|hours] Causes the execution to wait for the specified time. Any such wait can be interrupted by the continue button on the sequencer.vi, causing execution to continue.

`waitangle|waitfield|waittemp drift`(op)N `delta`(op)N Causes the sequence to halt until the specified condition is satisfied. The default depends on the actual measurement parameter, so just writing `waitangle`, `waitfield` or `waittemp` usually produces reasonable effects.

Being able to create a list of commands which is worked through sequentially is a big improvement over the interactive use, where each step is initiated via the graphical user interface. However, as soon as extensive measurements are needed, such sequences become extremely long and therefore hard to maintain. Therefore, flow control commands and variables were included into the sequencing language. These will be described now.

Variables

Variable names in sequence files can contain characters and numbers. They are case insensitive (`T` and `t` is the same variable). Variable values can be characters, strings and numbers. No strict separation between these types is maintained. If an arithmetic operation is possible on two variables, it will be performed; otherwise the values are simply concatenated to form the result.

The general assignment command is `set`.

`set t=10` creates a new variable and assigns it the value 10

`set p=20.5` creates a new variable and assigns it the value 20.5

`set t=t+p` replaces the value of `t` by the sum 30.5

`set p="temp="` replaces the value of `p` by the given string.

`set t=p+t` Now `t` will be `temp=30.5`

Most mathematical expressions can be used on the assignment's right-hand side. For details refer to the documentation of LabView's Eval Multi-Variable Scalar.vi function. Any variables used in a command are replaced by their value prior to execution. Thus, it is possible to use `settemp t` to set the system temperature to the current value of `t`.

The `if` structure

`if` can be used to choose between execution of different parts of the sequence. A mathematical comparison can be used as a condition.

```
if t>30 then set t=t+2 else set t=t+1 endif
```

This example increments the variable `t` by two if it is already larger than 30, otherwise it is incremented by only one. Note that `t` needs to be defined before this line appears in the sequence. Any number of commands and structures can be included between the `then` and `else` or between the `else` and `endif` keywords. The `else` keyword is optional, but every `if` needs a matching `endif`.

The `while` structure

This structure can be used to execute a part of the sequence repeatedly, depending on a condition.

```
while t<30 set t=t+2 endwhile
```

In this example `t` is increased as long as it is smaller than 30. Again `t` needs to be defined before this line in the sequence. Every `while` has to be matched by an `endwhile` keyword.

The `repeat` structure

This is very similar to the `while` structure with the difference that the condition is checked at the end. Thus, the part inside will be executed at least once.

```
repeat set t=t+2 repeatwhile t>30
```

As `if` and `while`, the `repeat` keyword has to be closed by a `repeatwhile` keyword.

The `for` structure

`for` is often much more convenient than the aforementioned two structures. Its function is most easily explained with an example.

```
for t=11,12,13,14,15,20,25,30,35,40 settemp t endfor
```

The inner part (`settemp t`) is executed once for each value in the list. After each iteration the next value in the list is taken from the list. The continuation operator (`...`) can be used to shorten the above command.

```
for t=11,12,...,15,20,..,40 settemp t endfor
```

Two or three dots (`..` or `...`) indicate a continuation of the last interval until the next value is reached. Because the step between the last two numbers before the first `...` is `11-10=1`, `t` assumes the values `13` and `14` before going to `15`. After `20` is executed, `t` becomes `25`, `30` and `35` before reaching the final value `40`. The two versions `..` and `...` are identical. The number of points interpolated depends solely on the number after the dots. Note the placement of commas. They are needed before and after the `...`. It is possible to assign not only numbers, but also strings.

```
for s=first,second,third setcomment s endfor
```

sets the comment to `first`, `second` and `third`. Simultaneous assignment of more than one variable is also possible.

```
for s,d,c=(10,5,fast),(1,1,slow)
setscan speed=s delta=d
setcomment c endfor
```

In the first iteration, the scan speed and step size are set to 10 and 5, respectively, while the comment is set to `fast`. In the second iteration, the second set of parameters is set. In the case of simultaneous assignments the parentheses are compulsory. The combination of continuation (...) and simultaneous assignment is also possible. Values that cannot be incremented are simply repeated. Great care has to be taken that at least one parameter reaches the upper limit. The following would run forever.

```
for s,c=(1,first),(1,second),...,(2,third) endfor
```

The first parameter `s` remains 1 and never reaches the next value (2). The second parameter `c` cannot be incremented and therefore remains `second`.

```
for s,c=(1,first),(2,second),...,(10,tenth) endfor
```

is correct. While `s` cycles from 3 to 9, `c` remains set to `second`.

3.3 Helper applications

Additionally to the torque measurement system there are some VIs that are useful for the inspection and organization of the data.

3.3.1 dataviewer.vi

This VI can be used to inspect already measured data files. Some fitting functions are available as well. The performance is not suitable for serious data analysis, but suffices for quick on-line checks of the data. Fitting should not be performed while taking measurements, because the process usually consumes considerable computing power. This results in execution pauses of the other programs (torque.vi and dataserver.vi) and consequent loss of data points.

3.3.2 selector.vi

Several measurements can be displayed simultaneously for better comparison and grouped together in selections. These selections are saved to a text file in the same directory where the measurements reside, so that they can be efficiently processed later.

3.4 Related publication

Automated operation of a homemade torque magnetometer using LabVIEW
Stefan Kohout, Joseph Roos and Hugo Keller
Meas. Sci. Technol. **16** (2005) 2240–2246

INSTITUTE OF PHYSICS PUBLISHING MEASUREMENT SCIENCE AND TECHNOLOGY

Meas. Sci. Technol. **16** (2005) 2240–2246 doi:10.1088/0957-0233/16/11/015

Automated operation of a homemade torque magnetometer using LabVIEW

S Kohout, J Roos and H Keller

Physik-Institut, Universität Zürich, Winterthurerstrasse 190, 8057 Zürich, Switzerland

E-mail: kohout@physik.unizh.ch

Received 8 April 2005, in final form 17 August 2005
Published 28 September 2005
Online at stacks.iop.org/MST/16/2240

Abstract

In order to simplify and optimize the operation of our homemade torque magnetometer, we created a new software system. The architecture is based on parallel, independently running instrument handlers communicating with a main control program. All programs are designed as command driven state machines which greatly simplifies their maintenance and expansion. Moreover, as the main program may receive commands not only from the user interface, but also from other parallel running programs, an easy way of automation is achieved. A program working through a text file containing a sequence of commands and sending them to the main program suffices to automatically have the system conduct a complex set of measurements. In this paper, we describe the system's architecture and its implementation in LabVIEW.

Keywords: magnetic torque, LabVIEW, automation, software, condensed matter research, superconductivity

1. Introduction

In modern condensed matter research, most interesting subjects are only subtle effects which can be investigated only by thorough and systematic studies of large numbers of samples. Even though first investigations have to be done by hand, a lot of time can be saved with automated measurement set-ups. Such automated systems are already widely used in large scale experiments, but most small laboratory experiments, even though computer controlled, do not allow for automated measurements. Frequently there are possibilities to have the system execute individual measurements automatically, but covering large areas of parameter space is seldom possible. Laboratory apparatus usually consists of several interconnected instruments with complicated interplay between them. Commercial control software is available for the individual components only. Consequently most control software is written by the scientists themselves, who face the lack of time, money and manpower to develop extensive automation software.

In this paper, we present an easy way of creating control software which offers possibilities of programming complex sequences and automatically executes them[1]. This is shown to be achieved with moderate development effort using a common laboratory programming language. We will first present the different architecture approach needed to achieve this goal, after which the addition of automation is a small step.

2. Software for laboratory equipment

Programs created for the control of experiments need to perform several tasks. Firstly, they have to be able to send control commands to the instruments and receive the measured data. Secondly, these data are to be processed and displayed and eventually user input needs to be translated to control commands. Various development platforms offer vast libraries of procedures to interface instruments, create user interfaces and perform complicated data processing. These help reduce the workload associated with creating such software. LabVIEW™ [1], a development environment from National Instruments™ for creating programs (called virtual instruments or, in short, VIs) in its own graphical programming language 'G', is probably best known and most widely used for such applications. 'G' offers all the flow control structures like loops and conditional branches found in any other programming language. Moreover, any VI can easily be used in any other VI as a subVI. LabVIEW VIs consist of a user

---

[1] Source code examples available on request.

0957-0233/05/112240+07$30.00 © 2005 IOP Publishing Ltd Printed in the UK

interface (UI) and a block diagram (BD) containing the actual code. Programming is done by modelling data flow, where graphical representations of functions and procedures are interconnected by lines, usually called wires. This somewhat unusual approach may cause unease at first, but the on-line help system and numerous code examples allow a steep learning curve. The designation VI stems from the similarity of such a program to an actual instrument, the UI obviously corresponding to the instrument's front panel and the BD to its internal wiring.

The usual way of creating LabVIEW software for measurement control is by writing a main VI containing the UI and the logic for acting appropriately on the user input as well as processing, displaying and saving the data. Communication with the instruments is performed by driver subVIs which are regularly executed by the main VI. When such a driver VI is called to perform a query on an instrument it sends the necessary command to the instrument, waits some time for the instrument to prepare the answer and finally reads this response from the instrument. Usually this process takes tens to hundreds of milliseconds. Assuming the whole measurement set-up consists of several instruments, the main VI may be organized in two different ways. Either all driver VIs are called sequentially, causing the time needed to collect all data to grow with the number of instruments. Another approach would be to call the driver VIs in parallel, which is possible thanks to the inherently multi-threading architecture of LabVIEW. In this case, however, all drivers would attempt to access the instruments at the same time. This would result in a 'traffic jam' in the case that the instruments are connected to a single interface bus. Some drivers would be forced to wait until the others have finished their writing to the bus. Moreover, as some instruments take measurements less often than others, many operations on the bus would be unnecessary because no new data would be obtained.

In this paper, we present the use of independent driver VIs, which we call handlers, running in parallel and communicating with a main VI by means offered by LabVIEW. This allows a more efficient use of the interface bus employed to connect the instruments and results in a higher data acquisition rate. Moreover, by employing a 'state machine' (SM) architecture such programs become easier to extend in functionality, to maintain and most importantly allow for the control by a separate program and consequently automation.

3. Experimental set-up

The programs presented here were developed to control and automatize a torque magnetometry apparatus which was built in our group [2, 3]. Such a device is used to measure a sample's magnetic moment **m** by the torque

$$\boldsymbol{\tau} = \mu_0 \mathbf{m} \times \mathbf{H} \qquad (1)$$

it experiences due to a magnetic field **H**. It is well suited for the investigation of anisotropic magnetic phenomena as found in most high temperature superconductors. Torque magnetometry is complementary to most other magnetometry techniques in that it is only sensitive to the part $m_\perp$ of **m** perpendicular to the applied field. A torque measurement is fast—one measurement taking a fraction of a second only—and due to the proportionality $\tau \propto H$ reaches high sensitivities for $m_\perp$ in high fields. Our homemade torque magnetometer system, shown schematically in figure 1, consists of a flow cryostat between the poles of an iron yoke magnet which sits on a rotatable support. Usually, two piezoresistive torque sensors are used simultaneously. The sample is mounted on one of them, whereas the other serves as a reference, as is shown in figure 2. Two piezoresistive paths are

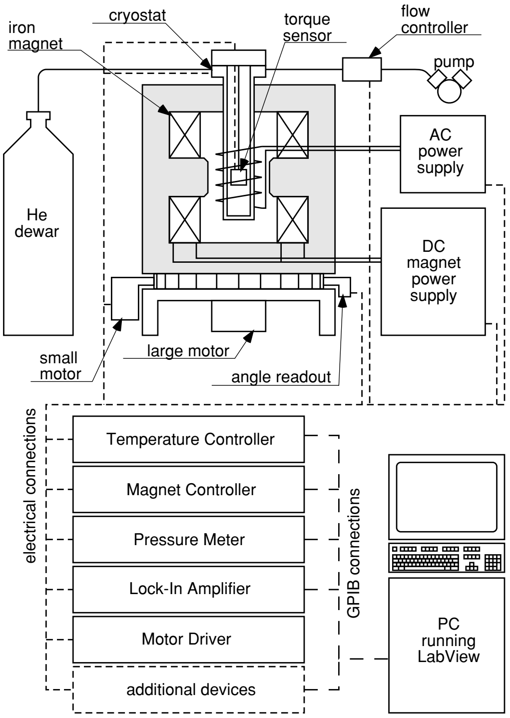

Figure 1. Torque measurement set-up overview, which was automated using the presented software. A cryostat is placed between the poles of an iron yoke magnet, which is freely rotatable. The torque sensor is inserted into the cryostat and connected to readout electronics. All instruments needed to control the experiment's state are connected to a personal computer.

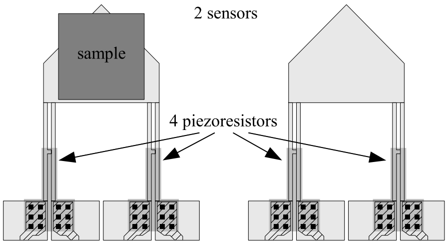

Figure 2. Illustration of the torque sensor set-up. The piezoresistive paths of two identical sensors are connected to form a Wheatstone bridge. One sensor holds the sample whereas the other serves as a reference.

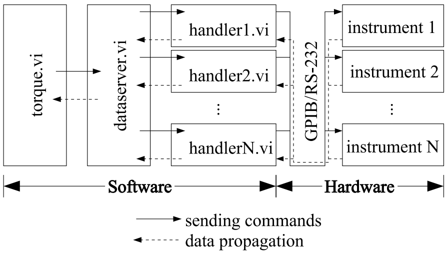

Figure 3. Architecture of the torque control software system. All VIs (torque.vi, dataserver.vi and the handler*.vis) execute in parallel. Commands are sent along the solid right pointing arrows and data propagate back along the dashed left pointing arrows.

fabricated on each sensor which are used to measure the stress on the sensor surface caused by the torque applied by the sample. All four piezoresistive paths are connected to form a Wheatstone bridge for highly sensitive detection of the resistance changes. A commercial lock-in amplifier (LIA) with integrated programmable oscillator is used to both excite and measure the bridge. Details of the measurement principle are beyond the scope of this paper and are described elsewhere [2, 3]. All devices needed to control and measure the system's state are connected to a Windows PC via an IEEE-488 General Purpose Interface Bus (GPIB), RS-232 serial connections and indirectly via additional analogue and digital input and output ports present in the LIA instrument. The main parts are a simple PCI-GPIB adapter card from NI built into the computer, the EG&G Model 7265 LIA, a Lakeshore DRC 93A temperature controller and the Bruker BH-15 magnetic field controller. Additional devices such as a pressure transducer with read out electronics for monitoring the exchange gas pressure in the cryostat or current sources and voltmeters for specialized applications may also be connected via the GPIB. The GPIB is an interface bus which is widely used in scientific instruments. It features 8-bit parallel data transfer, handshaking and real-time response capabilities. The software accessing the instruments was written based on the respective hardware users' manuals without need for commercial driver software.

4. Software system architecture

The architecture of the newly developed control software is shown in figure 3. Each instrument connected to the system is represented by a VI counterpart called *handler.vi*. All handlers are managed by the *dataserver.vi* VI which communicates with the *torque.vi* VI, which is the main application. All these VIs run independently in parallel. This way each *handler.vi* can be optimized to take best advantage of the instrument it is built for. This includes the waiting times needed for communication, an optimized data rate based on varying needs as well as the use of each instrument's ability to signal special events via the GPIB. Since all *handler.vis* run in parallel, their individual write–wait–read cycles needed to talk to the instruments are interlaced, thus reducing the bus' idle time. Moreover, each instrument is talked to only when necessary thus reducing the bus occupation while retaining data quality. This can be optimized particularly well by exploiting the service request (SRQ) functionality of the GPIB. Many instruments can signal a number of events to the GPIB controller by asserting the special SRQ line. Such events might be error conditions but can also be indicators of data availability. As an example, the Lakeshore temperature controller is programmed to assert the SRQ line whenever a new temperature reading is ready. As this occurs only every 2 s, the instrument is read only when really necessary instead of reading the same data several times per second. Even instruments not offering such functionality can be optimized by reducing the rate at which the *handler.vi* is instructed to read the instrument. This enables the more crucial measurements to be read more often resulting in data taken at a higher rate and resulting in better quality.

Because the *handler.vis* are not called as subVIs by the main VI, a special means of communication needs to be established. Here we use *queues* for sending commands to the *handler.vis* and *DataSockets* for receiving the measured data. A *queue* is a first-in–first-out style memory construct which is offered by LabVIEW. It may contain a fixed or unlimited number of string entries, in our case commands. By use of special subVIs any VI can append commands to a *queue's* end or retrieve the oldest commands. Any read entry is automatically removed. *Queues* are identified by a name, making access to them fairly easy. In most applications a given *queue* is read by only one VI whereas several VIs may write to it. *DataSockets* are memory constructs as well, identified by a unique name, but only contain the most recent datum. Their data type can be freely chosen among the data types in LabVIEW. The *DataSockets* used in our case are arrays of floating point numbers containing a *handler.vi's* main data. The *dataserver.vi* mentioned above serves as an intermediate VI which collects all the *handler.vi's* data and puts all together in a separate *DataSocket* which is then read by the *torque.vi* main VI. Thus, the main VI needs no knowledge about which data to obtain from which instrument. Even though LabVIEW offers to buffer more than one datum in a *DataSocket*, we configure our *DataSockets* such that each new piece of data overwrites the previous one. This ensures that no pile-up of data occurs (eventually causing a program crash) in case of unexpected delays due to malfunction in parts of the hardware system. Thus, we sacrifice data completeness for long-term stability and error tolerance. In fact, measurements are missed too rarely during normal operation to cause concern.

In order for the VIs to be able to act accordingly on the possible commands, they must be given some command parsing functionality. In fact such a command parser is every VI's core part: even the regular operations performed by the VIs are put into commands which are executed repeatedly. Essentially, all VIs are designed as command driven SM. The use of the SM paradigm in LabVIEW programs has already been proposed on several occasions [4–7] and given LabVIEW's capabilities this is not surprising. Nevertheless, to our knowledge only a few instrument control applications make use of this architecture. The basic idea is that by being executed, a program goes through various named states. The order in which these states are visited may be fixed and defined in advance or the state to follow might be determined based on the current state's result. The implementation in LabVIEW

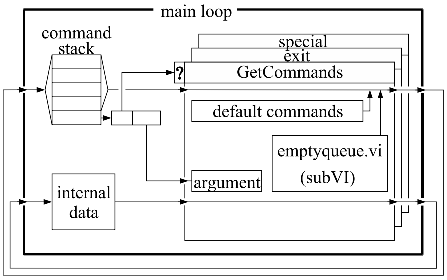

Figure 4. Schematic illustration of the VI's basic structure. An all enclosing main loop executes infinitely. The logic inside consists of a command stack whose first element is divided into instruction and argument. The instruction is used as the selector value into a case structure containing the code for the individual instructions. This results in the command parsing functionality needed for the operation. Internal data needed for the VI's execution are passed through each iteration and can be read and modified by each command case.

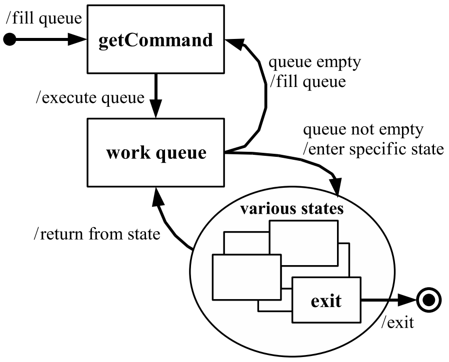

Figure 5. Generic state transition diagram, approximately common to all VIs. Basically, the following state is not defined by specific conditions in the current state, but the execution order is fixed after the *GetCommand* state is left. Additionally, certain states may insert additional states into the execution queue.

is fairly simple and is shown schematically in figure 4. An infinitely running loop contains a case structure consisting of all the states. These states are identified by character strings and are therefore easily human readable. In contrast to other methods, where the identification is by numbers or special enumeration data types, this makes the structure easy to extend and maintain. In addition to these structures the VIs contain a command stack and some internal data needed for execution. Upon startup, when the command stack is empty, a default case (state) is executed. Usually this is the 'GetCommands' case. This case contains the code needed to empty this VI's *queue* and a set of default commands which are put onto the command stack. When the main loop is iterated for the second time, the oldest command is removed from the stack, split into an instruction and optional arguments, whereupon this instruction is fed into the case structure selector, defining the case to be executed. This case may add more commands to the stack or simply perform a specific task. When the case is finished, the main loop iterates again, the next command is removed from the stack and so on. Whenever the stack becomes empty, the default case 'GetCommands' is executed again and refills it. Figure 5 shows a generic state transition diagram, which is approximately common to all *handler.vis*. The *handler.vis* run independently of the other programs, so no deadlock condition can occur, where two processes are waiting for each other. The only states waiting for a specific action are the *readdata* states in the *dataserver.vi* and the main *torque.vi*. Both are secured by reasonable timeout values. The execution speed is governed by the *handlerLIA.vi* for the LIA. The *dataserver.vi* waits for data from this handler, whereas *torque.vi* waits for the full dataset including the measurements from the other *handler.vis* from *dataserver.vi*. At the data rate of 10 Hz of the LIA, there is plenty of CPU time available for all other processes.

Because the *handler.vis* are independent programs not having to rely on being called regularly by a master VI, they can be used to carry out more complex tasks than just talking to the instruments. As an example, *handlerLakeshore.vi*, the *handler.vi* for the Lakeshore temperature controller, contains logic to control the temperature by software through control of the coolant flow in the cryostat. The flow controller is connected to a separate digital-to-analogue converter (DAC), thus enabling the *handlerLakeshore.vi* to control it by sending commands to the DAC's *handler.vi* (*handlerDAC.vi*). Keeping track of the last few seconds of measured data, calculating their time trends and publishing it to the *DataSocket* is coded into a command and performed by the *handler.vis* as well. All of this activity is hidden to the user. He only interacts with the UI of the main *torque.vi*, which is shown in figure 6. It gives the user the possibility of controlling all aspects of the experiment by entering appropriate values into the control fields. The measured data are visualized live in an *X*–*Y* graph.

5. Automation

As mentioned earlier, all VIs are organized as state machines, even the main VI *torque.vi*. As shown in figure 7 every user action (button press, value change) on its UI is transformed into a command by the UI-handler which is then sent to and processed in the SM. The SM then sends appropriate commands to the *dataserver.vi* and the *handler.vis* (wide arrow ① in figure 7). These two parts (UI-handler and SM) are independently running components of *torque.vi*. The communication between them is again ensured via *queues*. This enables other VIs, such as the *sequencer.vi* shown in figure 7 to be used to control the SM in *torque.vi* programmatically by sending these commands directly to the SM (wide arrow ② in figure 7).

When automatic measurements are required, a sequence text file is written containing the commands needed to accomplish these measurements which is then read by the *sequencer.vi*. Additionally to the commands of *torque.vi's* SM, the *sequencer.vi* understands a set of flow control instructions such as 'if', 'while' and 'for' which are useful for creating short sequences for repetitive tasks, as well as the use of variables and their arithmetic manipulation and comparison.

The *sequencer.vi* parses through the sequence file by looking for known keywords—the commands. Any strings

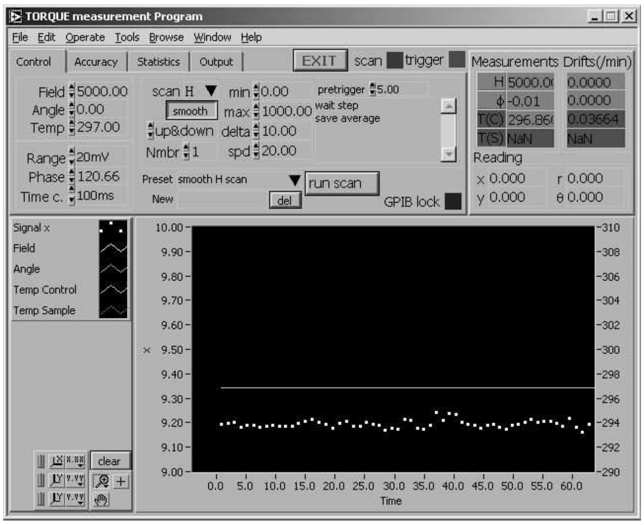
TORQUE measurement Program

Field 5000.00
Angle 0.00
Temp 297.00
Range 20mV
Phase 120.66
Time c. 100ms
scan H
up&down
Nmbr 1
min 0.00
max 1000.00
delta 10.00
spd 20.00
pretrigger 5.00
wait step
save average
Preset smooth H scan
New

Measurements		Drifts(/min)
H	5000.0	0.0000
ϕ	-0.01	0.0000
T(C)	296.86	0.03664
T(S)	NaN	NaN

Reading
x 0.000
y 0.000
r 0.000
θ 0.000

Figure 6. Screenshot of the main *torque.vi* during a measurement. Controls and indicators for measurement taking are arranged at the top. The currently obtained data are visualized in the large *X–Y* graph at the bottom.

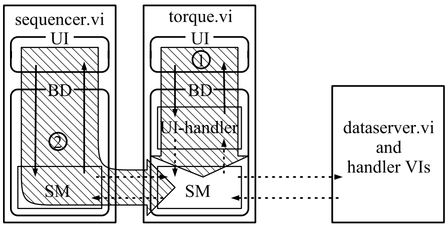

Figure 7. All VIs consist of a UI and a BD. In contrast to all other VIs the *torque.vi's* BD consists of the UI-handler part and the SM itself, both running in parallel. In normal, interactive operation of the torque system, user actions on the *torque.vi's* UI are translated by the UI-handler into commands which are sent to the SM via a queue and then propagate on to the dataserver and handler VIs (wide arrow ①). If an automated measurement is run, the *sequencer.vi's* SM retrieves commands from the text sequence on its UI and sends them via a queue to the *torque.vi's* SM from where they propagate on to the dataserver and handler VIs (wide arrow ②). The *torque.vi's* SM sends confirmation messages back to the *sequencer.vi*. Solid black arrows indicate direct access between the BD and the UI, whereas dotted arrows represent data transmission via *queues* and *DataSockets*.

which are not recognized as a keyword are treated as arguments to the preceding keyword. The string `settemp 20 waittemp` present in a sequence file would instruct the torque software to change the temperature to 20 K and wait for the cryostat to stabilize at this temperature. In this example `settemp` and `waittemp` are keywords and 20 is the argument to the keyword `settemp`. This makes possible efficient and flexible data taking with our homemade torque magnetometer. We emphasize that the software architecture described in this paper is of a general nature and easily applied to other laboratory equipment. Figure 8 shows a screenshot of the *sequencer.vi* during a measurement. The measurement sequence is entered in the large text area. During its execution, the current values of the variables in use are shown in the lower part.

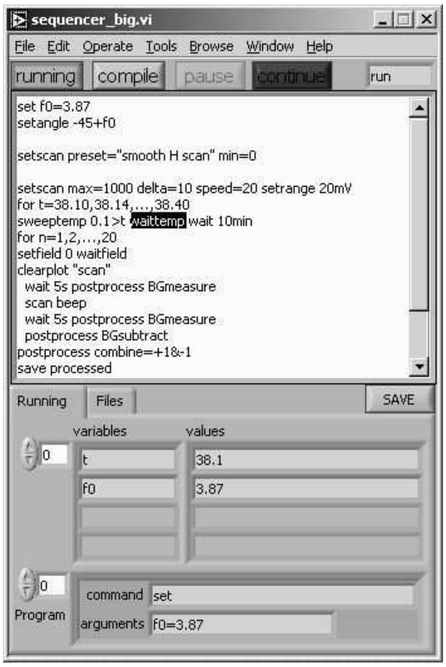
sequencer_big.vi

```
set f0=3.87
setangle -45+f0

setscan preset="smooth H scan" min=0

setscan max=1000 delta=10 speed=20 setrange 20mV
for t=38.10,38.14,...,38.40
sweeptemp 0.1>t waittemp wait 10min
for n=1,2,...,20
setfield 0 waitfield
clearplot "scan"
  wait 5s postprocess BGmeasure
  scan beep
  wait 5s postprocess BGmeasure
  postprocess BGsubtract
postprocess combine=+1&-1
save processed
```

variables	values
t	38.1
f0	3.87

command set
arguments f0=3.87

Figure 8. Screenshot of the *sequencer.vi*, while an automatic measurement taking is in progress. The sequence is input into the large text area at the top. In the bottom half, the current values of the variables are presented during execution.

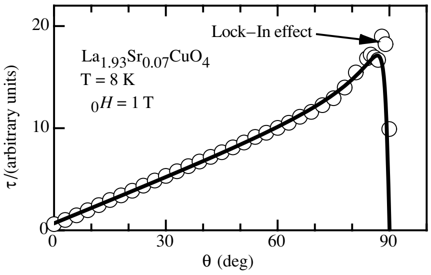

Figure 9. Angle-dependent torque measurement (circles) of an underdoped crystal of $La_{2-x}Sr_xCuO_4$ with $x = 0.07$ ($T_c = 17$ K), performed at $T = 8$ K in a magnetic field $\mu_0 H = 1$ T. The solid line is a fit of a model derived by Kogan [11]. The deviation close to $\theta \approx 90°$ stems from the lock-in transition.

6. Example of application

In order to demonstrate the possibilities of such an automatable measurement system, we present some results of a systematic study of the so-called lock-in transition in the high temperature superconductor $La_{2-x}Sr_xCuO_4$ [8]. Details about this effect can be obtained from various other sources and are not discussed here [9, 10]. This effect is most easily visible in angle-dependent torque measurements and manifests itself as a deviation from otherwise smooth behaviour. An example of such a measurement is shown in figure 9, where the measured data points close to 90° deviate from a theoretical curve which fits well to the remaining angle range. The same model can also be used to describe data taken as a function of magnetic field magnitude H at a fixed angle. It is commonly accepted that in a first approximation the magnetic moment $m = \tau/H$ of a superconductor is proportional to $\ln(H)$ [11].

Within our study we measured six $La_{2-x}Sr_xCuO_4$ single micro-crystals with varying Sr content $0.07 \leqslant x \leqslant 0.23$ and critical temperatures T_c varying from 17 K to 35 K. They were mounted on a highly sensitive torque sensor and cooled below T_c. Field-dependent measurements ($\mu_0 H = 0$–1.5 T at 5 mT steps with increasing and decreasing field) were taken at 60 field orientations ($\theta = -90°$–90° with varying steps) and at about ten temperatures below the critical temperature T_c. We emphasize that such extensive measurements would hardly be possible without our software's automation possibilities. As each field scan takes about 6 min, without automation user interaction would be necessary at this interval for *one week* to collect all these data for one crystal. After writing the sequence and starting its execution, the measurement system, on the other hand, finishes such a measurement set within about *three days* with no need of intervention. The experiment is finished faster, because less time is lost between consecutive field scans and because the measurement is running day and night.

We present here only one dataset of a single crystal taken at one particular temperature. Such a dataset consists of 60 field scans taken at various orientations. The two field scans shown in figure 10 illustrate the deviations of field-dependent data due to the lock-in transition. Clearly visible are two regions (I and II) where τ/H is proportional to $\ln(H)$. A comparison of these measurements to angle-dependent measurements at similar conditions indicates that region I corresponds to the part where lock-in takes place, whereas data in region II are well described by the theoretical curve in figure 9. By analysing the whole dataset, it is now easy to investigate the evolution of these two regions as a function of angle θ. The result is shown in figure 11, where the extents of the two regions, obtained from field-dependent measurements, are plotted versus the angle θ. The horizontal line A indicates the cut of the measurement in figure 9 and the vertical lines B and C the measurements shown in figure 10. The observed region separating regions I and II manifests the lock-in transition and can be understood in terms of a model proposed by Feinberg and Villard [12].

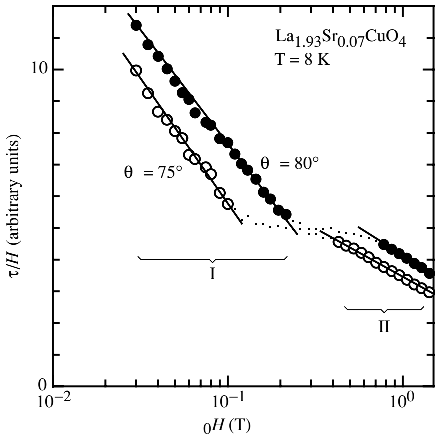

Figure 10. Field-dependent measurement $\tau(H)$ of the same $La_{2-x}Sr_xCuO_4$ crystal as was used for the measurement in figure 9. The angle of the magnetic field was fixed at $\theta = 75°$ and $\theta = 80°$. The measurements are plotted as τ/H versus $\ln(H)$. The lines are guides to the eye to show the two linear regions I (low field) and II (high field).

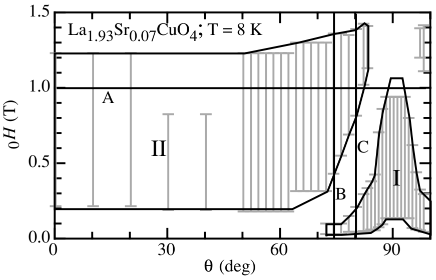

Figure 11. Summary of field-dependent measurements performed on a $La_{2-x}Sr_xCuO_4$ single crystal at $T = 8$ K. Only the extents of the linear regions such as shown in figure 10 as a function of field orientation θ are shown. The enhancement of the low-field region I close to the ab plane ($\theta \approx 90°$) is clearly visible. The horizontal line A indicates the position of the measurement shown in figure 9. The vertical lines B and C indicate the positions of the measurements shown in figure 10.

Acknowledgments

This work was supported in part by the Swiss National Science Foundation.

References

[1] LabVIEW http://www.ni.com/labview/

[2] Willemin M, Rossel C, Brugger J, Despont M H, Rothuizen H, Vettiger P, Hofer J and Keller H 1998 Piezoresistive cantilever designed for torque magnetometry *J. Appl. Phys.* **83** 1163

[3] Rossel C, Willemin M, Gasser A, Bothuizen H, Meijer G I and Keller H 1998 Torsion cantilever as magnetic torque sensor *Rev. Sci. Instrum.* **69** 3199

[4] Gill A 1962 *Introduction to the Theory of Finite-state Machines* (New York: McGraw-Hill)

[5] Gruggett L 1995 State your case! *LabVIEW Tech. Resour.* **3** 12–4

[6] Bitter R, Mohiuddin T and Nawrocki M 2001 *LabVIEW Advanced Programming Techniques* chapter 3, State Machines (Boca Raton, FL: CRC Press)

[7] Application design patterns: State machines *National Instruments Developer Zone*

[8] Kohout S, Schneider T, Roos J, Sasagawa T and Takagi H 2005 Systematic study of the lock-in transition in $La_{2-x}Sr_xCuO_4$ in preparation

[9] Blatter G, Feigel'man M V, Geshkenbein V B, Larkin A I and Vinokur V M 1994 Vortices in high-temperature superconductors *Rev. Mod. Phys.* **66** 1125

[10] Steinmeyer F, Kleiner R, Müller P and Winzer K 1994 Lock-in transition in layered superconductors *Physica* B **194** 2401–2

[11] Kogan V G 1988 Uniaxial superconducting particle in intermediate magnetic fields *Phys. Rev.* B **38** 7049

[12] Feinberg D and Villard C 1990 Intrinsic pinning and lock-in transition of flux lines in layered type-II superconductors *Phys. Rev. Lett.* **65** 919

Part II

Magnetic properties of novel superconductors

Chapter 4

Introduction

Superconductivity was first observed in 1911 by H. Kamerlingh-Onnes [Onn11] in form of the *perfect conductivity* of Hg below 4.1 K. Twenty years later, in 1933, W. Meissner and R. Ochsenfeld [MO33] discovered another aspect of superconductivity. The observed expulsion of a magnetic field from a sample, the *perfect diamagnetism*, was named Meissner-Ochsenfeld effect after them. Each effect on its own is not sufficient to describe superconductivity. Only the combination of both causes this new state to be a thermodynamic one. However, superconductivity is destroyed if the applied magnetic field exceeds the critical field H_c. The high-temperature superconductors discovered in 1986 by J.G. Bednorz and K.A. Müller [BM86] show this behavior as well. However, the critical temperature and the critical field are observed to be considerably higher. Moreover, these materials have a layered structure, which makes them highly anisotropic. This means that various superconducting properties depend strongly on the direction with respect to the cristallographic axes. This anisotropy makes these materials useful for magnetic torque investigations. In fact, isotropic materials cannot be investigated with torque magnetometry.

The improved apparatus presented in the first part of this thesis was applied to measurements of magnetic properties of high-temperature superconductors. The automatic execution of long sequences allowed a thorough study of key magnetic properties of these materials, such as the correlation lengths along different crystallographic directions, the magnetic penetration depth and the anisotropy parameter. In this chapter, the theories used to extract these properties from measurements are presented after a short overview of general properties of the high-temperature superconductors.

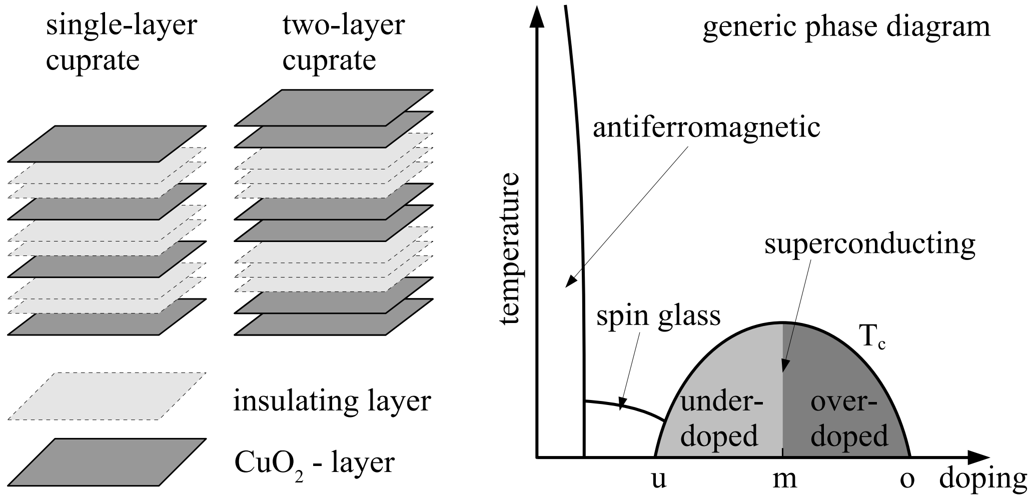

Figure 4.1: Generic layered structure (left) and phase diagram (right) of the cuprate high-temperature superconductors.

4.1 Materials: the cuprate families

High-temperature superconductivity was discovered in the $La_{2-x}Ba_xCuO_4$ system [BM86]. Other subsequently found compounds had similar structures, sharing the CuO_2 planes, as shown in the left panel of Fig. 4.1. It is generally agreed that these planes hold the superconducting carriers. The number of superconducting CuO_2 planes and intermediate insulating planes was found to strongly affect the superconducting properties. In the Bi-Sr-Ca-Cu-O system, for example, the number of directly adjacent CuO_2 planes can be varied from one to three, causing the critical temperature T_c to increase considerably with each additional plane. Currently, the highest $T_c = 139\,K$ is achieved in the Hg-Ba-Ca-Cu-O system, established in 1995 [DCS+95] after a breakthrough in 1993 [SCGO93]. With applied pressure, it can even be increased up to 160 K [CGC+93].

In these compounds, the superconducting properties heavily depend on the so-called doping state of the sample, namely the amount of free charges present in the CuO_2 planes. The critical temperature T_c, where superconductivity sets in, depends quadratically on this doping level in a first approximation. This is illustrated in the right panel of Fig. 4.1. The superconducting transition temperature T_c increases from the underdoped limit (marked "u") up to optimal doping ("m") and decreases towards the overdoped limit ("o"), where it vanishes. The doping can be changed by various methods. In $La_{2-x}Sr_xCuO_4$ and $La_{2-x}Ba_xCuO_4$, the doping is controlled by the amount of

Sr and Ba, respectively. Effectively, the substitution of these 2+ charged ions for the La^{3+} ions removes electrons from the material. The missing electrons, or additional holes, are mobile in the CuO_2 planes and are believed to be the constituents of the superconducting charge carriers. So-called electron-doped materials such as $Nd_{2-x}Cu_xCuO_4$, where additional electrons instead of holes are introduced to the material are known to superconduct as well. They are not as widely investigated as the popular hole-doped cuprates. Other compounds, such as $YBa_2Cu_3O_{7-\delta}$, are mainly doped by the variation of their oxygen content $7-\delta$. At $\delta = 0$, the substance is optimally doped, and becomes underdoped with increasing δ. The doping state of an existing sample can easily be changed with appropriate heating procedures. Oxygen is removed from the sample at high temperatures (up to 900 °C). This reduced oxygen content can be frozen if cooled down quickly enough. Best results are obtained by quenching the sample in mercury which is held at room temperature. However, the overdoped regime is nearly inaccessible in this compound. Only slightly overdoped samples can be produced. The maximum T_c lies around 90 K for optimum doping. Another commonality of these materials is that their undoped compositions ($x = 0$ in $La_{2-x}Sr_xCuO_4$ and $La_{2-x}Ba_xCuO_4$ or $\delta = 1$ in $YBa_2Cu_3O_{7-\delta}$) are antiferromagnetic insulators.

4.2 Theories on superconductivity

There exist many theories on superconductivity. The reproduction of all aspects of these theories would reach far beyond the scope of this thesis. Therefore, only short summaries and general ideas needed for understanding the following chapters are given.

4.2.1 The London model

Soon after the discovery of the Meissner-Ochsenfeld effect, the brothers F. and H. London [LL35] proposed in 1935 two equations to describe the electric and magnetic fields inside a superconductor. The dissipationless current **j** due to an electric field **E**

$$\frac{\mathrm{d}\mathbf{j}}{\mathrm{d}t} = \frac{n_\mathrm{S} e^2}{M}\mathbf{E} \tag{4.1}$$

is usually referred to as the *first London equation*, where n_S and M are the concentration and mass of the superconducting charge carriers, respectively. This equation can be rewritten as

$$\frac{\mathrm{d}}{\mathrm{d}t}\left(\nabla \times \mathbf{j} + \frac{n_\mathrm{S} e^2}{M}\mathbf{B}\right) = 0. \tag{4.2}$$

Any static magnetic fields $\mathbf{B}$ and current densities $\mathbf{j}$ are solutions of this equation. However, the experiment showed that $\mathbf{B} = 0$ inside a superconductor. The London brothers discovered that this can be explained with a restriction to solutions which obey the *second London equation*

$$\nabla \times \mathbf{j} + \frac{n_{\mathrm{S}} e^2}{M} \mathbf{B} = 0. \tag{4.3}$$

This leads directly to the Meissner-Ochsenfeld effect. Solutions for both London equations must be of the form

$$\lambda_{\mathrm{L}} \nabla^2 \mathbf{B} = \mathbf{B} \tag{4.4}$$

with the *London penetration depth* λ_{L}

$$\frac{1}{\lambda_{\mathrm{L}}^2} = \frac{\mu_0 n_{\mathrm{S}} e^2}{M}. \tag{4.5}$$

The simplest solution is $\mathbf{B} = \mathbf{B_0} \exp(-x/\lambda_{\mathrm{L}})$, a field decaying exponentially from the planar surface within the superconducting sample. This simple phenomenological approach already describes the essential features of superconductivity, namely perfect conductivity and perfect diamagnetism.

4.2.2 Ginzburg-Landau theory

In 1950, V.L. Ginzburg and L.D. Landau [GL50] introduced a very powerful phenomenological theory of superconductivity, which describes the behavior of a superconductor in an external magnetic field. They introduced a complex order parameter ψ, treated within Landau's general theory of second order phase transitions. This order parameter can be connected to the local density of superconducting charge carriers by

$$n_{\mathrm{S}} = |\psi(x)|^2. \tag{4.6}$$

The differential equation for ψ is not reproduced here. This consideration of spatial variations of n_{S} resulted in the introduction of another characteristic length scale, the *Ginzburg-Landau (GL) coherence length* ξ. The superconducting order parameter ψ (and consequently the carrier density n_{S}) cannot vary over shorter distances than ξ without large energy requirements. Both the London penetration depth λ_{L} and the GL coherence length ξ are temperature dependent and diverge upon approaching T_{c}. However, their ratio

$$\kappa = \frac{\lambda_{\mathrm{L}}}{\xi} \tag{4.7}$$

called the *GL parameter* is approximately constant with temperature.

In the superconductors known up to then, the correlation length was found to be $\xi \gg \lambda_\mathrm{L}$, or $\kappa \ll 1$. However, A. Abrikosov [Abr57] found in 1957, that a large GL parameter $\kappa \gg 1$ would cause the energy associated with the surface between normal and superconducting regions to be negative. Thus, the energetically favorable state would be one with as much surface as possible. Instead of a rather homogeneous expulsion of field (the Meissner-Ochsenfeld Effect), this would cause the sample to become strongly tessellated with normal and superconducting regions. This state is called the mixed state. Abrikosov calculated, that each normal state region would carry a single quantum of flux

$$\Phi_0 = \frac{h}{2e} = 2.07 \times 10^{-15}\,\mathrm{Tm}^2 \tag{4.8}$$

and that these flux tubes (called vortices) would form a regular array. Due to this striking difference, superconductors with $\kappa > 1/\sqrt{2}$ are called *type II*, whereas the ones with $\kappa < 1/\sqrt{2}$ are called *type I*. The first vortex enters the sample at the lower critical field H_{c1}. More vortices enter the sample with increasing field, up to the upper critical field H_{c2}, when no more superconducting regions exist in the sample. Whereas conventional, low temperature superconductors such as Hg, Al, Pb or others can be of type I or type II, most of the newly discovered *high-*T_c compounds are of type II.

4.2.3 BCS-theory

After these phenomenological theories, J. Bardeen, L.N. Cooper and J.R. Schrieffer [BCS57] presented their microscopic BCS theory for superconductivity in 1957. It explained dissipationless charge transport due to the pairing of electrons via a weak interaction with the lattice to form the so-called Cooper-pairs. This pairing is associated with the formation of a temperature dependent energy gap Δ. The minimum energy of 2Δ is needed to break a Cooper pair, making the paired state stable up to a critical temperature T_c. The BCS theory predicts

$$\frac{2\Delta(T=0)}{k_\mathrm{B}T_\mathrm{c}} = 3.528, \tag{4.9}$$

in good agreement with experiment. The measured quotients were mostly between 3 and 4. The BCS theory is very successful in describing other phenomena of superconductivity, though it is insufficient to explain superconductivity in the newly discovered high-temperature superconductors.

4.2.4 Anisotropic Ginzburg-Landau theory (AGLT)

The layered structure of the high-temperature superconductors suggests, that properties along the $\mathrm{CuO_2}$-planes (ab-directions) are essentially different from those perpendicular to these planes (c-direction). Such an anisotropy can be introduced into the Ginzburg-Landau equations mentioned (though not reproduced) above by replacing the scalar charge carrier mass by a mass tensor with different principal values m_a, m_b and m_c along the three crystallographic directions a, b and c. The much stronger interaction along the planes than perpendicular to the planes can be expressed as $m_c \gg m_a, m_b$. In tetragonal structures $m_a = m_b = m_{ab}$ can be assumed. Note that there is a small in-plane anisotropy in orthorhombic structures, which can usually be neglected compared to the much larger perpendicular anisotropy. The mass anisotropy causes the correlation length ξ, the penetration depth λ and the critical fields H_{c1} and H_{c2} to become anisotropic as well. A single anisotropy parameter

$$\gamma = \sqrt{\frac{m_c}{m_{ab}}} = \frac{\lambda_c}{\lambda_{ab}} = \frac{\xi_{ab}}{\xi_c} = \frac{H_{\mathrm{c2},ab}}{H_{\mathrm{c2},c}} = \frac{H_{\mathrm{c1},c}}{H_{\mathrm{c1},ab}} \tag{4.10}$$

suffices to describe these anisotropies.

The Ginzburg-Landau equations become nonlinear upon approaching H_{c1}. Consequently their solution is not possible. Therefore V.G. Kogan used the London model, which is a reasonable approximation for large Ginzburg-Landau parameters $\kappa = \lambda/\xi$. Thus, he obtained a formula for the torque upon a superconducting particle in intermediate magnetic fields H (i.e. $H_{\mathrm{c1}} \ll H \ll H_{\mathrm{c2}}$) [Kog88].

$$\tau = \frac{\Phi_0 V}{16\pi\lambda_{ab}^2} H(1-\gamma^{-2}) \frac{\sin 2\theta}{\varepsilon(\theta)} \ln\left(\frac{\eta H_{\mathrm{c2},c}}{H\varepsilon(\theta)}\right), \tag{4.11}$$

with

$$\epsilon(\theta) = \sqrt{\gamma^{-2}\sin^2\theta + \cos^2\theta}. \tag{4.12}$$

Another, less approximate expression for the torque on a superconducting particle is given by Z. Hao and J.R. Clem [HC91], but due to its complexity it is not covered in this work. Moreover, Eq. (4.11) is widely used and accepted for evaluation of torque data and has proved useful for this purpose.

4.2.5 Lawrence-Doniach model

W.E. Lawrence and S. Doniach [LD72] proposed to make the continuous order parameter $\psi(x, y, z)$ discrete along the direction z perpendicular to the ab-planes, replacing it by $\psi_n(x, y)$. This describes a set of interacting, superconducting planes. Gradients $\mathrm{d}\psi/\mathrm{d}z$ in the Ginzburg-Landau equations are thus replaced by differences $(\psi_n - \psi_{n-1})/s$ with the inter-plane spacing s. This model was extensively applied to conventional, layered superconductors. Together with AGLT it was also used to describe interesting 2D-3D crossover phenomena in high-temperature superconductors.

4.2.6 Scaling theory

The approach of T. Schneider and J.M. Singer [SS00] is substantially different. Knowing that near a phase transition critical fluctuations play an important role, they start from the basic, thermodynamic assumption that the energy density must be of the form

$$f = \frac{k_\mathrm{B}T}{\xi_a^- \xi_b^- \xi_c^-}, \tag{4.13}$$

where ξ_a^-, ξ_b^- and ξ_c^- are the correlation lengths of these critical fluctuations below T_c. Such fluctuations exist above T_c as well and these effects are also covered in their investigations. However, these results are not covered in the short summary presented here. It is found, that the cuprate superconductors belong to the 3D-XY universality class, where the system is three dimensional with a two-component order parameter. Physical properties of a system close to a phase transition obey universal power laws. The exponents of these power laws are identical for all systems in a specific universality class. This allows the detection and comparison of such similarities and for the formulation of powerful statements.

The torque on a sample close to the phase transition at T_c and in weak magnetic fields is found to be

$$\tau = \frac{-Q_3^- C_{3,0}^- k_\mathrm{B} T V}{2\Phi_0 \xi_c^-} \mu_0 H \left(1 - \gamma^{-2}\right) \frac{\sin 2\theta}{\varepsilon(\theta)} \ln\left(\frac{\mu_0 (\xi_{ab}^-)^2}{\Phi_0} H \varepsilon(\theta)\right) \tag{4.14}$$

with the same anisotropy scaling function as used in the AGLT

$$\epsilon(\theta) = \sqrt{\gamma^{-2}\sin^2(\theta) + \cos^2(\theta)}. \tag{4.15}$$

Comparing Eqs. (4.11) and (4.14), one realizes that they have the same functional dependence on the field H and on the angle θ. Since the approach of Schneider and Singer is based on critical fluctuations, it is valid only close to T_c. Therefore, Kogan's interpretation should be used for the analysis of data taken considerably below T_c.

It should also be noted that, even though the correlation lengths ξ_i^- look similar to the correlation length which can be derived from Eq. (4.11) by

$$H_{\mathrm{c}2,c} = \frac{\Phi_0}{2\pi\mu_0\xi_{ab}^2}, \tag{4.16}$$

they are not related. The ξ_i^-'s are defined only close to T_c, where they diverge as

$$\xi_i^-(T) = \xi_{i,0}^-\left(1 - \frac{T}{T_\mathrm{c}}\right)^{-\nu}, \tag{4.17}$$

where $\nu = 2/3$ is an exponent universal within the so-called 3D-XY universality class. The 3D indicates the fact, that the system under investigation is essentially three dimensional. The term XY means that the order parameter is a two dimensional vector (or a complex quantity). Away from the underdoped limit and close to the critical temperature T_c, the high-temperature superconductors are believed to belong to this universality class. The zero temperature correlation length $\xi_i(0)$ and the critical correlation length amplitude $\xi_{i,0}^-$ are not related, though they are often similar.

Chapter 5

Vortices and anisotropies

Torque measurements are principally performed as a function of temperature T, magnetic field strength H and the angle θ of the field with respect to the cristallographic orientation of the sample. Temperature dependent measurements serve well for the determination of T_{c}. The anisotropy parameter γ [Eq. (4.10)] of the sample can be deduced from the angle dependence, either from direct angle dependent measurements at fixed field or from the variation of several measurements as a function of magnetic field at various fixed angles. The first approach is straightforward and was used until now almost uniquely to measure γ. In this work, the latter approach was used, where several field dependent measurements are taken and individually fit to the field dependent part

$$\tau = m_\theta \mu_0 H \ln\left(\frac{H}{H_\theta}\right) \tag{5.1}$$

of Eq. (4.14). The fit parameters m_θ and H_θ are subsequently fit to their individual angle dependence

$$m_\theta = m_0\left(1-\gamma^{-2}\right)\frac{\sin 2\theta}{\varepsilon(\theta)} \tag{5.2}$$

and

$$H_\theta = \frac{H_0}{\varepsilon(\theta)}, \tag{5.3}$$

which allows the determination of the anisotropy γ. The angle dependences of τ, m_θ and H_θ are shown in Fig. 5.1 for various values of γ. It is clearly seen that the best estimates for γ are obtained from measurements close to 90°. However, as will be shown later, this is the region where measurements are problematic due to transformations of the vortex lattice.

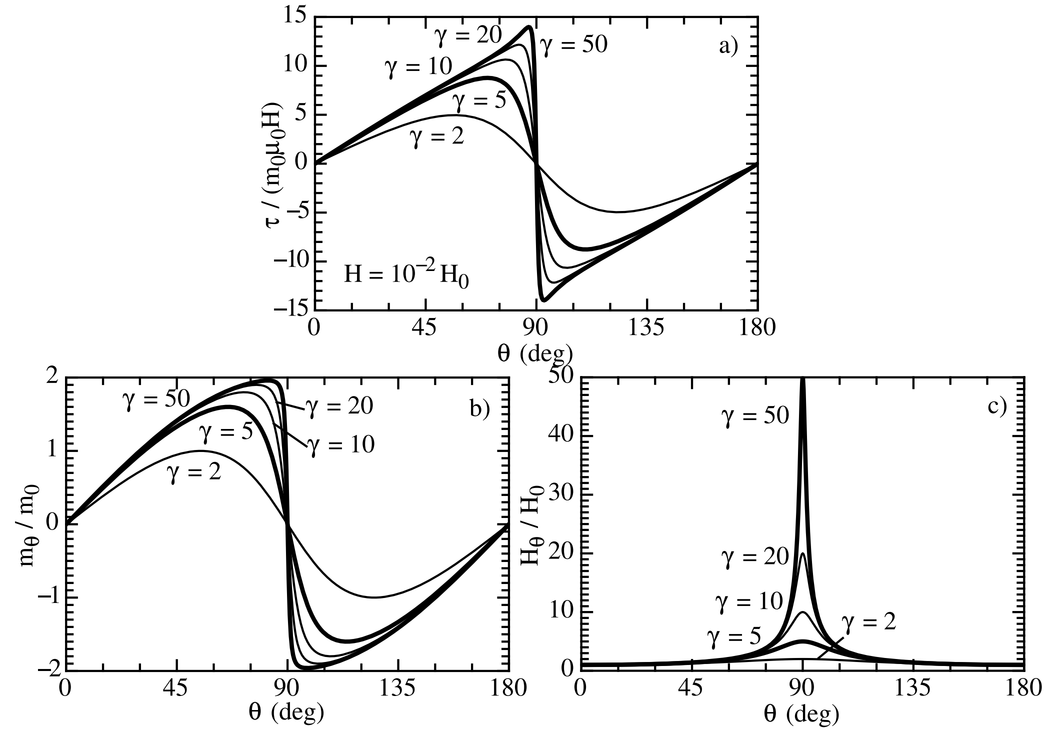

Figure 5.1: The theoretical angle dependence of τ (a), m_θ (b) and H_θ (c) for different anisotropies γ in the equations (4.14), (5.2) and (5.3).

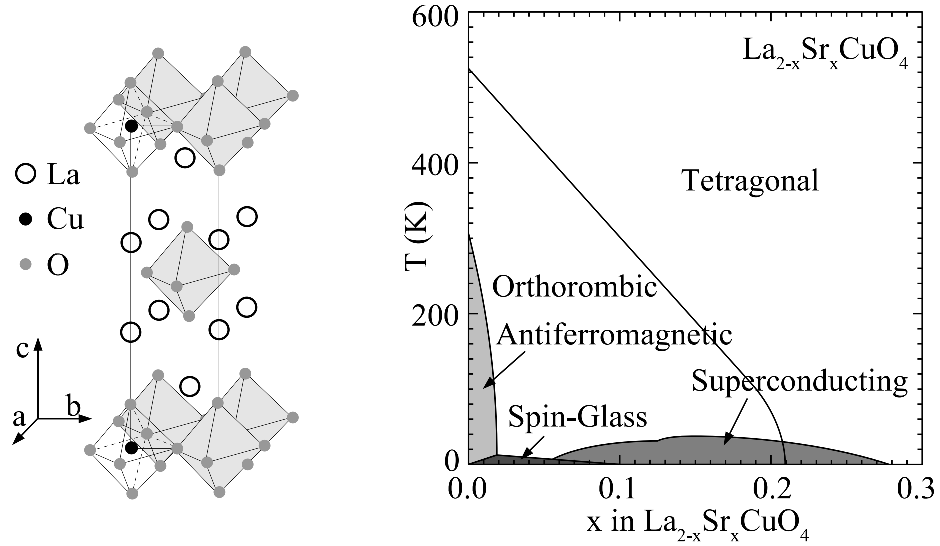

Figure 5.2: Structure (left) and phase diagram (right) of the high-temperature superconductor $La_{2-x}Sr_xCuO_4$ (after [Joh97]).

5.1 Vortex configurations in $La_{2-x}Sr_xCuO_4$

The $La_{2-x}Sr_xCuO_4$ cuprate superconductor is derived from the La_2CuO_4 parent compound, an antiferromagnetic insulator. It has one of the simplest structures within the cuprates and can easily be doped with Sr (this work) or Ba [BM86] substituted for La. Its structure and phase diagram are shown in Fig. 5.2. The unsubstituted ($x = 0$) parent compound is insulating and antiferromagnetic with the Néel temperature $T_{\mathrm{N}} \approx 300\,\mathrm{K}$. With increasing Sr content x, T_{N} is strongly reduced and vanishes at $x = 0.01$. At high temperature, the compound is still insulating, while there exists a spin glass state at low temperature. Superconductivity appears between the under- and overdoped limits $x_{\mathrm{u}} \approx 0.05$ and $x_{\mathrm{o}} \approx 0.27$, respectively. At optimal doping around $x_{\mathrm{m}} \approx 0.15$, the critical temperature reaches its maximum value $T_{\mathrm{c,m}} \approx 40\,\mathrm{K}$, depending on the sample quality. Usually, single crystals have lower T_{c}'s than powders. A structural transition between a high temperature tetragonal phase and a low temperature orthorombic phase is also known, but unimportant for this study.

Samples of $La_{2-x}Sr_xCuO_4$ with $x = 0.07, 0.108, 0.125, 0.15, 0.19,$ and 0.23 were grown with the traveling-solvent floating-zone (TSFZ) method by T. Sasagawa [SKT$^+$98]. Small parts were broken off the grown crystals in order to obtain micro crystals of approximately $100 \times 100 \times 50\,\mu\mathrm{m}^3$ size. Measurements were performed using the highly sensitive capacitive torsion torque

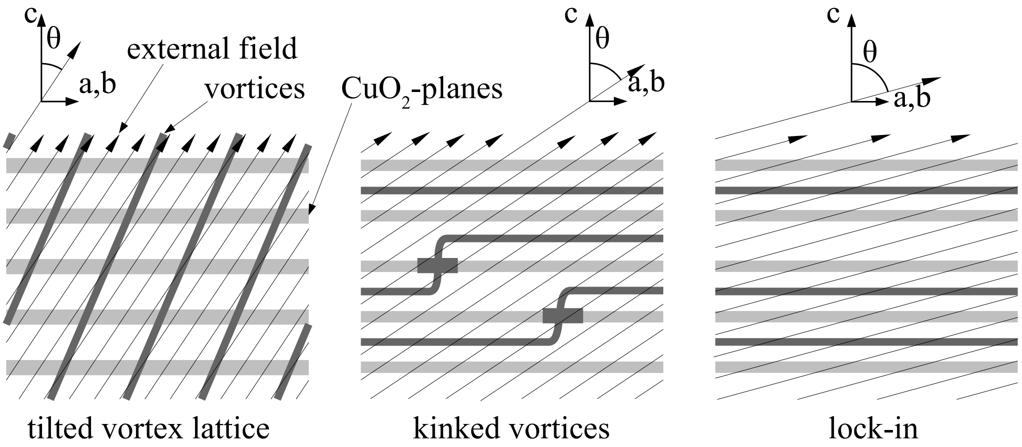

Figure 5.3: Schematic illustration of transformations of the vortex lattice. When θ, the angle between the applied magnetic field and the sample's c-axis is not too large, the ordinary lattice of tilted Abrikosov vortices is observed (left). At large angles, kinked Josephson vortices start to appear (middle). Finally, when the magnetic field is close to being aligned with the sample's ab-planes, the vortices lock in (right). The critical angles highly depend on the magnetic field strength.

sensors as described in section 1.2 on page 9.

Careful analysis of the systematically measured data revealed the occurrence of three different vortex configurations. The first is the lattice of ordinary, Abrikosov vortices (AV). It can persist up to large angles θ, the angle between the magnetic field and the sample's c-axis. When the field direction approaches the orientation of the CuO_2-planes, these Abrikosov vortices are replaced by kinked vortices (KV). These are made up of Josephson vortices lying aligned between the CuO_2-planes interconnected by so-called pancake vortices within the planes. If the field is oriented sufficiently close to the ab-plane of the sample, these pancakes disappear – the vortices are said to be locked in (LIV) [BFG$^+$94]. An illustration is given in Fig. 5.3.

These different configurations can be distinguished in magnetic torque measurements by their different angle- and field dependences. The AV phase is well described by Eqs. (4.11) or (4.14) with its characteristic asymmetric $\sin(2\theta)$ angle dependence and a logarithmic dependence of τ/H on field H. The KV phase is very similar in that it shares the logarithmic field dependence. However, the angle dependence deviates from that of the AV phase. In fact, torque strongly increases close to the CuO_2-planes compared to the AV model. This strong increase has been observed in torque measurements of

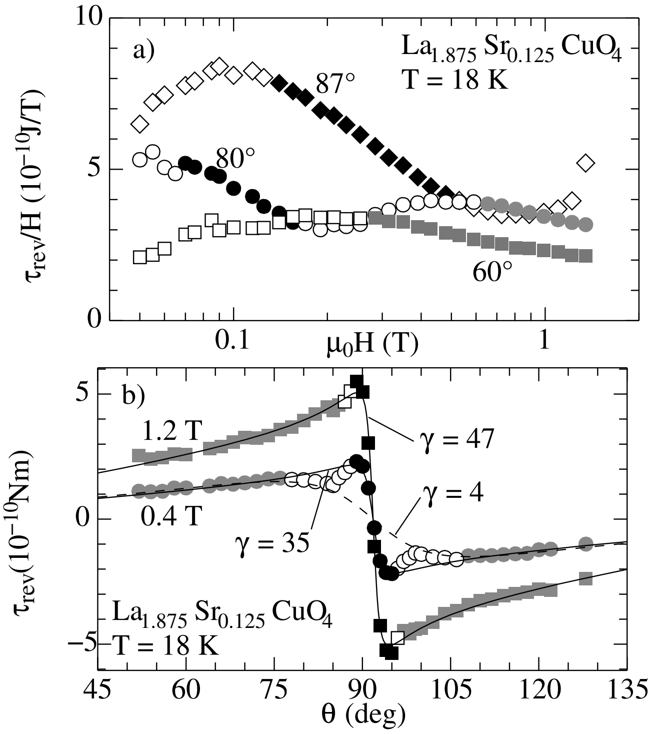

Figure 5.4: Signature of kinked vortices in single-crystal $La_{2-x}Sr_xCuO_4$ ($x = 0.125$). a) Magnetic torque τ_{rev}/H vs H as measured for various angles (squares: $\theta = 60°$, circles: $\theta = 80°$, diamonds: $\theta = 87°$) at 18 K. Linear regions in high magnetic fields (gray symbols) are from the Abrikosov vortex lattice. Linear regions at low fields close to $\theta = 90°$ as shown by the filled symbols are attributed to kinked vortices. b) Data from the same measurements plotted vs orientation angle θ at constant magnetic fields $\mu_0 H = 0.4\,T$ (circles) and $\mu_0 H = 1.2\,T$ (squares). Gray and black filled symbols are attributed by analogy to the linear regions in a) to the Abrikosov and kinked vortex phase, respectively.

strongly anisotropic materials like $YBa_2Cu_3O_{7-\delta}$, the $Bi_2Sr_2CaCu_2O_{8+\delta}$ families or even organic superconducting materials [SKMW94, ZRL+96, KIO+92, TAY+02, ACS+01] and has been taken as a clear signature of lock-in. However, as will be shown later, this feature is attributed to the KV. For the LIV, a quadratic field dependence was calculated [MP91]. Examples of angle- and field dependent torque measurements are given in Fig. 5.4. The angle dependent measurement at 0.4 T nicely illustrates the increased torque close to 90° (black filled symbols). The strongly differing anisotropy values γ obtained from fits of Eq. (4.14) upon inclusion of different measured points show the difficulty of obtaining this parameter. The anisotropy ($\gamma \approx 36$ for this compound) should not vary with magnetic field magnitude. Inclusion of the points close to 90° yields an overestimation of γ, whereas the omission of these points causes an underestimation due to the lack of points in the crucial region around 90°.

In Fig. 5.4a, three field dependent measurements are shown, which correspond to the data shown in Fig. 5.4b. Points belonging to similar regions are filled correspondingly, in order to enable to link the two figures. If the field is applied far away from the CuO_2-planes, such as the measurement at $\theta = 60°$, a linear region is easily seen and extends from intermediate up to high magnetic fields. This is the part belonging to the AV phase. If, however, the magnetic field is rotated towards the CuO_2-planes, another linear region, attributed to the KV, appears at low fields ($\theta = 80°$), which grows when the field is aligned further with the CuO_2-planes ($\theta = 87°$). So close to the CuO_2-planes, the linear region of the AV has grown above the maximum field 1.5 T of our apparatus. Tracking the points in the linear regions back to the angle dependent measurement in Fig. 5.4b, the KV phase can be designated in the angle dependence and becomes clearly visible as the steep increase close to 90°. This discourages the interpretation, that this steep increase is due to the lock-in effect, since the field dependence is not quadratic.

Because the LIV region is restricted to angles θ closer to 90° than shown in these figures, the characteristic quadratic depedence is not visible here. By combining two or more measurements closest to 90° (e.g. by calculating the average slope $\mathrm{d}\tau/\mathrm{d}\theta$ at $\theta = 90°$ between adjacent measurements), the noise can be reduced and the quadratic dependence made visible. Figure 5.5 shows such a calculated slope vs applied magnetic field. A quadratic function can be fit up to 75 mT, as emphasized by filled symbols. Nevertheless, the conditions under which lock-in occurs remain difficult to determine due to the smallness of the torque signal at weak magnetic fields. They are shown merely to give an impression of how small this region is. The angle and field regions, where the three phases (AV, KV and LIV) are observed, are exemplarily for one sample at one temperature shown in Fig. 5.6. The shape

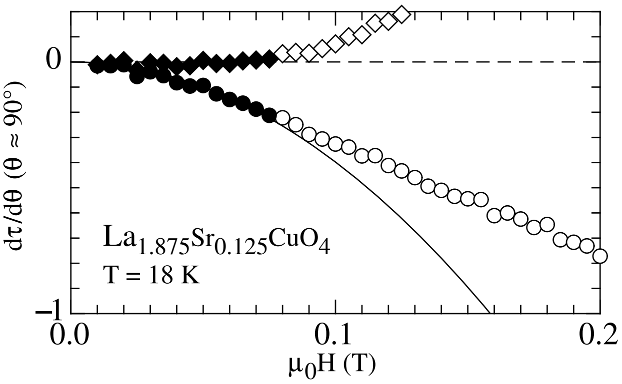

Figure 5.5: Slope $d\tau/d\theta$ of single-crystal $La_{2-x}Sr_xCuO_4$ ($x = 0.125$) close to $\theta = 90°$, obtained by fitting a straight line to τ vs θ for two measured points separated by 1° (circles). The curve is a quadratic fit to the points below 75 mT, as emphasized by filled symbols. Diamonds represent the difference between the fit and the measured data.

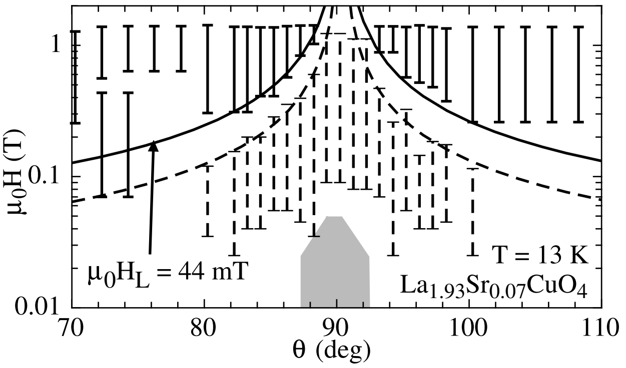

Figure 5.6: Vertical bars indicate the extent of the linear regions in single-crystal $La_{2-x}Sr_xCuO_4$ ($x = 0.07$) as in Fig. 5.4a vs the angle θ of the measurement. Solid and dotted bars represent the AV and the KV phase, respectively. The solid and dashed curves are fits of Eq. (5.4) to the lower bound of the AV and the upper bound of the KV, respectively. The shaded region illustrates the region where lock-in occurs.

of the boundary between the AV and KV regions is well described by the simple relation

$$H = \frac{H_{\mathrm{L}}}{\cos\theta} \tag{5.4}$$

proposed by Bulaevskii *et al.*.[BLK92] This is equivalent to stating that the perpendicular (to the sample's ab-plane) component of the applied magnetic field is equal to a limiting field H_{L}. With increasing temperature, the limiting field H_{L} decreases. An extrapolation shows that it does not vanish until the critical temperature T_{c} is reached.

The analysis of the whole data set obtained for the different crystals at various temperatures shows that, in order to determine the anisotropy parameter γ, only high field measurements close to the critical temperature should be considered. This knowledge is important for future studies, because a reliable method to determine γ is a key to performing more specific studies on the influence of different conditions on this important material property. The results presented in Fig. 5.7 were obtained by first fitting the angle dependent torque $\tau_{\mathrm{rev}}(\theta)$ at several fixed fields with Eq. (4.14) and then averaging the obtained values for γ where they were field independent. In Fig. 5.7 the such measured anisotropies γ and critical temperatures T_{c} of six differently doped samples are shown. Even though the points do not follow the empirical relations [PTB+91, TBS+95, Sch03, Sch04]

$$T_{\mathrm{c}} \propto x^2 \qquad \text{and} \qquad \gamma \propto x^{-1}, \tag{5.5}$$

as indicated by the continuous (in a) and dotted (in b) curves, it is clear that the universal relation

$$T_{\mathrm{c}} \propto \gamma^{-2} \tag{5.6}$$

introduced by Schneider [Sch05] is well obeyed. The dashed curves in Fig. 5.7 indicate the average of literature data for T_{c} measured before [TII+89, SH91, NU93, WRH+99, STS+00, Sch05]. The overall shift of the T_{c} dome toward lower doping is probably caused by the heat treatment to which the samples were subjected. The generally lower T_{c} is due to the fact that the measurements were obtained from single crystals, which generally exhibit lower T_{c}'s than powder samples.

In summary, the developments of torque sensory equipment and automation software presented in the first part of this thesis enabled the accomplishment of this study in high temperature superconductivity. It lead to the determination of angle-field-temperature regions with different vortex configurations and their influence on the determination of the anisotropy parameter γ. This allowed to establish a procedure to reliably measure this important quantity. It can be regarded as a foundation for future, more

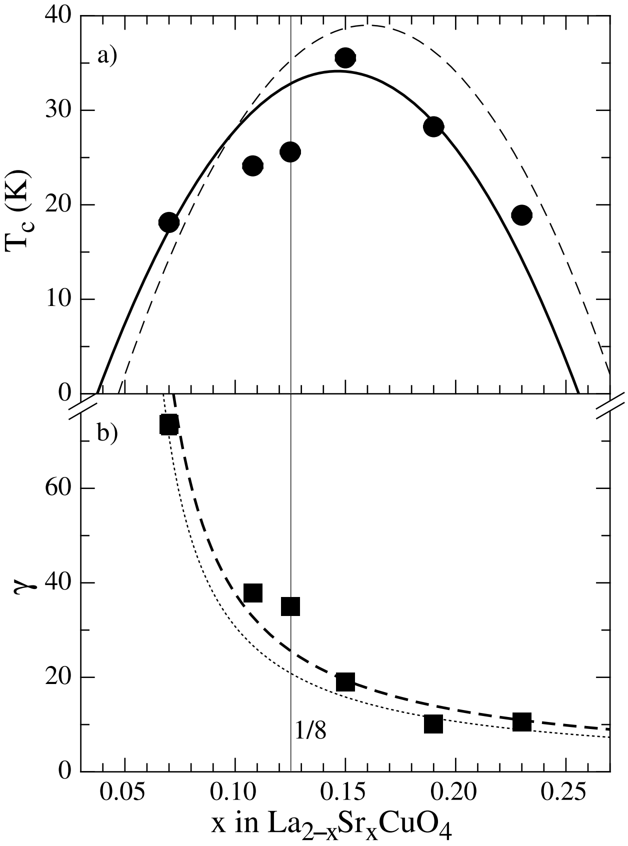

Figure 5.7: Critical temperature T_c (a) and anisotropy parameter γ (b) of single crystal $\mathrm{La}_{2-x}\mathrm{Sr}_x\mathrm{CuO}_4$ vs doping x, determined as described in the main text. Curves (solid: parabola, dotted: hyperbola) are guides to the eye according to Eq. (5.5). The curves serve as a comparison to the data shown in Fig. 1 of Ref. [Sch05].

complex experiments such as studies of the effect of isotope exchange on the anisotropy.

5.2 Related publication

Study of the Vortex States and Magnetic Anisotropy in Single Crystal $La_{2-x}Sr_xCuO_4$ *by Means of Torque Magnetometry*
S. Kohout, T. Schneider, T. Sasagawa, J. Roos, H. Takagi and H. Keller
submitted to Phys. Rev. B

Study of the Vortex States and Magnetic Anisotropy in Single Crystal $La_{2-x}Sr_xCuO_4$ by Means of Torque Magnetometry

S. Kohout,* T. Schneider, J. Roos, and H. Keller
Physik-Institut, Universität Zürich, Winterthurerstrasse 190, 8057 Zürich, Switzerland

T. Sasagawa and H. Takagi
Department of Advanced Materials Science, University of Tokyo,
5-1-5 Kashiwanoha, Kashiwa, Chiba 277-8561, Japan

(Dated: June 1, 2006)

The cuprate superconductors have highly anisotropic, layered structures. This causes the flux lattice penetrating them in the intermediate state to undergo dramatic changes when the direction of the applied magnetic field approaches the CuO_2 planes. We present highly sensitive torque measurements on tiny $La_{2-x}Sr_xCuO_4$ single crystals showing these regimes of vortex structure and their influence on the determination of the magnetic anisotropy parameter γ. Systematic measurements of torque as a function of magnetic field magnitude and orientation at various temperatures below T_c allowed to determine the conditions under which the structural changes occurs, allowing a reliable determination of γ. The values of γ obtained for $La_{2-x}Sr_xCuO_4$ as a function of doping x, covering the whole doping regime (under-, optimally, and overdoped) are in good agreement with earlier results, indicating a flow toward quasi-two-dimensionality in the underdoped limit.

I. INTRODUCTION

The mixed state in type-II superconductors, where magnetic flux enters a sample in form of single flux quantum vortices, is often used to extract and investigate various superconducting properties. Most of the models for these properties are based on a continuous anisotropic description. However, a lot of attention has always been attributed to the layered structure of these materials. A rich phase diagram has evolved from such calculations and measurements have been found to confirm such effects. Lawrence and Doniach[1] were the first to account for the layered structure and proposed a description, similar to the Ginzburg Landau theory, but specifically discretizing the equations along the *c*-direction perpendicular to the CuO_2 planes. Others based their calculations upon this work and found indications for strong intrinsic pinning if the applied magnetic field is oriented close to the CuO_2 planes.[2,3,3,4] Observations of lock-in were made on various layered superconductors, including cuprates and organic superconductors.[5–10] Besides the dramatic locking-unlocking transition, Kes[11] proposed and Theodorakis[12] calculated in detail a model, where four different vortex states are assumed depending on whether the applied field components parallel and perpendicular to the superconducting planes are above or below the respective lower critical fields $H_{c1}^{||}$ and $H_{c1}^{\perp}$. Further calculations[4,11,12] lead to the prediction that the ordinary Abrikosov type vortex lattice transforms first into a lattice of kinked Josephson vortices along the CuO_2 planes, before finally locking in. A comprehensive summary of the theoretical work on this transition and lock-in is given by Blatter *et al.*.[13]

In this article we present systematic measurements of the cuprate superconductor $La_{2-x}Sr_xCuO_4$ using highly sensitive torque magnetometry. Torque measurements are highly sensitive to the transverse magnetization perpendicular to an applied magnetic field and therefore well suited for investigations of anisotropic magnetic properties. Five single crystal samples with different Sr content, covering the under-, optimal, and over-doped region, were investigated at temperatures below T_c and in fields up to 1.5 T. Due to increased irreversibility effects at low temperatures, only measurements within about 5 K below T_c were performed. Clearly visible systematics of the appearance of Josephson vortices and lock-in as a function of field strength, field orientation, and temperature are reported. Thanks to these systematics we can clearly assign the peaks in angle-dependent torque measurements to the Josephson type vortices — on the contrary to previous interpretations, where these were attributed to the lock-in directly. We show that the effective lock-in only occurs in a much narrower angle region.

An important property of layered superconductors is the anisotropy parameter $\gamma = (m_c^*/m_{ab}^*)^{1/2}$, where m_c^* and m_{ab}^* are the effective supercarrier masses for currents flowing along the *c*-axis and in the *ab*-plane, respectively. It turns out that a precise determination of γ is problematic due to the appearance of the Josephson vortices. Here we present a reliable procedure for the extraction of an accurate value of γ from magnetic torque measurements.

II. EXPERIMENTAL DETAILS

Single crystals of $La_{2-x}Sr_xCuO_4$ were grown using the traveling solvent floating zone technique.[14] Underdoped ($x = 0.07$, 0.125), optimally doped ($x = 0.15$), and overdoped ($x = 0.19$, 0.23) single crystal samples were prepared. Microcrystals of about $100 \times 100 \times 50\,\mu m^3$ size were broken from these crystals. Due to their approximate cube shape, the demagnetizing factor $\nu \approx 0.3$ for a

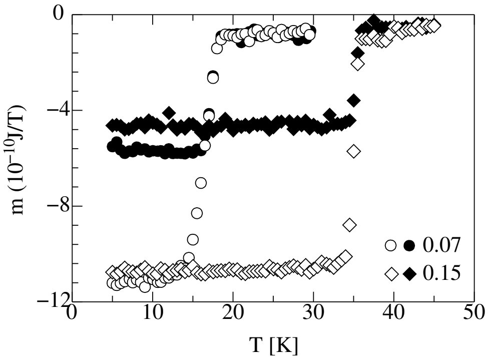

FIG. 1: Magnetization curves of two single-crystal $La_{2-x}Sr_xCuO_4$ samples ($x = 0.07$ and $x = 0.15$) obtained at $\mu_0 H = 1$ mT with the field parallel to the *c*-axis. Closed and open symbols denote measurements obtained in field cooling and zero-field cooling mode, respectively.

sphere was used for calculations where it appears. Low field (1 mT) SQUID measurements in field cooling and zero-field cooling mode were performed to characterize the crystals. The transitions were sharp with transition widths (10–90%) of $\Delta T \approx 0.2$ to 1.0 K and showed Meissner fractions between 20% and 50%, respectively. Typical low-field (1 mT) magnetization measurements of single-crystal $La_{2-x}Sr_xCuO_4$ ($x = 0.07$ and $x = 0.15$) are shown in Fig. 1.

A custom built torquemeter[15] was used to determine the sample's magnetic moment $\mathbf{m}$ from the torque

$$\boldsymbol{\tau} = \mu_0 \mathbf{m} \times \mathbf{H} \qquad (1)$$

it experiences in an external magnetic field $\mathbf{H}$. Torque magnetometry is well suited for investigations of anisotropic magnetic phenomena as found in high temperature superconductors.[5,8,16,17] It is complementary to most other magnetometry techniques in that it is only sensitive to $m_\perp$, the part of $\mathbf{m}$ perpendicular to the applied field, whereas most magnetometers measure the parallel component $m_\parallel$. A torque measurement is fast (one measurement takes only a fraction of a second) and reaches high sensitivities for $m_\perp$ in high fields due to the proportionality $\tau \propto H$. We used capacitive torque sensors[15] with a sensitivity of well below 10^{-12} Nm. The system consists of a flow cryostat between the poles of a rotatable iron yoke magnet ($\mu_0 H_{\max} = 1.5$ T). It is fully computer controlled and allows efficient measurement taking.[18]

At a fixed temperature, magnetic torque measurements $\tau(H, \theta_{\text{fix}})$ were performed at various fixed field orientations θ_{fix} as a function of field magnitude H. Each field scan consisted of torque measurements during continuous increasing (τ_{inc}) and decreasing (τ_{dec}) field sweeps from 0 to 1.5 T. The average $\tau_{\text{rev}} = (\tau_{\text{inc}} + \tau_{\text{dec}})/2$ was then analyzed. Such field scans were performed at roughly 30 different field orientations on each crystal at about six different temperature settings. A complete background measurement well above T_c was taken for each crystal and subtracted from the data prior to analysis.

III. THEORETICAL BACKGROUND

The data were analyzed within the framework of the phase transition approach of Schneider and Singer,[19] where critical thermal fluctuations close to T_c are investigated, leading to universal relations. These critical properties allow the cuprates to be assigned to the 3D-XY universality class.[19] The torque signal below T_c and for small fields then adopts the form[19]

$$\tau = m_0\left(1-\gamma^{-2}\right)\frac{\sin(2\theta)}{\varepsilon_\gamma(\theta)}\mu_0 H \ln\left(\frac{H}{H_0}\varepsilon_\gamma(\theta)\right) \qquad (2)$$

$$\text{with} \qquad m_0 = \frac{-Q_3^- C_{3,0}^- k_B T V}{2\Phi_0 \xi_c^-} \quad , \; H_0 = \frac{\Phi_0}{\mu_0 (\xi_{ab}^-)^2} \qquad (3)$$

$$\text{and} \qquad \varepsilon_\gamma(\theta) = \sqrt{\cos^2\theta + \gamma^{-2}\sin^2\theta}. \qquad (4)$$

Generally, m_0, H_0, and γ are used as fit parameters. Here ξ_c^- and ξ_{ab}^- are the correlation lengths along and perpendicular to the *c*-axis, respectively, and $\gamma = \xi_{ab}^-/\xi_c^-$ is the anisotropy parameter. The $^-$ superscripts indicate, that critical properties upon approaching T_c from below are investigated. V denotes the sample volume, H is the magnetic field magnitude, and θ is the angle it encloses with the sample's *c*-axis. Φ_0 is the magnetic flux quantum and $Q_3^- C_{3,0}^- \approx 0.69$ is a universal constant for the 3D-XY universality class in the limit $T \to T_c$ and $H \to 0$.[20,21] In order for Eq. (2) to be applicable, the scaling variable

$$\mathcal{Z} = \frac{H}{H_0}\varepsilon_\gamma(\theta) \qquad (5)$$

has to be small ($\mathcal{Z} \ll 1$), because for $\mathcal{Z} > 0.32$, magnetic field induced finite size effects[22] become important and cause a modification of the shape of $\tau(H, \theta)$. Equation (2) is found to agree well with measured data, except for angles $\theta \approx 90°$, where deviations are often observed (see Fig. 2(b)). Since torque τ was measured at fixed angle θ as a function of magnetic field H, the form

$$\tau = m_\theta \mu_0 H \ln(H/H_\theta) \qquad (6)$$

of Eq. (2) for a constant angle θ was used to fit the data. Regions of data where this model can be applied are easily identified by the linear dependence of τ_{rev}/H vs $\ln(H)$. The extracted parameters m_θ and H_θ are subsequently fit to their respective angle dependence

$$m_\theta = m_0\left(1-\gamma^{-2}\right)\sin(2\theta)/\varepsilon_\gamma(\theta) \qquad (7)$$

and

$$H_\theta = H_0/\varepsilon_\gamma(\theta) \tag{8}$$

in order to obtain m_0, H_0, and γ.

The specialities due to the layering are not encompassed in this general description. Calculations based on the vortex structure, however, have been used for a long time to describe torque data. Kogan's[23] description of the torque acting on a type-II superconductor for fields $H_{c1} \ll H \ll H_{c2}$ reads as

$$\tau = \frac{VH\Phi_0}{8\pi\lambda_{ab}^2} f_\mathrm{K}(\vartheta) \tag{9}$$

with

$$f_\mathrm{K}(\vartheta) = \left(1-\gamma^{-2}\right) \frac{\sin\vartheta\cos\vartheta}{\varepsilon(\vartheta)} \ln\left(\frac{L\beta}{\xi_c\gamma\sqrt{\varepsilon(\vartheta)}}\right). \tag{10}$$

The angle ϑ is measured between the applied field and the CuO_2 planes and $L = \sqrt{(\Phi_0/B)}$ is the intervortex distance. These results were obtained assuming a lattice of Abrikosov type vortices. We note that the functional dependence of τ on H and θ of Eqs. (2) and (9) is the same. Theodorakis[12] investigated the case, where the flux enters the sample in form of kinked vortices made of Josephson type vortices between the CuO_2 layers interconnected by pancake vortices. His formula for the magnetic torque reads very similarly, replacing $f_\mathrm{K}(\vartheta)$ by

$$\begin{aligned} f_\mathrm{T}(\vartheta) &= \left(1-\gamma^{-2}\right) \frac{\sin\vartheta\cos\vartheta}{\varepsilon(\vartheta)} \ln\left(\frac{L\beta}{d\gamma\sqrt{\varepsilon(\vartheta)}}\right) \\ &\quad + \mathrm{sgn}(\vartheta)\ln\left(\frac{d}{\xi_c}\right) \end{aligned} \tag{11}$$

in Eq. (9) with d being the distance between the CuO_2 layers. The field dependence remains logarithmic with a different slope, though the angle dependence is modified by the additional term. At very small angles $\vartheta < \vartheta_\mathrm{L}$ below the lock-in angle ϑ_L, the vortices lie fully between the CuO_2 layers, the torque becomes independent on specific superconducting parameters and assumes a quadratic field dependence

$$\tau = \vartheta\frac{VH^2\mu_0}{2\nu}, \tag{12}$$

as calculated by Maslov and Pokrovsky.[24] The demagnetizing factor along the applied field direction ν makes comparison with experiments difficult, because it is hard to determine, let alone well defined for arbitrarily shaped samples.

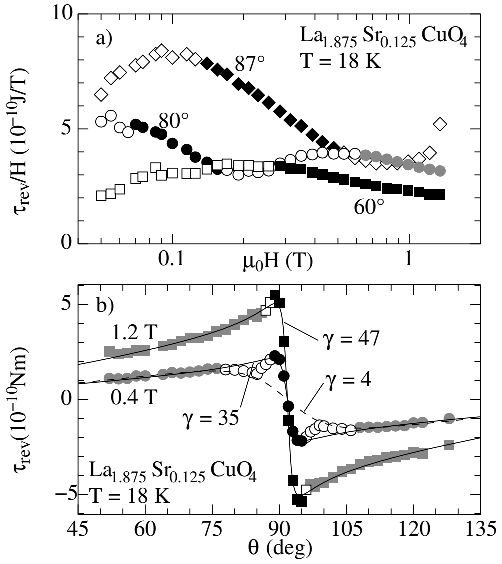

FIG. 2: Torque measurements $\tau_\mathrm{rev}(H, \theta_\mathrm{fix})$ of an underdoped $La_{2-x}Sr_xCuO_4$ ($x = 0.125$) single crystal sample at 18 K. (a) Part of the whole data set ($\theta = 60°$, $80°$, and $87°$) plotted as τ_rev/H vs $\ln H$, revealing linear regions (filled black and gray symbols) according to Eq. (6). Data points belonging to high-field linear regions (ordinary, tilted vortex lattice) are filled gray. Those belonging to low-field linear regions (kinked vortices) are filled black. (b) Another part of the same data set, plotted as τ_rev vs θ for $\mu_0 H = 0.4\,\mathrm{T}$ (circles) and $\mu_0 H = 1.2\,\mathrm{T}$ (squares). The meaning of the symbols is the same as in (a). Curves represent fits to Eq. (2). The strongly differing values obtained for γ illustrate the difficulty of its determination.

IV. RESULTS

Each field dependent measurement $\tau_\mathrm{rev}(H, \theta_\mathrm{fix})$ was investigated separately, regarding the applicability of Eq. (6), by plotting τ_rev/H vs $\ln H$, as shown in Fig. 2(a) for three different angles. Linear regions where Eq. (6) can be fitted are emphasized by gray and black filled symbols. At low angles ($\theta = 60°$) only one such region was found [gray squares in Fig. 2(a)]. However, when θ approaches 90°, a second linear region appears at low fields (filled circles, $\theta = 80°$). This low-field region expands to higher fields very close to 90° (filled diamonds, $\theta = 87°$). Note that the high-field linear region of the $\theta = 87°$ measurement lies above our maximum measurement field of $\mu_0 H = 1.5\,\mathrm{T}$. We emphasize that irreversibility $\tau_\mathrm{inc} - \tau_\mathrm{dec}$ is small in both linear regions. Different measurement conditions which affect the irreversibility did not change the results. Thus, we judge that irreversibility does not influence our results significantly. The points belonging to these high-field and low-field linear regions are easily associated with the smooth angular dependence at small angles and the steep increase close to $\theta = 90°$ in Fig. 2(b), respectively. This steep increase has always been

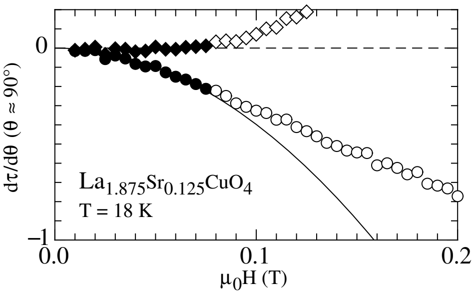

FIG. 3: The slope $\frac{\Delta\tau}{\Delta\theta}$ close to $\theta = 90°$ as determined from measurements on a $\mathrm{La}_{2-x}\mathrm{Sr}_x\mathrm{CuO}_4$ single crystal with $x = 0.125$ as a function of magnetic field H (circles) with a fit to a quadratic function (solid line). The region of quadratic dependence (filled symbols) indicating lock-in is clearly visible in the difference plot (diamonds).

associated with lock-in, but our measurements suggest that it is due to the appearance of kinked vortices. The complete lock-in must therefore be restricted to a much smaller angular regime, identified by a quadratic field dependence. Such a quadratic field dependence can in fact be observed by plotting the slope $\frac{\Delta\tau}{\Delta\theta}(\theta \approx 90°)$ (effectively averaging over a few measured points at different angles) vs. field H, as shown in Fig. 3.

The extents of the different regions observed in our measurements were determined for all measured angles, temperatures and samples, leading to detailed maps in the H_{xy}-H_z planes. Such results are shown in Fig. 4 for an underdoped sample ($x = 0.07$) at 13 K. The observed angle dependence of both the upper limit of the low-field region and the lower limit of the high-field region are well described by the relation

$$H = \frac{H_{\mathrm{L}}}{|\cos\theta|} \tag{13}$$

proposed by Bulaevskii *et al.*.[4] With $H_{\mathrm{L}} = H_J(1-\nu_z)$, this describes the field region below which the tilted vortex lattice cannot exist. Taking $H_{\mathrm{L}} = H_{c1}^{c}(1-\nu_z)$, it is the upper limit for the locked-in vortices. The temperature dependence of the tilted-kinked vortex lattice transition field, as obtained from the lower bound of the high-field and the upper bound of the low-field linear region, is shown for the five differently doped samples in Fig. 5 (closed and open symbols, respectively). The values of the slopes $\alpha = \mu_0 \mathrm{d}H_{\mathrm{L}}/\mathrm{d}T$ of the linear fits to $H_{\mathrm{L}}(T)$ are listed in Table I. They clearly increase with increasing doping, which means that a stronger magnetic field is needed to drive the vortices from the locked-in situation to the free, tilted position in overdoped samples.

The linear regions found in $\tau_{\mathrm{rev}}(H, \theta_{\mathrm{fix}})/H$ vs $\ln H$ for different angles were independently fit to Eq. (6). The

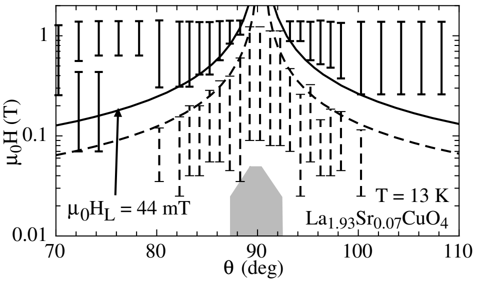

FIG. 4: Graphical representation of the field regions as displayed in Figs. 2(a) and 3 for an underdoped $\mathrm{La}_{2-x}\mathrm{Sr}_x\mathrm{CuO}_4$ ($x = 0.07$) single crystal. The vertical bars illustrate the lower and upper field limit of the linear regions. Dashed bars belong to the kinked phase, whereas solid bars represent the free tilted vortex lattice. The solid and dashed curves are fits of Eq. (13). The two solid bars at 72° and 74° probably belong to the same linear region, because they have very similar slopes $\mathrm{d}(\tau_{rev}/H)/\mathrm{d}(\ln H)$. The gray region around 90° illustrates the occurrence of lock-in.

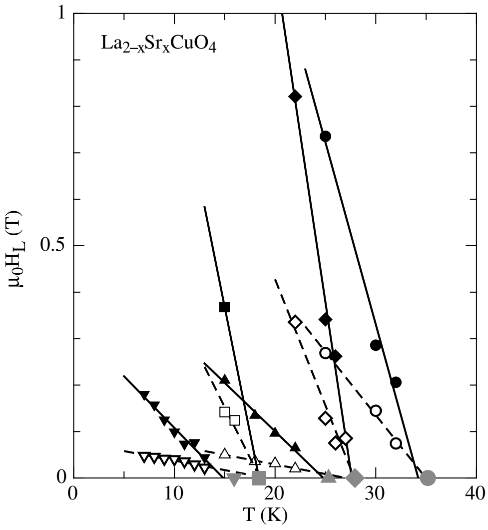

FIG. 5: Lower bound of the high-field linear region (closed symbols) and upper bound of the low-field linear region (open symbols), as obtained for single-crystal $\mathrm{La}_{2-x}\mathrm{Sr}_x\mathrm{CuO}_4$ with various Sr contents x (▽ : $x = 0.07$, △ : $x = 0.125$, ○ : $x = 0.15$, ◇ : $x = 0.19$, □ : $x = 0.23$). The large symbols on the abscissa represent the T_c's obtained as described in the text. Lines are linear fits with slopes $\alpha = \mu_0 \mathrm{d}H_{\mathrm{L}}/\mathrm{d}T$ listed in Table I.

x	T_c (K)	α (mT/K)	T_max (K)	γ
0.070	17.67(19)	-22.2(19)	14.9(5)	73.5(2.0)
0.108	23.83(20)	—	—	37.8(1.0)
0.125	25.31(14)	-20.9(17)	24.8(6)	35.0(1.0)
0.150	35.18(37)	-78(12)	34.2(9)	19.0(1.0)
0.190	27.93(6)	-144(17)	27.6(5)	10.2(1.0)
0.230	18.41(14)	-108[a]	—	10.6(1.0)

[a] slope obtained from one point and T_c only

TABLE I: Summary of some quantities obtained for single-crystal $\mathrm{La}_{2-x}\mathrm{Sr}_x\mathrm{CuO}_4$ samples with various Sr contents x. T_c was obtained from linear extrapolation of m_0 vs T to $m_0 = 0$ (see text). The quantity $\alpha = \mu_0 \mathrm{d}H_\mathrm{L}/\mathrm{d}T$ was obtained from linear fits to H_J vs T displayed in Fig. 5, and T_max is the temperature where the linear fit intersects the abscissa. The values of the anisotropy parameter γ were determined with the procedure described in the text.

resulting fitted parameters H_θ and m_θ of one data set of an underdoped sample ($x = 0.07$) at fixed temperature ($T = 13\,\mathrm{K}$) are shown in Fig. 6 as a function of angle.

In principle, the anisotropy γ may be obtained from fits of Eqs. (7) and (8) to $m_\theta(\theta)$ and $H_\theta(\theta)$, respectively. However, there are difficulties: First of all, close to $\theta = 90^\circ$, points are missing for the tilted vortex lattice which are crucial for a reliable determination of γ due to its strong dependence on $\varepsilon_\gamma(\theta)$ [Eq. (4)] in this angle region. Second, the discrepancy between the γ values obtained from $m_\theta(\theta)$ and $H_\theta(\theta)$, respectively, is very large. It is particularly large for the kinked lattice, for which γ obtained from $H_\theta(\theta)$ diverges. The applicability of Eq. (2) to the kinked phase is therefore questionable. Consequently, physical conclusions drawn from results obtained in the kinked lattice must be treated with care. On the other hand, m_0 and H_0 obtained from fits to $m_\theta(\theta)$ and $H_\theta(\theta)$ of the free, tilted vortex lattice (Fig. 6, filled circles) are largely independent of γ. Thus, for each sample and temperature a parameter set m_0, H_0, and H_J can be obtained. From these, the in-plane and out-of-plane correlation lengths ξ_ab^- and ξ_c^- are determined by Eqs. (3), as shown in Fig. 7 (symbols are the same as in Fig. 5). As expected, the divergence of the correlation lengths upon approaching T_c is observed for the results obtained from the free, tilted vortex lattice. Qualitatively the difference between the tilted and the kinked vortex lattice is more pronounced in underdoped samples. Figure 8 shows the temperature dependence of the scaling variable $\mathcal{Z}$ [Eq. (5)], which must satisfy $\mathcal{Z} \ll 1$ in order to justify the use of Eq. (2). The average $\overline{\mathcal{Z}} = \overline{H}\varepsilon_\gamma(\theta)/H_0$ is shown, where $\overline{H}$ is the average of the field region from which H_0 was obtained by fitting Eq. (6). As is clearly seen, this requirement is fulfilled for all measurements, except for temperatures very close to T_c. The critical value $\mathcal{Z} \approx 0.3$, where magnetic field induced finite size effects are expected to set in,[22] is shown as well.

As stated in the introduction, the occurrence of kinked vortices inhibits a reliable determination of the anisotropy parameter γ. It may also cause a spurious field dependence, when angle dependent measurements $\tau_\mathrm{rev}(H, \theta_\mathrm{fix})$, taken at different fields and fitted with Eq. (2), are compared. The temperature dependence of H_L clearly shows that kinked vortices appear up to temperatures close to T_c (see Fig. 5). Therefore, for a reliable determination of γ, only measurements close to T_c and in high fields should be considered. For this reason we fitted Eq. (2) to the angle dependence at constant field $\tau_\mathrm{rev}(H = \mathrm{const.}, \theta)$. The resulting field dependent $\gamma(H)$ was averaged over the high-field region, where it is field-independent. At low fields, however, some field dependence of γ is always observed. The resulting anisotropies γ obtained for the single-crystal samples investigated here are shown in Fig. 9 and listed in Table I. The critical temperatures T_c shown in Figs. 5 and 9 and listed in Table I were obtained from linear extrapolations of $m_0(T)$,

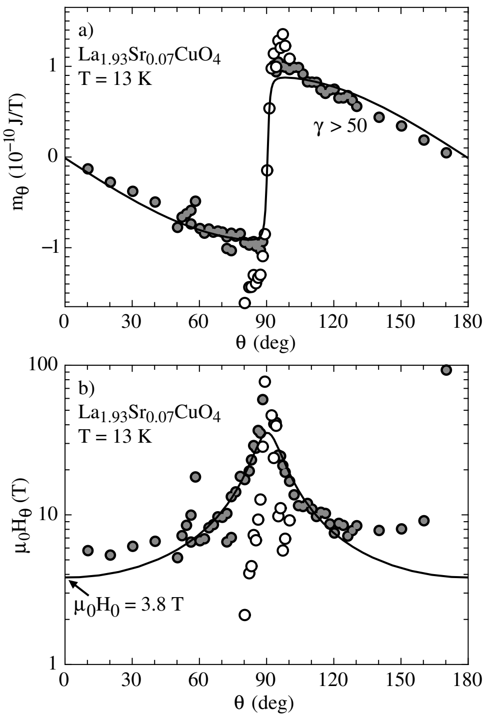

FIG. 6: The fit parameters m_θ (a) and H_θ (b) as determined for a $\mathrm{La}_{1.93}\mathrm{Sr}_{0.07}\mathrm{CuO}_4$ single crystal at 13 K as a function of the angle θ. Closed and open circles correspond to results from field regions of the tilted and the kinked vortex lattice, respectively. Curves in (a) and (b) are fits of Eqs. (7) and (8), respectively.

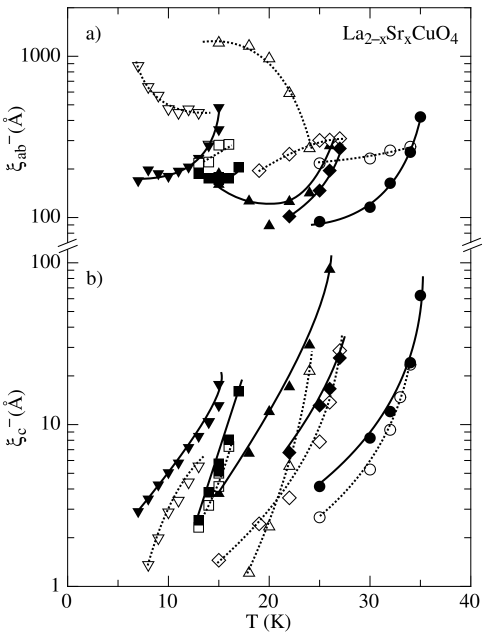

FIG. 7: (a) In-plane ($\xi_{\rm ab}^-$) and (b) out-of-plane ($\xi_{\rm c}^-$) correlation lengths as determined from m_0 and H_0 using Eq. (3) for single-crystals of $La_{2-x}Sr_xCuO_4$ for various dopings x ($\bigtriangledown : x = 0.07$, $\triangle : x = 0.125$, $\bigcirc : x = 0.15$, $\diamond : x = 0.19$, $\square : x = 0.23$). Filled and open symbols are obtained from measurements of the tilted and the kinked vortex lattice, respectively. Since the applicability of Eq. (2) is questionable for the locked-in lattice, the interpretation of the open symbols is not clear. Curves are guides to the eye.

which is linear within error bars close to T_c. The doping dependence of T_c and γ follows approximately the empirical models proposed in Refs. 25–29. However, we observe a general shift of the T_c-dome toward lower doping x and a generally lower T_c. The latter can be attributed to the fact that single crystals usually exhibit lower T_c's than powder samples. The lower T_c of the samples with nominal compositions $x = 0.108$ and $x = 0.125$ is in accordance with the dip of T_c observed close to $x = 1/8$.[31] Our values of the anisotropy parameter γ for these samples lie above the general trend of the other samples (see Fig. 9). Both deviations may be interpreted such that the effective doping of these samples is considerably lower ($x \approx 0.09$). Plotted as T_c vs $1/\gamma$, all points fall on the universal parabola found for various cuprates.[30]

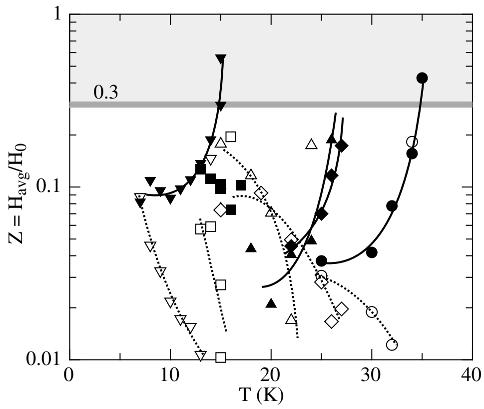

FIG. 8: Temperature dependence of the average scaling variable $\mathcal{Z}$ for single crystal samples of $La_{2-x}Sr_xCuO_4$ for various Sr contents x. Symbols are the same as in Figs. 5 and 7. It is evident that Eq. (2) is valid over the whole temperature range, except for $T \lesssim T_c$ ($\mathcal{Z} \gtrsim 0.3$, gray region), where field induced finite size effects are expected to set in.[22]

V. SUMMARY

The appearance of kinked vortices and the lock-in effect in the layered superconductor $La_{2-x}Sr_xCuO_4$ was studied extensively by means of torque magnetometry. Our measurements allowed us to identify the characteristic peaks of torque close to the CuO_2 planes with the appearance of kinked vortices — contrarily to previous measurements which assigned them to the lock-in effect. In particular the influence of these vortex configurations on the determination of the anisotropy parameter γ was investigated. Kinked vortices appear nearly up to the critical temperature T_c and can only be avoided in large magnetic fields. Thus, γ must be determined close to T_c in a field as large as possible. Values of the anisotropy parameter γ obtained this way show that it increases with decreasing doping x, indicating that the system becomes quasi 2-dimensional in the underdoped limit.[27,28] Even though the determination and interpretation of the correlation lengths $\xi_{\rm ab,c}^-$ of the kinked phase is questionable, their difference to the $\xi_{\rm ab,c}^-$ of the free vortex lattice can be regarded as a measure of how large the qualitative difference between the two phases is. As expected, we observe that the qualitative difference between the two phases becomes more pronounced toward the 2D limit in the underdoped regime. However, the magnetic field needed to drive the kinked lattice to its free, tilted orientation decreases toward this 2D limit, implying that the tendency to form kinked vortices is weakened as the system becomes quasi 2-dimensional. The agreement with other measurements of the anisotropy γ shows that the procedure presented in this article is well suited for the determination of γ from magnetic properties.

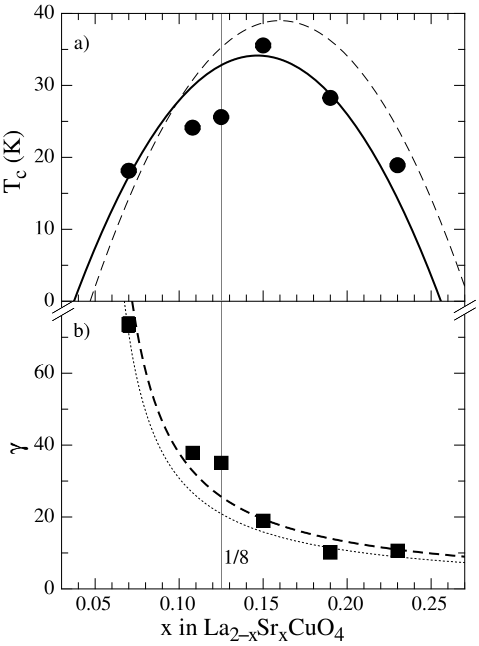

FIG. 9: T_c (a) and anisotropy parameter γ (b) of $La_{2-x}Sr_xCuO_4$ single crystals as a function of doping x, determined as described in the main text. (a) The solid parabola is a guide to the eye. The dashed parabola serves as a comparison to the data shown in Fig. 1 of Ref. 30. (b) Both the dashed and the dotted curves are the ones shown in Fig. 1 of Ref. 30. The considerably lower T_c and higher γ of the two underdoped samples with nominal concentrations $x = 0.108$ and $x = 0.125$ could be interpreted by a lower effective doping of $x \approx 0.09$.

VI. ACKNOWLEDGMENT

This work was partly supported by the Swiss National Science Foundation.

---

[*] current e-mail address: `kohout@physik.unizh.ch`

[1] W. E. Lawrence and S. Doniach, Proceedings of the 12th International Conference on Low Temperature Physics p. 361 (1972).

[2] M. Tachiki and S. Takahashi, Solid State Comm. **70**, 291 (1989).

[3] D. Feinberg and C. Villard, Phys. Rev. Lett. **65**, 919 (1990).

[4] L. N. Bulaevskii, M. Ledvij, and V. G. Kogan, Phys. Rev. B **46**, 366 (1992).

[5] D. E. Farrell, J. P. Rice, D. M. Ginsberg, and J. Z. Liu, Phys. Rev. Lett. **64**, 1573 (1990).

[6] S. Kawamata, N. Itoh, K. Okuda, T. Mochiku, and K. Kadowaki, Physica C Superconductivity **195**, 103 (1992).

[7] F. Steinmeyer, R. Kleiner, P. Müller, and K. Winzer, Physica B Condensed Matter **194**, 2401 (1994).

[8] D. Zech, C. Rossel, L. Lesne, H. Keller, S. L. Lee, and J. Karpinski, Phys. Rev. B **54**, 12535 (1996).

[9] M. A. Avila, L. Civale, A. V. Silhanek, R. A. Ribeiro, O. F. de Lima, and H. Lanza, Phys. Rev. B **64**, 144502 (2001).

[10] K. Takahashi, T. Atsumi, N. Yamamoto, M. Xu, H. Kitazawa, and T. Ishida, Phys. Rev. B **66**, 012501 (2002).

[11] P. H. Kes, J. Aarts, V. M. Vinokur, and C. J. van der Beek, Phys. Rev. Lett. **64**, 1063 (1990).

[12] S. Theodorakis, Phys. Rev. B **42**, 10172 (1990).

[13] G. Blatter, M. V. Feigel'man, V. B. Geshkenbein, A. I. Larkin, and V. M. Vinokur, Rev. Mod. Phys. **66**, 1125 (1994).

[14] T. Sasagawa, K. Kishio, Y. Togawa, J. Shimoyama, and K. Kitazawa, Phys. Rev. Lett. **80**, 4297 (1998).

[15] C. Rossel, M. Willemin, A. Gasser, H. Bothuizen, G. I. Meijer, and H. Keller, Rev. Sci. Instrum. **69**, 3199 (1998).

[16] J. C. Martinez, S. H. Brongersma, A. Koshelev, B. Ivlev,

P. H. Kes, R. P. Griessen, D. G. de Groot, Z. Tarnavski, and A. A. Menovsky, Phys. Rev. Lett. **69**, 2276 (1992).

[17] M. Willemin, C. Rossel, J. Hofer, H. Keller, Z. F. Ren, and J. H. Wang, Phys. Rev. B **57**, 6137 (1998).

[18] S. Kohout, J. Roos, and H. Keller, Meas. Sci. Technol. **16**, 2240 (2005).

[19] T. Schneider and J. M. Singer, *Phase Transition Approach to High Temperature Superconductivity* (Imperial College Press, London, 2000).

[20] J. Hofer, T. Schneider, J. M. Singer, M. Willemin, H. Keller, C. Rossel, and J. Karpinski, Phys. Rev. B **60**, 1332 (1999).

[21] J. Hofer, T. Schneider, J. M. Singer, M. Willemin, H. Keller, T. Sasagawa, K. Kishio, K. Conder, and J. Karpinski, Phys. Rev. B **62**, 631 (2000).

[22] T. Schneider, J. Supercond. **17**, 41 (2004).

[23] V. G. Kogan, Phys. Rev. B **38**, 7049 (1988).

[24] S. S. Maslov and V. L. Pokrovsky, Europhys. Lett. **14**, 591 (1991).

[25] M. R. Presland, J. L. Tallon, R. G. Buckley, R. S. Liu, and N. E. Flower, Physica C **176**, 95 (1991).

[26] J. L. Tallon, C. Bernhard, H. Shaked, R. L. Hitterman, and J. D. Jorgensen, Phys. Rev. B **51**, R12911 (1995).

[27] T. Schneider and H. Keller, Phys. Rev. Lett. **86**, 4899 (2001).

[28] T. Schneider, Physica B **326**, 289 (2003).

[29] T. Schneider, in *The Physics of Superconductors*, edited by K. Bennemann and J. B. Ketterson (Springer, Berlin, 2004), p. 111.

[30] T. Schneider, phys. stat. sol. (b) **242**, 58 (2005), and references therein.

[31] P. G. Radaelli, D. G. Hinks, A. W. Mitchell, B. A. Hunter, J. L. Wagner, B. Dabrowski, K. G. Vandervoort, H. K. Viswanathan, and J. D. Jorgensen, Phys. Rev. B **49**, 4163 (1994).

Chapter 6

Discussion and outlook

Clearly, this work's main result was the establishment of a new, reliable source of sensors for torque magnetometry, both capacitive and piezoresistive. After the developments of D. Zech and M. Willemin in the group of H. Keller in collaboration with C. Rossel from the IBM Zurich Research Laboratory, the Zurich group now has the entire knowledge for creating new sensors. The whole design process is done in the group. The fabrication is performed by a private company, making the obtaining of new sensors very reliable. The mounting of the sensors can again be done at the University. The new square design of torque sensors with a high sensitivity and versatility has proved to work well. A further fabrication run will be needed to obtain the two-axis torque sensors proposed in this thesis, should the need for two-axis measurements arise.

Even though the piezoresistive and the capacitive torque readout techniques are nearly equally sensitive, their application fields are quite different. The capacitive sensors are comparably robust and offer enough space to accommodate large samples. Unfortunately, stray capacities to the cryostat walls make the sensors very sensitive to the position inside the cryostat. Consequently, the relation between the measured signal and the applied torque changes after each warm-up and cool-down of the cryostat. This makes this readout technique unfavorable for experiments with high demands on reproducibility. The piezoresistive sensors, on the other hand, can be calibrated very easily, even *in situ* with a mounted sample. Furthermore, they are inherently highly reproducible, which makes them the prime choice for isotope effect experiments. However, due to their fragility, they are not suited for large samples.

The availability of high performance piezoresistive torque sensors now make it possible to conduct isotope-effect experiments with torque magnetometry. In the group of H. Keller, which has specialized in isotope-effect experiments, J. Hofer started with such measurements on underdoped $La_{2-x}Sr_xCuO_4$ single crystals [HCS+00]. The desirable extension into the overdoped regime now becomes possible and will certainly be taken up. The overdoped region is relatively little explored so far. Such measurements are therefore very likely to shed more light on the high-temperature superconductivity puzzle. Thanks to the automation facilities built into the measurement setup, comparable measurements are easier to perform now. A once saved measurement program can be used several times after each isotope-exchange treatment of the sample. This ensures identical measuring conditions and consequently easily comparable data.

The automation facilities also enable the conduction of long measurement series. Both the measurement over large regions in phase space or the very fine measurement of selected portions of it can easily be programmed and carried out. The former allows the determination of systematic effects, such as demonstrated in section 5.1 on the example of the vortex transformations in $La_{2-x}Sr_xCuO_4$ across the whole doping regime. The latter is very useful for investigations of critical phenomena close to phase transitions. Such a work is currently being performed on the recently discovered two-band superconductor MgB_2.

Appendix A

Command system

Knowledge of the commands exchanged between the VIs is not needed for the operation of the torque software system. However, for completeness and to provide an overview of the system for users intending to develop the system, a more detailed account of the command system is given in this appendix.

All commands consist of an instruction and an argument, separated by an equal (=) sign. An example is the "setpoint=20" command in the handlerLakeshore.vi VI, which is used to set a new temperature (handlerLakeshore.vi is the handler.vi VI for the Lakeshore temperature controller).

Before execution, the command is divided into these two parts. The instruction is wired to the selector of the main case structure present in every VI. The argument is present within the case structure as well and handled accordingly depending on the command. Some commands do not require any argument, they just ignore it. Others divide the argument further in order to get the needed information.

A.1 torque.vi commands

As already mentioned in section 3.1.5, the torque.vi main program is divided into two parts. One of them is checking for user interaction (GUI) and the other (CP) performs the actual tasks associated with changing the measurement parameters, taking measurements and processing data.

The following basic operation modes are distinguished:

Parameter setting Measurement parameters are set. These include the system temperature, the magnetic field strength and direction as well as extensive Lock-In Amplifier settings. Selections for different scan measurements are also made by presetting several values like lower and upper boundary of the scan and choosing the parameter to be scanned.

Speed and step distance can be chosen as well as the direction of the scan.

Scan measurements When a scan is started, the system automatically forces the scan parameter outside the first boundary or waits for the user to do this. Then the scan parameter is increased or decreased according to the chosen settings while measurements are taken continuously.

Postprocessing data After a scan is finished, some basic postprocessing can be performed on the data, like subtracting background drifts or reordering the data for easier analysis.

Saving and printing The continuous data log, the scan measurement or the postprocessed data can be printed or saved to disk after selecting the channels of interest.

The CP's data needed for execution include the following main structures:

Parameters contains local copies of the current measurement parameters including the setpoints chosen by the user.

Pretrigger contains the set of most recent measurements received from the dataserver.vi, usually during the last few seconds.

Log In regular intervals, a measurement is copied onto the end of this structure. It helps to track the status of the measurement system concerning temperature and measurement stability.

Scan measurement contains the raw data of a scan measurement

Postprocessed data is filled with a copy of the scan measurement data after having been processed.

Scan metadata contains data about the scan measurement which is not saved in the scan itself (like Lock-In Amplifier parameters).

Because the functionality is so broad and complex the commands are further structured in CP. Most commands consist of a main and a subcommand, sometimes they feature even more subcommand layers. In the stack they are just separated by spaces. An example is the "doscan start checkout" command which is executed before a parameter sweep to check if the parameter currently lies outside the range which is to be scanned. In case it is not, the "doscan start goOut" command is executed which tries to move the parameter to its initial position.

The main case structure comprises the following main cases:

initializeRegisters is executed only for the very first time the program is started and initializes the internal data containers to reasonable default values. A command is also sent to the dataserver.vi instructing it about what measurement data to send back regularly.

GetCommand [subcommand] checks the queue and attaches these commands to the set of commands needed to be run automatically. If needed, the exit command is executed here as well.

sequence [subcommand] performs a set of tasks needed for automated measurement taking. It is described in more detail below.

getMsrmts obtains the most recent measurement from the DataSocket server and appends it to the internal cache (called pretrigger) of the most recent measurements.

stability checks how far the measurement parameters are off from their desired values and if they are stable enough.

doscan [subcommand] is used to start, stop and control scan measurements.

postprocess [subcommand] contains several subcommands which are used to alter the internally stored data. These functions are described later in more detail.

shortenpretrigger removes measurement data from the pretrigger which is not needed anymore, either because it is too old or because it was already saved into the scan measurement.

setparameters [subcommand] is used to alter measurement parameters (temperature and magnet control and Lock-In Amplifier settings).

setscan [subcommand] is similar to setparameters, but alters the setup of measurement scans.

archive [subcommand] performs tasks associated with printing and saving measurements to disk.

plot [subcommand] contains commands used for selecting the data set and channels to be plotted and the plotting itself.

In order to enable automatic measurement taking the command set of torque.vi had to be extended by a set of waiting commands which are not needed for the interactive use. These commands are incorporated into the torque.vi's main `sequence` command as subcommands (e.g. `sequence waitfield`).

waitfield, waitangle, waittemp are used to wait for a measurement parameter to either become stable and/or enter a specified range.

wait N is used to wait for a specified time. N is a number with unit (e.g. 1h, 15min or 30s).

waitfortorqueNT is used to specify waiting for a scan measurement to be finished.

Whenever sequencer.vi sends such a command to torque.vi, it appends a special ID, based on the current time. After the waiting condition is fulfilled, torque.vi sends a notice to sequencer.vi, again including this ID. The sequencer.vi only continues the execution of the sequence when the same ID is returned. Other ID's might be left overs from older waiting instructions which were ignored for some reason (e.g. if the user hit the continue button).

A.2 dataserver.vi commands

The dataserver.vi employs the following commands.

readall Collects data from instruments and publishes them all together. The definition about which data to collect is received in this command as well.

status regularly sends the status command to the handler VIs to update their status and reads this status data from the instruments.

exit contains only the exit questioner

docommand checks the queue for new commands and sends them on to the handler.vi VIs.

A.3 handler.vi VIs commands

Especially all the handler.vi VIs are very similar and therefore share a common set of commands. These include

GetCommand checks the queue for newly received commands and the instruments SRQ for possible service requests. In any case, it fills the stack with the default command sequence (like reading the instrument's data and sending it to the DataSocket server).

remote puts the instrument in the remote state.

local puts the instrument in the local state.

reset performs a GPIB reset on the instrument interface.

exit smoothly stops execution after putting the instrument into the local state.

status forces the VI to publish its status to the DataSocket.

setwait=N sets the wait time to N milliseconds. This gives the other VIs time to execute in parallel. By changing it to different values, the priorities of execution can be influenced to some degree. Lower wait times cause higher priorities.

publish keeps track of the last few data points, calculates their drift tendency and sends the most recent data point to the DataSocket.

drifttime=N changes the time used by the publish command. Only data younger than N seconds is kept and used for the drift calculation.

This basic set of commands is extended by device specific commands in each handler.vi VI. They are now described in more detail.

A.3.1 handlerEGG7265.vi

readxy reads the x (in phase) and y (quadrature) channels.

SRQ=N handles the service requests. N holds information about the received service request.

Sensitivity=N sets the sensitivity range. N can be a valid index according to the instruments manual or a number with unit (as 10mV).

Phase=N sets the reference phase to a fixed value. N is a number in degrees.

Autophase performs an autophase operation. The lock-in amplifier sets the Phase in order to null the y output.

timeconst=N sets the averaging time constant. N can be a valid index according to the instruments manual or a number with unit (as 100us for 100 µs)

DACn=N sets the DAC output value for channel $n = 1 \dots 4$ (N is a number in volts)

ADCn read out ADC channel n

setflow$=N$ set new coolant flow to $N = 20\dots200$, units are the same as the flow controller's display indicator.

Flow reads the current coolant flow. The flow controller is attached to ADC2, therefore this command is identical to ADC2. In addition, the value received is converted to flow units.

BYTE$=N$ sets the eight lines of the digital output to N. The bits of N define the state of each line.

motor$=N$ set the motor speed ($N = -100\dots100$). A setting to the maximum results in a speed of about 10 °/min.

shaking$=$[on|off|N] sets a new shaking frequency. This effect depends on the basic setting of the Wavetek oscillator. Values $N < 1$ ($N > 1$) result in a lower (higher) frequency.

A.3.2 handlerLakeshore.vi

readcontrol reads the control temperature sensor

readsample reads the sample temperature sensor

readtemps reads both temperature sensors

readparameters reads a set of additional parameters associated with temperature regulation such as PID parameters and heater settings.

setpoint$=T$ Sets a new temperature in Kelvin.

sweep$=S>T$ approaches temperature T at a constant speed of S K/min.

heaterpower$=N$ sets the heater power to the fixed value N %.

heaterrange$=N$ sets the heater power range. N can be either the label or the index of the corresponding button on the controller's front panel ($N = 2$ is equivalent to $N = -3$).

A.3.3 handlerBruker.vi

Because the field is stabilized by the field controller it is not needed to repeatedly query the current field if no field changes were initiated. Therefore the handler.vi works in three different modes. If update=0, it does not read the field. If update=1 the field is read repeatedly until it becomes stable. update=2 forces it to update forever. The GetCommand command sets the stack accordingly.

readField reads the field

setField=N sets new field to N Oe and change to update=1

setHmin=N sets the minimum field for sweep to N

setHmax=N sets the maximum field for sweep to N

sweep=N starts a sweep with indicated speed N

checkoverload checks for the overload condition and adapts update state.

A.3.4 handlerAngle.vi

There are only few commands in this handler.vi, described in the following list.

readangle Reads the angle

calcdrift calculates the drift and publishes the measurement.

setpoint=A@S Moves to a new angle A at S °/min. After being issued by the user, this command keeps itself alive as long as necessary by attaching itself to the end of the command stack.

Publication list

Anisotropic properties of MgB_2 by torque magnetometry
M. Angst, D. Di Castro, R. Puzniak, A. Wisniewski, J. Jun, S.M. Kazakov, J. Karpinski, S. Kohout, and H. Keller
Physica C **408-410**, 88–89 (2004)

Anisotropy and internal-field distribution of MgB2 in the mixed state at low temperatures
M. Angst, D. Di Castro, D.G. Eshchenko, R. Khasanov, S. Kohout, I.M. Savić, A. Shengelaya, S.L. Bud'ko, P.C. Canfield, J. Jun, J. Karpinski, S.M. Kazakov, R.A. Ribeiro and H. Keller
Phys. Rev. B **70**, 224513 (2004)

Automated operation of a homemade torque magnetometer using LabVIEW
S. Kohout, J. Roos and H. Keller
Meas. Sci. Technol. **16** (2005) 2240–2246

Novel sensor design for torque magnetometry
S. Kohout, J. Roos and H. Keller
submitted to Rev. Sci. Instrum.

Study of the Vortex States and Magnetic Anisotropy in Single Crystal $La_{2-x}Sr_xCuO_4$ by Means of Torque Magnetometry
S. Kohout, T. Schneider, T. Sasagawa, J. Roos, H. Takagi, and H. Keller
submitted to Phys. Rev. B

Bibliography

[Abr57] A.A. Abrikosov. On the magnetic properties of superconductors of the second type. Sov. Phys.—JETP **5** 1174 (1957).

[ACS+01] M.A. Avila, L. Civale, A.V. Silhanek, R.A. Ribeiro, O.F. de Lima, and H. Lanza. Irreversible magnetization under rotating fields and lock-in effect on a $ErBa_2Cu_3O_{7-\delta}$ single crystal with columnar defects. Phys. Rev. B **64** 14450 (2001).

[Api] `http://www.apiezon.com/grease.htm`.

[aut] `http://www.autodesk.com/autocadlt`.

[BCS57] J. Bardeen, L.N. Cooper, and J.R. Schrieffer. Theory of superconductivity. Phys. Rev. **108** 1175 (1957).

[BFG+94] G. Blatter, M.V. Feigel'man, V.B. Geshkenbein, A.I. Larkin, and V.M. Vinokur. Vortices in high-temperature superconductors. Rev. Mod. Phys. **66** 1125 (1994).

[ble] `http://www.blender3d.com/`.

[BLK92] L.N. Bulaevskii, M. Ledvij, and V.G. Kogan. Vortices in layered superconductors with Josephson coupling. Phys. Rev. B **46** 366 (1992).

[BM86] J.G. Bednorz and K.A. Müller. Possible superconductivity in $LaBaCuO_4$. Z. Phys. B **64** 189 (1986).

[CDG95] S.J. Chapman, Q. Du, and M.D. Gunzburger. On the Lawrence-Doniach and anisotropic Ginzburg-Landau models for layered superconductors. SIAM J. Appl. Math. **55** 156 (1995).

[CGC+93] C.W. Chu, L. Gao, F. Chen, Z.J. Huang, R.L. Meng, and Y. Xue. Superconductivity above 150 K in $HgBa_2Ca_2Cu_3O_{8+\delta}$ at high pressures. Nature **365** 323 (1993).

[CHJ97] Z. Chen, K.-H. Hoffmann, and L. Jiang. On the Lawrence-Doniach model for layered superconductors. Euro. J. Appl. Math. **8** 369 (1997).

[DCS+95] P. Dai, B.C. Chakoumakos, G.F. Sun, K.W. Wong, D.F. Lu, and Y. Xin. Synthesis and neutron powder diffraction study of the superconductor $HgBa_2Ca_2Cu_3O_{8+\delta}$ by Tl substitution. Physica C **243** 201 (1995).

[dG65] P. de Gennes. *Superconductivity of Metals and Alloys.* Addison-Wesley, (1965).

[FRGL90] D.E. Farrell, J.P. Rice, D.M. Ginsberg, and J.Z. Liu. Experimental evidence of a dimensional crossover in $Y_1Ba_2Cu_3O_{7-\delta}$. Phys. Rev. Lett. **64** 1573 (1990).

[FV90] D. Feinberg and C. Villard. Intrinsic pinning and lock-in transition of flux lines in layered type-II superconductors. Phys. Rev. Lett. **65** 919 (1990).

[GL50] V.L. Ginzburg and L.D. Landau. On the theory of superconductivity. Zh. Eksperim. i Teor. Fiz. **20** 1064 (1950).

[HC91] Z. Hao and J.R. Clem. Reversible magnetization and torques in anisotropic high-κ type-II superconductors. Phys. Rev. B **43** 7622 (1991).

[HCS+00] J. Hofer, K. Conder, T. Sasagawa, Guo meng Zhao, M. Willemin, H. Keller, and K. Kishio. Oxygen-isotope effect on the in-plane penetration depth in underdoped $La_{2-x}Sr_xCuO_4$ single crystals. Phys. Rev. Lett. **84** 4192 (2000).

[Hof96] J. Hofer. Entwicklung eines miniaturisierten Drehmomentmagnetometers, Drehmomentmagnetisierungsmessungen an einem $HgBa_2Ca_3Cu_4O_{10+\delta}$ Mikrokristall. Master's thesis, Universität Zürich, Jan 1996.

[Hof00] J. Hofer. *Studies of Intrinsic Magnetic Properties of High Temperature Superconductors by Means of Torque Magnetometry.* PhD thesis, Universität Zürich, (2000).

[IR78] A.C. Rose Innes and E.H. Rhoderick. *Introduction to Superconductivity.* Pergamon, Oxford, 2nd edition, (1978).

[Joh97] D.C. Johnston. Normal-state magnetic properties of single-layer cuprate high-temperature superconductors and related materials. In K. H. J. Buschow, editor, *Handbook of Magnetic Materials*, volume 10, pages 1–237. Elsevier, Amsterdam, (1997).

[KC81] V.G. Kogan and J.R. Clem. Uniaxial type-II superconductors near the upper critical field. Phys. Rev. B **24** 2497 (1981).

[KFM88] V.G. Kogan, M.M. Fang, and S. Mitra. Reversible magnetization of high-T_c materials in intermediate fields. Phys. Rev. B **38** 11958 (1988).

[KIO+92] S. Kawamata, N. Itoh, K. Okuda, T. Mochiku, and K. Kadowaki. Observation of anisotropic pinning effect in $Bi_2Sr_2CaCu_2O_{8+\delta}$ single crystals. Physica C **195** 103 (1992).

[Kog81] V.G. Kogan. London approach to anisotropic type-II superconductors. Phys. Rev. B **24** 1572 (1981).

[Kog88] V.G. Kogan. Uniaxial superconducting particle in intermediate magnetic fields. Phys. Rev. B **38** 7049 (1988).

[Lab] `http://www.ni.com/labview/`.

[LD72] W.E. Lawrence and S. Doniach. Theory of layer structure superconductors. In *Proceedings of the 12th International Conference on Low Temperature Physics*, page 361, (1972).

[LL35] F. London and H. London. The electromagnetic equations of the supraconductor. Proc. Roy. Soc. **A149** 71 (1935).

[MO33] W. Meissner and R. Ochsenfeld. Ein neuer Effekt bei Eintritt der Supraleitfähigkeit. Naturwissenschaften **21** 787 (1933).

[MP91] S. S. Maslov and V. L. Pokrovsky. The first critical field and locking-unlocking phase transition in layered superconductors. Europhys. Lett. **14** 591 (1991).

[MTK+90] K. Miyashita, T. Takahashi, S. Kawamata, S. Morinaga, and Y. Hoshi. Non-contact magnetic torque sensor. IEEE Trans. Magn. **26** 1560 (1990).

[NNM+01] J. Nagamatsu, N. Nakagawa, T. Muranaka, Y. Zenitani, and J. Akimitsu. Superconductivity at 39K in magnesium diboride. Nature **410** 63 (2001).

[NU93] Y. Nakamura and S. Uchida. Anisotropic transport properties of single-crystal $La_{2-x}Sr_xCuO_4$: Evidence for the dimensional crossover. Phys. Rev. B **47** 8369 (1993).

[Onn11] H. Kamerlingh Onnes. The resistance of pure mercury at helium temperatures. Comm. Phys. Lab. Univ. Leiden **120b, 122b, 124c** (1911).

[PTB+91] M.R. Presland, J.L. Tallon, R.G. Buckley, R.S. Liu, and N.E. Flower. General trends in oxygen stoichiometry effects on T_c in Bi and Tl superconductors. Physica C **176** 95 (1991).

[RBZ+96] C. Rossel, P. Bauer, D. Zech, J. Hofer, M. Willemin, and H. Keller. Active microlevers as miniature torque magnetometers. J. Appl. Phys. **79** 8166 (1996).

[RHM+94] P.G. Radaelli, D.G. Hinks, A.W. Mitchell, B.A. Hunter, J.L. Wagner, B. Dabrowski, K.G. Vandervoort, H.K. Viswanathan, and J.D. Jorgensen. Structural and superconducting properties of $La_{2-x}Sr_xCuO_4$ as a function of sr content. Phys. Rev. B **49** 4163 (1994).

[RWG+98] C. Rossel, M. Willemin, A. Gasser, H. Bothuizen, G.I. Meijer, and H. Keller. Torsion cantilever as magnetic torque sensor. Rev. Sci. Instrum. **69** 3199 (1998).

[SBL70] F. Sass, Ch. Bouché, and A. Leitner, editors. *Dubbel / Taschenbuch für den Maschinenbau*, page 410. Berlin: Springer, 13 edition, (1970).

[SCGO93] A. Schilling, M. Cantoni, J.D. Guo, and H.R. Ott. Superconductivity above 130 K in the HgBaCaCuO system. Nature **363** 56 (1993).

[Sch97] T. Schneider. Universal critical quantum properties of cuprate superconductors. Acta Phys. Pol. A **91** 203 (1997).

[Sch03] T. Schneider. Universal properties of cuprate superconductors. Physica B **326** 289 (2003).

[Sch04] T. Schneider. Universal properties of cuprate superconductors: Evidence and implications. In K.H. Bennemann and J.B. Ketterson, editors, *The Physics of Superconductors*, volume II, page 111. Springer, Berlin, (2004).

[Sch05] T. Schneider. Relationship between and implications of the isotope and pressure effects on transition temperature, penetration depth and conductivities. phys. stat. sol. (b) **242** 58 (2005).

[SH91] M. Suzuki and M. Hikita. Resistive transition, magnetoresistance, and anisotropy in $La_{2-x}Sr_xCuO_4$ single-crystal thin films. Phys. Rev. B **44** 249 (1991).

[SKMW94] F. Steinmeyer, R. Kleiner, P. Müller, and K. Winzer. Lock-in transition in layered superconductors. Physica B **194** 2401 February 1994.

[SKT+98] T. Sasagawa, K. Kishio, Y. Togawa, J. Shimoyama, and K. Kitazawa. First-order vortex-lattice phase transition in $(La_{1-x}Sr_x)_2CuO_4$ single crystals: Universal scaling of the transition lines in high-temperature superconductors. Phys. Rev. Lett. **80** 4297 (1998).

[Smi54] C.S. Smith. Piezoresistance effect in germanium and silicon. Phys. Rev. **94** 42 (1954).

[SS00] T. Schneider and J.M. Singer. *Phase Transition Approach to High Temperature Superconductivity.* Imperial College Press, London, (2000).

[STS+00] T. Sasagawa, Y. Togawa, J. Shimoyama, A. Kapitulnik, K. Kitazawa, and K. Kishio. Magnetization and resistivity measurements of the first-order vortex phase transition in $(La_{1-x}Sr_x)_2CuO_4$. Phys. Rev. B **61** 1610 (2000).

[TAY+02] K. Takahashi, T. Atsumi, N. Yamamoto, M. Xu, and H. Kitazawa. Superconducting anisotropy and evidence for intrinsic pinning in single crystalline MgB_2. Phys. Rev. B **66** 012501 (2002).

[TBS+95] J.L. Tallon, C. Bernhard, H. Shaked, R.L. Hitterman, and J.D. Jorgensen. Generic superconducting phase behavior in high-T_c cuprates: T_c variation with hole concentration in $YBa_2Cu_3O_{7-\delta}$. Phys. Rev. B **51** 12911 (1995).

[TII+89] H. Takagi, T. Ido, S. Ishibashi, M. Uota, S. Uchida, and Y. Tokura. Superconductor-to-nonsuperconductor transition in $(La_{1-x}Sr_x)_2CuO_4$ as investigated by transport and magnetic measurements. Phys. Rev. B **40** 2254 (1989).

[Tin96] M. Tinkham. *Introduction to Superconductivity.* McGraw-Hill, 2^{nd} edition, (1996).

[Wil99] M. Willemin. *Ultrasensitive Torque Magnetometry on High-T_c Superconductors.* PhD thesis, Universität Zürich, (1999).

[WRB+98] M. Willemin, C. Rossel, J. Brugger, M.H. Despont, H. Rothuizen, P. Vettiger, J. Hofer, and H. Keller. Piezoresistive cantilever designed for torque magnetometry. J. Appl. Phys. **83** 1163 (1998).

[WRH+99] M. Willemin, C. Rossel, J. Hofer, H. Keller, and A. Revcolevschi. Anisotropy scaling close to the ab plane in $La_{1.9}Sr_{0.1}CuO_4$ by torque magnetometry. Phys. Rev. B **59** R717 (1999).

[Zec95] D. Zech. *A Magnetization Study of Cuprate Superconductors.* PhD thesis, Universität Zürich, (1995).

[ZRL+96] D. Zech, C. Rossel, L. Lesne, H. Keller, S.L. Lee, and J. Karpinski. Angle-dependent reversible and irreversible magnetic torque in single-crystalline $Y_2Ba_4Cu_8O_16$. Phys. Rev. B **54** 12535 (1996).

Curriculum Vitae

Personal Data

Name	Stefan Kohout
Date of birth	9. August 1976
Place of origin	Villigen AG, Switzerland
Languages	Czech (native written and spoken) German (proficient written and spoken) English (proficient written and spoken) French (advanced written and spoken) Italian (advanced written and spoken) Spanish (basic written and spoken)

Schools

1983 – 1987	Primary School Villigen AG
1987 – 1988	Primary School Hausen AG
1988 – 1992	Secondary School Windisch AG
1992 – 1996	“Gymnasium” Aarau AG, completed with “Maturität” Typus C

Academic Education

1996 – 2001	Studies at the University of Zurich Major subject: experimental physics Minor subject: information technology
2001	Experimental physics diploma Thesis title: *Messungen am Auslesechip für den PILATUS Detektor*
2001 – 2005	Graduate studies at the University of Zurich

Acknowledgements

Hugo Keller: giving opportunity to work very freely and supporting me throughout the whole project

Sepp Roos: various advice on hardware, measurement and publication issues

The group: comfortable environment and interesting insights into other fields, techniques and cultures

Philippe Niedermann and Arno Hoogerwerf: comfortable collaboration for the fabrication of the sensors

Walter Fässler: always ready with technical tips and organizing exotic tools

Tiziano Crudeli and Martin Klöckner: assistance with technical details

Kurt Bösiger and the machine-shop team: making strange ideas and broken equipment work

Tariel Sakhelashvili and Silvan Streuli: nicely bonding the sensor chips

Toni Schneider: bringing to me the interesting world of critical phenomena

Ralph Pixley: reading “the whole thing” and improving the english

Physics Institute: sympathetic atmosphere and working environment

Maminka a Tatínek: volnost a důvěra

Vera Haas: greatest thanks for everlasting support and help in organizational issues